

Signature Simulation and Characterization of Mixed Solids in the  
Visible and Thermal Regimes

by

Tyler D. Carson

B.S., University of Northern Colorado, 2009

M.S., University of New Mexico, 2011

A dissertation submitted in partial fulfillment of the  
requirements for the degree of Doctor of Philosophy  
in the Chester F. Carlson Center for Imaging Science  
College of Science  
Rochester Institute of Technology

August 2015

Signature of Author \_\_\_\_\_

Accepted by \_\_\_\_\_

Coordinator, Ph.D. Degree Program

CHESTER F. CARLSON CENTER FOR IMAGING SCIENCE  
COLLEGE OF SCIENCE  
ROCHESTER INSTITUTE OF TECHNOLOGY  
ROCHESTER, NEW YORK

CERTIFICATE OF APPROVAL

---

Ph.D. DEGREE PROPOSAL

---

The Ph.D. Degree Dissertation of Tyler D. Carson  
has been examined and approved by the  
dissertation committee as satisfactory for the  
dissertation required for the  
Ph.D. degree in Imaging Science

---

Dr. Carl Salvaggio, Dissertation Advisor	Date
--	------

---

Dr. Charles Bachmann

---

Dr. Michael Gartley

---

Dr. Jiandi Wan

Signature Simulation and Characterization of Mixed Solids in the Visible and Thermal  
Regimes

*by*

Tyler D. Carson

Submitted to the  
Chester F. Carlson Center for Imaging Science  
in partial fulfillment to the requirements  
for the degree of Doctor of Philosophy  
at the Rochester Institute of Technology

**Abstract**

Solid target signatures vary due to geometry, chemical composition and scene radiometry. Although radiative transfer models and function-fit physical models may describe certain targets in limited depth, the ability to incorporate all three of these signature variables is difficult. This work describes a method to simulate the transient signatures of mixed solids and soils by first considering scene geometry that was synthetically created using 3-d physics engines. Through the assignment of spectral data from the Nonconventional Exploitation Factors Data System (NEFDS) and other libraries, synthetic scenes are represented as a chemical mixture of particles. Finally, first principles radiometry is modeled using the Digital Imaging and Remote Sensing Image Generation (DIRSIG) model. With DIRSIG, radiometric and sensing conditions were systematically manipulated to produce goniometric signatures. The implementation of this virtual goniometer allows users to examine how a target bidirectional reflectance function (BRDF) and directional emissivity will change with geometry, composition and illumination direction. The tool described provides geometry flexibility that is unmatched by radiative transfer models. It delivers a discrete method to avoid the significant cost of time and treasure associated with hardware based goniometric data collections.

## *Acknowledgements*

We would like to thank the National Reconnaissance Office for funding this work.



## *Disclaimer*

The views expressed herein are those of the author and do not reflect the official policy of the U.S. Air Force, Department of Defense, or the U.S. Government

# Contents

<b>Abstract</b>	<b>ii</b>
<b>Acknowledgements</b>	<b>iii</b>
<b>Disclaimer</b>	<b>iv</b>
<b>Contents</b>	<b>v</b>
<b>List of Figures</b>	<b>viii</b>
<b>List of Tables</b>	<b>x</b>
<b>1 Introduction</b>	<b>1</b>
<b>2 Theory</b>	<b>8</b>
2.1 Electromagnetic Radiation . . . . .	8
2.2 Material Properties . . . . .	10
2.3 Geometry and Modes of Scatter . . . . .	12
2.3.1 Specular Reflections . . . . .	14
2.3.2 Diffuse Reflections . . . . .	15
2.3.3 Directional Diffuse Reflections . . . . .	15
2.4 Directional Scatter and BRDF . . . . .	16
2.5 Directional Emissivity . . . . .	18
2.6 Reflection Components of the Beard-Maxwell Model . . . . .	18
2.7 Ground and Pupil Plane Radiance . . . . .	19
2.7.1 Approximations to the Governing Equation . . . . .	22
2.7.2 Pupil Plane Radiance in the VNIR/SWIR . . . . .	23
2.7.3 Pupil Plane Radiance in the LWIR . . . . .	23
2.7.4 Pupil Plane Radiance in the MWIR . . . . .	23
2.7.5 Pupil Plane Radiance For a Virtual Goniometer . . . . .	23
<b>3 Background</b>	<b>25</b>
3.1 Modeling Tools . . . . .	25
3.1.1 Blender Physics Engine . . . . .	25
3.1.2 DIRSIG . . . . .	26

3.1.3	NEFDS . . . . .	27
3.1.4	Electron Microscopy . . . . .	27
3.1.4.1	Electron Microscopy Principles . . . . .	28
3.1.4.2	X-Ray Microanalysis . . . . .	29
3.2	Mixed Solid Targets . . . . .	30
3.2.1	Soil Particles . . . . .	30
3.2.2	Soil Particles With Chemical Contaminants . . . . .	31
3.2.3	Man Made Surfaces With Soil Contaminants . . . . .	32
3.2.4	Spectral Features of Soil Targets . . . . .	32
<b>4</b>	<b>Methodology</b>	<b>37</b>
4.1	Scene Construction . . . . .	38
4.1.1	Microscopy . . . . .	38
4.1.2	Blender 3-D Modeling . . . . .	40
4.1.3	ODB Files . . . . .	41
4.2	Virtual Hardware . . . . .	41
4.2.1	DIRSIG Simulation File . . . . .	41
4.2.2	Shell File Creation . . . . .	42
4.2.3	Python Editor . . . . .	43
4.2.4	ENVI File Analysis . . . . .	43
4.2.5	Display . . . . .	45
4.3	Goniometric Modeling of Soil in the Visible Regime . . . . .	46
4.3.1	Scene Recreation . . . . .	47
4.3.2	Goniometer Re-creation . . . . .	47
4.3.3	Experimental Procedures . . . . .	48
4.3.4	Goniometer Modifications . . . . .	48
4.3.5	Complex Soil Scenes . . . . .	49
4.4	Goniometric Modeling Using the NEFDS . . . . .	51
4.4.1	Soil Contaminant Study Using NEFDS Data . . . . .	52
4.5	Soil Features in the Longwave Infrared . . . . .	54
4.5.1	Geometry . . . . .	54
4.5.2	Hyperspectral Sensor . . . . .	56
4.5.3	Chemistry . . . . .	56
4.5.4	Radiometry . . . . .	57
4.6	Modeling the Signatures of Particle Size Distributions . . . . .	59
4.6.1	Geometry . . . . .	59
4.6.2	Chemistry . . . . .	61
4.6.3	Radiometry . . . . .	62
4.7	Directional Reflectance and Emissivity of Lab Targets . . . . .	62
4.7.1	Directional Emissivity Measurements . . . . .	63
4.7.2	BRDF of Soil with Calcium Chloride Solution . . . . .	64
4.7.2.1	BRDF of Collection with GRIT . . . . .	65
4.7.2.2	BRDF Simulation . . . . .	67
<b>5</b>	<b>Results</b>	<b>68</b>
5.1	Goniometer Recreation and Soil Study . . . . .	68

---

5.2	Complex Soil Scenes . . . . .	72
5.2.1	Tire Track Scene . . . . .	72
5.2.2	Modeling the Effects of Porosity and Particle Size . . . . .	76
5.3	BRDF Simulation Using the NEFDS . . . . .	82
5.4	Soil Signatures in the LWIR . . . . .	89
5.5	Directional signatures of liquid contaminants . . . . .	93
<b>6</b>	<b>Summary and Conclusions</b>	<b>102</b>
6.1	Recommendations . . . . .	104
6.1.1	Emissivity file format . . . . .	104
6.1.2	Fluid Simulation . . . . .	106
6.1.3	Advanced Ray Tracing for Sensitive Absorption Features . . . . .	107
	 Bibliography	 <b>112</b>

# List of Figures

2.1	Reflection . . . . .	13
2.2	Specular and Diffuse . . . . .	14
2.3	Microfacet Scattering . . . . .	17
3.1	Convex Hull . . . . .	26
3.2	Sand and Calcium Chloride (SEM Image) . . . . .	28
3.3	X-ray Microanalysis . . . . .	29
3.4	Soil Emissivity . . . . .	33
3.5	Disturbed, Tamped and Undisturbed Soil in the LWIR . . . . .	35
3.6	Undisturbed and Wet Sieved Soil in the LWIR . . . . .	36
3.7	Directional emissivity of quartz . . . . .	36
4.1	Sand Particles (SEM Image) . . . . .	39
4.2	Blender Model of Soil Grains . . . . .	39
4.3	Blender Physics Engine . . . . .	40
4.4	Goniometer Workflow . . . . .	42
4.5	Sensor Response . . . . .	44
4.6	Blender Interface . . . . .	46
4.7	Tire Track Scene . . . . .	50
4.8	Complex Soil Scene . . . . .	50
4.9	DHR Based Reflection . . . . .	52
4.10	Sand On Paint . . . . .	53
4.11	DHR Based Reflection . . . . .	54
4.12	Dusty Grains . . . . .	55
4.13	Scene Building In Blender . . . . .	56
4.14	Particle Size Distributions . . . . .	60
4.15	Density Comparison . . . . .	60
4.16	Magnetite Scene Distribution . . . . .	61
4.17	Soil Radiance . . . . .	64
4.18	Contaminated Sand . . . . .	65
4.19	GRIT . . . . .	66
4.20	Particle Simulation Scene . . . . .	67
5.1	Principal And Perpendicular Planes . . . . .	69
5.2	Principle Plane Soil BRDF . . . . .	70
5.3	Perpendicular Plane Soil BRDF . . . . .	71
5.4	Sensor Pixel Study . . . . .	72

5.5	Principle Plane Soil BRDF with 80% Hemispherical Illumination . . . . .	73
5.6	Perpendicular Plane Soil BRDF with 80% Hemispherical Illumination . .	73
5.7	Tire Track With Varying Illumination Source Position . . . . .	74
5.8	Tire Track BRDF (30° Source Zenith) . . . . .	75
5.9	Tire Track BRDF (55° Source Zenith) . . . . .	75
5.10	Tire Track BRDF (75° Source Zenith) . . . . .	76
5.11	BRDF Of A Uniform Distribution . . . . .	78
5.12	BRDF Of Unimodal And Bimodal Distributions . . . . .	79
5.13	DIRSIG Error Analysis . . . . .	80
5.14	BRDF Of Quartz-Magnetite Mixture . . . . .	81
5.15	BRDF Change With Phase Angle . . . . .	82
5.16	Car Paint Contamination (98% surface coverage) . . . . .	84
5.17	Car Paint Contamination (90% surface coverage) . . . . .	84
5.18	Car Paint Contamination (44% surface coverage) . . . . .	85
5.19	Car Paint Contamination (27% surface coverage) . . . . .	85
5.20	Car Paint Contamination (Illumination at Nadir) . . . . .	86
5.21	Car Paint Contamination (Illumination Comparison) . . . . .	87
5.22	Reflectance With Surface Coverage at nadir . . . . .	88
5.23	Reflectance With Surface Coverage (30) . . . . .	89
5.24	Reflectance With Surface Coverage (50) . . . . .	90
5.25	3 Particle Scene . . . . .	91
5.26	Disturbed Soil . . . . .	91
5.27	Impact Of Grain Boundaries . . . . .	93
5.28	Calibrated Sand . . . . .	94
5.29	Calcium Chloride Powder . . . . .	95
5.30	Baked Calcium Chloride Solution . . . . .	95
5.31	Sand With Calcium Chloride . . . . .	96
5.32	Calibrated Sand LWIR . . . . .	96
5.33	Sand With Calcium Chloride . . . . .	97
5.34	Baked Calcium Chloride Sample . . . . .	98
5.35	DIRSIG Contamination Scene (NADIR) . . . . .	98
5.36	DIRSIG Contamination Scene (40 Degrees) . . . . .	99
5.37	Water LWIR . . . . .	100
5.38	Micro Dirsig . . . . .	101
6.1	Work Breakdown Structure . . . . .	103
6.2	Quartz . . . . .	106
6.3	Fluid Simulation . . . . .	107
6.4	Quartz Reflectance (100-200 $\mu m$ ) . . . . .	108
6.5	Quartz Reflectance (<75 $\mu m$ ) . . . . .	110
6.6	Attenuation in Quartz (0 Degrees) . . . . .	110
6.7	Attenuation in Quartz (60 Degrees) . . . . .	111

# List of Tables

2.1	Typical bands of operation in remote sensing . . . . .	9
4.1	Spectrometer specifications for directional emissivity measurements . . . .	63
4.2	Specifications for the high resolution spectroradiometer that is used in conjunction with GRIT. . . . .	66

# Chapter 1

## Introduction

How can we pinpoint the directional scattering of spectral radiation from surfaces comprised of mixed materials? Surface properties of reflectance and emissivity are parameters required to define a scattering signature. Many specimens in our world are made of material mixtures. Consequently, optical properties that describe surface radiometry can vary within a single target.

Consider an asphalt road littered with a sand contaminant. This sand lays upon the road with a particular geometric pattern. Imagine that this pattern is the recognizable form of a tire track. If this target were to be remotely sensed, there would be areas where a percentage of the signal could be attributed to pure asphalt, pure sand, and a combination of the two materials. If the sensor field-of-view changes, or the sun becomes occluded by clouds, an identical radiance measurement of the target can not be reproduced. This is because illumination and the geometry of the target have changed with respect to the sensor.

At first thought, making goniometric target measurements might seem like the best and only method to redefine the reflective features of the tire track (Wang et al., 2010). Logistically, it is a difficult solution. A robust target signature would require measurements at every view angle and lighting scenario. To ensure consistent measurements that can be compared with observations of other targets and scenes, the same sensor or sensor characteristics should be used for each goniometric measurement. The optical and radiometric characteristics of the imaging system should be repeatable. In situ target geometry for many surfaces is difficult or impossible to replicate in lab environments (Johnson et al., 1998a). Traveling to targets of interest is often costly and is always weather dependent. Therefore, a physics-based signature recreation tool would



be of great value. Simulation experiments could be completed rapidly, and scene content would adhere to both rigid body dynamics and soft body dynamics.

The basis of such a modeling tool lies in the realm of computer graphics. Accurate measurements require precise virtual geometry, goniometric measurement, and evaluation tools that plausibly describe nature. These deliverables have origin in the form of procedural shaders used by artists. A shader is simply an algorithm that produces the physically possible or visually pleasing levels of light and color in an image.

In the past, physically based shading was a consideration second in importance to artists. The primary concern of the graphic design community has been to give artists as much freedom to create, as their software will allow. Walt Disney (Burley, 2012) and their Pixar studios subsidiary (Hery and Villemin, 2013) are pushing the bounds of realistic animation. They have found that if motion picture animations are to be faithful to reality, physical plausibility must be observed.

To animate reproductions of fine texture, such as hair and cloth, physical shading and lighting must be used (Westin et al., 1992, 2004, Xu et al., Darling and Ferwerda, 2009). Disney implemented these techniques with difficulty at first. Previously, artists could rely on experience to place lights and shade objects in ways that produced visually pleasing scenes. These learned techniques were found to clash with boundary conditions that accompany physical shading. Scene creation and editing became more time intensive, but for the sake of realism.

Animators have come to the conclusion that to truly mimic reality, lighting and shading should be consistent for all scenes and materials. Thus, the film industry has invested much in the research and development of reflectance modeling. Preexisting material reflectance databases (Torrance and Sparrow, 1976) have been exploited in order to test new algorithms (Westin et al., 2004). Designers wish to find or create models that are physically based, while still providing adjustable parameters for artistic control. Many published models have been refined over time to include comprehensive physical traits such as index of refraction or faceted surfaces (He et al., 1991, Ngan et al., 2005). A problem for both animators and scientists alike, is the narrow scope of most models. Accuracy is sacrificed in exchange for concise comprehensive equations that can be used for many different surfaces. Certain pure materials have been characterized quite well by shader models (Nayar and Oren, 1995, Hanrahan and Krueger, 1993, Beckmann and Spizzichino, 1963, Ashikmin and Shirley, 2000). This is done primarily through data fitting. However, a single descriptor for all materials has yet to be derived (Torrance and Sparrow, 1976). This is not surprising. Human perception and science tell us that objects of different materials look dissimilar under different lighting and viewing

conditions (Ientilluci and Gartley, 2009). Variance in reflection is precisely why graphic artists and scientists need a test-bed to define materials and models that describe them. Developing such a tool will exhibit shortcomings, advantages and limits of simulation.

Material definition hinges upon the understanding of the radiation signal that propagates between a material and a sensor. Radiance that reaches the pupil plane of a sensor is dependent upon the reflectance distribution and can be written:

$$L(\lambda, \theta_v, \phi_v, \theta_l, \phi_l) = \left[ \frac{E_l(\lambda)}{\pi} \cos(\theta_l) \tau_1(\lambda, \theta_l) f(\lambda, \theta_v, \phi_v, \theta_l, \phi_l) + \epsilon(\lambda, \theta_v, \phi_v) L_T(\lambda, T) \right] \tau_2(\lambda, \theta_v) + L_u(\lambda, \theta_v) \quad (1.1)$$

The angular orientation of the solar source is represented with  $(\theta_l, \phi_l)$ , while the sensor viewing position is described using  $(\theta_v, \phi_v)$ . These directly relate to the bidirectional reflectance distribution function  $f(\lambda, \theta_v, \phi_v, \theta_l, \phi_l)$ . As this equation is wavelength dependent, self-emitted blackbody radiance  $L_T(\lambda, T)$  and directional emissivity  $\epsilon(\lambda, \theta_v, \phi_v)$  are also considered.

Reflectance ( $f$ ) is incorporated in computer graphics through the rendering equation (Kajiya, 1986). A general BRDF can be contrived for most surfaces if diffuse and specular reflections are considered separately (He et al., 1991). By separating these two features, models tend to yield discontinuities at different light source and view angles. This is because specular lobes are observed to have finite support or “wings”. These wings are attributed to absorption, re-emission and geometry that are not well captured by general models.

To predict the reflection of most natural materials, surfaces are approximated by an assortment of Lambertian facets. Physics-based BRDF models that stem from a micro-facet basis have a general form:

$$f(l, v) = \text{diffuse} + \frac{D(\theta_h) F(\theta_d) G(\theta_l, \theta_v)}{4 \cos \theta_l \cos \theta_v} \quad (1.2)$$

As before,  $f$  represents the bi-directional reflectance function (BRDF).  $D$  is the microfacet distribution function. This term gives the specular lobe its shape.  $G$  is the geometric attenuation factor. This factor accounts for the shadowing of facets by other surface facets. This parameter becomes important at near grazing view and light source angles.  $F$  is the Fresnel reflection coefficient which represents the manner that specular reflections change when light and view vectors move apart.  $\theta_l$  is the incident angle of

light and  $\theta_v$  is the view angle. Both of these angles are measured with respect to a half-vector, which lies directly between the incident light vector and the view vector. There are many instances when a viewing vector is not coincident with the Fresnel reflection vector. It is due to these instances that two more angles should be defined.  $\theta_h$  is the angle between the surface normal and the half-vector.  $\theta_d$  is the difference angle between incident light and the half-vector.

Several graphics tools have been developed to examine BRDF models (Burley, 2012, Hery and Villemin, 2013, Colbert et al., 2006). These softwares allow specular and diffuse models to be mixed and matched to create visually pleasing art. This capability also allows artists to use models in conjunction with scenarios for which they are best suited. For instance, an Oren-Nayar diffuse model may better describe a rough material lit at grazing angles when compared to a Lambertian model. Using a tool like BRDF explorer, designers can modify functional parameters native to chosen models and compare results, BRDFs, with measured data. Such BRDF plots can serve as target signatures.

It is desirable to use reflectance to identify objects and view their radiometric features. Graphic design tools provide a remarkable interface for users to visually see how geometry and optical parameters affect radiometry. But, they fail to meet key scientific performance parameters for a few reasons:

First, surface geometry and material makeup dictate both the diffuse and specular components of every physically based BRDF model (Nicodemus et al., 1977). Many objects are anisotropic and possess an asymmetric form. Generic shader models cannot account for this fact. Inconsistencies in diffuse reflection models emerge as incident light or the viewing vector approach grazing angles with an object's surface. Although models do predict physical retro-reflections (Burley, 2012, Hanrahan and Krueger, 1993), they are not as pronounced as measured data indicates. In short, they do not produce results that accurately model the real world.

Rough material samples have also been shown to vary from the expected reflectance results predicted by the Fresnel effect (Ngan et al., 2005). That is, reflected light is often observed in directions that are not coincident with a perfect reflection. BRDF models must account for "off specular" reflectance peaks by adding parameters. These parameters account for the fact that particles, making up even relatively flat surfaces, shadow one another. Shadowing depends on micro-facet distributions and specularity. Thus, shadowing effects vary from surface to surface and BRDF predictions of any one single model are often inaccurate.

Reflectance functions are derived based on curve fits to data. Most of the goniometric data used for these fits corresponds to the visible spectrum. Authors claim that wavelength dependence of shader models is embedded in albedo parameters (He et al., 1991, Nayar and Oren, 1995, Gondek et al., 1994). Albedo is the fraction of incident electromagnetic radiation reflected by a surface. The directional dependence of albedo is often left unaccounted for. At near grazing incidence and observation angles, albedo has a high correspondence to surface roughness. It is not well behaved. Curve fitting is taxing on the albedo function. In order to match measured reflectance data points, unrealistic albedo values are often required (Nayar and Oren, 1995, Ward, 1992, Dür, 2006). In some instances, energy conservation is ignored (Geisler-Moroder and Dür, 2010). This diminishes any precise information pertaining to a material-wavelength relationship.

Also, modeling the infrared spectrum would require emissivity information that shader models lack (Kerekes et al., 2008).

Most surface reflection models are principled in that they possess parameters that are tied to physical material properties. However, they are general and do not account for spatially varying features (Dong et al., 2010). They are not necessarily physically correct. This is why mixed solids such as soil and sand are optimal for comparative research. Even a smooth layer of sand or dirt has large rough features compared to the wavelength of visible and infrared radiation. This is why soils can be described using primarily diffuse BRDF parameters (Nayar and Oren, 1995). Specular materials require parameters to describe their “glossiness” and parameters to describe their macro features (He et al., 1991). The addition of these factors results in added approximation and generalization.

Rougher surfaces made of shiny materials are also hard to model because diffuse parameters always dominate the fitting curves (Westin et al., 1992, Xu et al., Nayar and Oren, 1995, Beckmann and Spizzichino, 1963). Material properties related to specular reflection are overlooked. Very flat specular materials, and very rough materials such as soil are typically easy to interpolate. Materials that are man made are rarely so well defined. Often, they require double distribution curve fits that model targets as layers rather than particles (Hanrahan and Krueger, 1993). Using multiple distributions results in more empirical parameter values. This can lead to inaccurate reflectance values that are not physical in nature. In general, interpolation can not be used to describe a surface comprised of multiple materials. Graphic designers use blending software to make reflection gradients visually palatable (Hery and Villemin, 2013). Scientists do not have that luxury.

Banninger (Bänninger and Flühler, 2004) and others (Li et al., 1996, Liang and Townshend, 1996) built upon earlier work of soil specific radiative transfer (Hapke, 1993) to link the spatial characteristics of mixed soils to BRDF. By treating particles as layered thin films, subsurface soil scattering was determined by the thickness and refractive index of each thin slab. This work connected light scatter to surface texture. Based on the evaluation of graphics shaders, one would expect texture and backscatter effects to be noticeable at large zenith angles. Banninger showed that the influence of texture on reflectance is measureable at zenith angles as small as 45 degrees. Using polarization effects (Liang and Townshend, 1996), investigations also confirmed an increase in reflectance and decrease in transmittance with decreasing particle size. The model by Li (Li et al., 1996) correctly predicted the tinted appearance of rough surfaces that is brought on by shadowing and multiple top-surface reflections.

As is true with shader models, the accuracy of any reflectance function depends on the number of free parameters, and on how well model approximations align with the physical surface to be modeled. Although the soil specific methods (Bänninger and Flühler, 2004, Li et al., 1996, Liang and Townshend, 1996, Hapke, 1993) are based in physics rather than generalized analytic shading, they do not guarantee physical consistency. Albedo and index of refraction are still treated as empirical parameters. A supposition consistent within all of the discussed models is that light is comprised of optical wavelengths only. This makes the empirical albedo term even more ambiguous. Anisotropic features are treated with specific approximations in (Hapke, 2012a). Notably, the angular scattering functions of individual particles are represented as a constant averaged function, and multiple scattering is incorporated using the Chandrasekhar functions of isotropic scatterers. If a surface is deemed to be sufficiently anisotropic (Li et al., 1996), Mie theory is used to describe the single scattering albedo. Mie theory is not a good approximation for packed soils, as a spherical scattering approximation cannot be anticipated. Such a model would not adequately describe effects of weathering or human interaction.

Wang (Wang et al., 2010) attempted to gain insight into soil reflectance through the use of advanced imaging spectrometers oriented in multiple view directions. Such tools were also used by (Kerekes et al., 2008) to make reflectance and emissivity measurements of contaminated surfaces. Classification algorithms were used to analyze data. It was shown that the BRDF of smooth surfaces is dominated by illuminated pixels and BRDF of rougher surfaces is dominated by dark shaded pixels. Moreover, rougher surfaces exhibit greater variation in BRDF than do smooth surfaces. Variation in BRDFs generated from NIR light sources is more distinct than those generated from visible illumination. This supports the use of BRDF for target identification.

Gartley (Gartley et al., 2008a,b) and the Rochester Institute of Technology have developed tools to aid in the exploration of non-constant BRDFs. Digital Imaging and Remote Sensing Image Generation (DIRSIG) provides a work-around for the problems and inaccuracies inherent to data collects. DIRSIG considers the self-emission contributions that are relevant for infrared targets. It also does not require surfaces to be described by some mathematical form. Surfaces can be created using graphic art tools. Then, the solid angle of a detector can be tracked as rays of light bounce between materials that make up a surface. A single run can capture a full hemispherical BRDF for any zenith and azimuth combination. Using this software, materials mixed with contaminants can be studied. Potentially, fine-grain (10-20 micron) soil particles can be included individually in radiometric simulation. Johnson (Johnson et al., 1998a) found that the deposition of such particles have the tendency to reduce spectral contrast in the infrared.

This thesis presents a new goniometric tool that serves as a test-bed for the signatures of mixed solids in the optical and infrared wavelength regimes. The research has three main components: a virtual goniometer structure, a method to realistically create mixed solids on the particle scale, and a simulation tool to apply realistic lighting, and output 3-D BRDF signatures based on standardized data sets.

## Chapter 2

# Theory

Recorded light reflecting or emitting from a scene provides information about environmental geometry and material make-up. Such light undergoes modification as it travels. Light that is *modified* by a target of interest will also be subjected to un-interesting, yet impactful, interactions with the atmosphere and the device used for recording. It follows that in order to measure or model distinct targets, many natural processes must be understood. These principles are listed below:

### THE RADIATION OF LIGHT

### SCENE GEOMETRY AND MATERIAL PROPERTIES

### THE DYNAMICS OF LIGHT PROPAGATION

### LIGHT DETECTION

### MODELING TECHNIQUES

Once equipped with an appreciation of how light tends to interact with a scene, characteristic trends can be defined and used for differentiation and identification.

## 2.1 Electromagnetic Radiation

The energy that is captured by sensors and used to produce imagery is a form of electromagnetic (EM) radiation. Light energy is measured in joules (J). It travels as a wave

with orthogonal electric field, magnetic field and propagation components. The distance between two consecutive elements of a wave is known as wavelength ( $\lambda$ ), and it is by this unit that radiation is characterized. The speed of light propagation can be calculated using the equation below.

$$c = \lambda\nu \quad (2.1)$$

Speed ( $c$ ) is measured in units of meters per second and frequency ( $\nu$ ) is measured in hertz (Hz) or cycles per second. In a vacuum the speed of light is  $2.997 \times 10^8$  m/s.

Photons are quantifiers that describe the particle nature of light. The ability of light to possess energy and momentum is a byproduct of the wave-particle duality of radiation. Energy is wavelength dependent and is given by

$$E = \frac{hc}{\lambda} \quad (2.2)$$

Planck's constant  $h = 6.626 \times 10^{-34}$  J s (joule second).

Light spans a large wavelength range and it is convenient to partition spectra into bands. The majority of remote sensing occurs in the ultraviolet (UV), visible and infrared (IR) regimes. A list of bands is shown in Table 2.1. By evaluating the equation above, it is noted that shorter wavelengths correspond to higher energies than do longer wavelengths.

Name	Abbreviation	Wavelength [micron]
Ultraviolet	UV	0.01 - 0.4
Visible	VIS	0.4 - 0.7
Near Infrared	NIR	0.7 - 1.0
Shortwave Infrared	SWIR	1.0 - 2.5
Midwave Infrared	MWIR	3.0 - 5.0
Longwave Infrared	LWIR	8.0 - 14.0

TABLE 2.1: Typical bands of operation in remote sensing

The visible band comprises light corresponding to the sensitivity of the human eye. By remote sensing standards, this band is dominated by the reflection of light from materials rather than the emission of radiation from a material itself. This feature of nature makes detection in the visible regime relatively easy. The same characteristic makes detection in the infrared bands more complex. Near IR (NIR) and Shortwave IR (SWIR) are subject



to solar reflections; self emission is relatively negligible. The threshold of reflection and emission processes is approached in the Midwave IR (MWIR) spectrum. During daylight hours, detection in the MWIR includes both reflected and emitted photons. Night-time sensing in the MWIR considers self emission only. Incidentally, MWIR measurements are difficult to make and require a priori knowledge that is unnecessary for data collection in other bands. Because the Longwave IR (LWIR) is often used to determine temperature in a scene, it is also referred to as the *thermal infrared* (TIR) band. Common imaging tasks in the TIR include target detection and night vision. The goal of this research is to obtain signatures of mixed solids in the visible and infrared regions.

## 2.2 Material Properties

Reflectance is the ratio of irradiance ( $W/m^2$ ) that is reflected from a surface ( $M_\rho$ ) to the irradiance that is incident upon that same surface ( $E_i$ ). The amount of light that is reflected from a surface is wavelength dependent. This is why surfaces possess different signatures when they are sensed over varying spectral bands.

$$\rho(\lambda) = \frac{M_\rho(\lambda) [Wm^{-2}]}{E_i(\lambda) [Wm^{-2}]} \quad (2.3)$$

Not all light that strikes a surface is reflected. Some irradiance ( $W/m^2$ ) is transmitted through the surface ( $M_\tau$ ), and some is absorbed ( $M_\alpha$ ). Transmittance is the ratio of irradiance ( $W/m^2$ ) that is transmitted through a surface to the irradiance that is incident upon the surface ( $E_i$ ).

$$\tau(\lambda) = \frac{M_\tau(\lambda) [Wm^{-2}]}{E_i(\lambda) [Wm^{-2}]} \quad (2.4)$$

Absorbance or absorbtivity is written in similar fashion.

$$\alpha(\lambda) = \frac{M_\alpha(\lambda) [Wm^{-2}]}{E_i(\lambda) [Wm^{-2}]} \quad (2.5)$$

Energy can only be subjected to the three functions of reflection, transmission and absorption. Therefore, energy is conserved within these three parameters and the total irradiance that is reflected, transmitted and absorbed is equal to the initial incident irradiance.

$$\frac{M_\rho(\lambda)}{E_i(\lambda)} + \frac{M_\tau(\lambda)}{E_i(\lambda)} + \frac{M_\alpha(\lambda)}{E_i(\lambda)} = \rho(\lambda) + \tau(\lambda) + \alpha(\lambda) = 1 \quad (2.6)$$

Temperature also induces materials to emit energy. This energy is in addition to the radiation that impinges upon a surface from external sources. Emissivity is the metric formally used to denote the ability of surfaces to emit energy. It is the ratio of the emitted irradiance ( $W/m^2$ ) from a surface ( $M_\varepsilon$ ) to irradiance emitted from a perfect absorber and emitter. Perfect radiators are also known as blackbodies. Emissivity is a function of temperature, and because the blackbody term below is a perfect radiator,  $\varepsilon$  has values between zero and one.

$$\varepsilon(T) = \frac{M_\varepsilon(T)}{M^{BB}(T)} \frac{[Wm^{-2}]}{[Wm^{-2}]} \quad (2.7)$$

Kirchoff's law states that for objects in thermal equilibrium, absorbance is approximately equal to emissivity.

$$\alpha \approx \varepsilon \quad (2.8)$$

The conservation of energy equation can then be altered accordingly.

$$\rho(\lambda) + \tau(\lambda) + \varepsilon(\lambda, T) = 1 \quad (2.9)$$

Note that this generalized approximation indicates that energy conservation is a function of two variables (wavelength and temperature). These independent processes are linked and made dependent through this new relationship. Making this assertion complicates all attempts to accurately model irradiance leaving a surface. Models that attempt to define target exitance by curve fitting may neglect the complexities induced by this approximation. Although parameter fitting may provide a repeatable description of a geometry, it may also violate the principles of energy conservation and be deemed *unphysical*.

Planck found the the exitance ( $W/m^2$ ) of a black body to be dependent on both temperature and wavelength.

$$M(\lambda, T) = \frac{2\pi hc^2}{\lambda^5} \frac{1}{e^{\frac{hc}{\lambda kT}} - 1} \frac{[W]}{[m^2 \cdot m]} \quad (2.10)$$

Where  $k$  is the Boltzman constant ( $1.3807 \times 10^{-23}$  J/K),  $h$  ( $6.626 \times 10^{-34}$  J s) is Planck's constant and  $T$  is temperature in Kelvin (K). The Stefan-Boltzman law describes the total exitance produced by a blackbody. It is found by integrating the above equation over all wavelengths, making exitance a function of temperature only.

$$M_{BB}(T) = \sigma T^4 \frac{[W]}{[m^2]} \quad (2.11)$$

Where  $\sigma$  is the Stefan-Boltzman constant ( $5.6704 \times 10^{-8}$  W/m<sup>2</sup>/K<sup>4</sup>). The spectral exitance peak of a blackbody curve can be found by using the Wien displacement law.

$$\lambda_{max} = \frac{2898}{T} [\mu m] \quad (2.12)$$

## 2.3 Geometry and Modes of Scatter

It was stated that light that impinges upon a surface may exclusively take part in processes of scatter (reflection), absorption, or transmission. Most targets of interest in remote sensing are not transmissive, and Kirchoff's law is exploited to yield a conservation equation containing measurables that can be more easily sensed from a large distance.

$$\rho + \varepsilon = 1 \quad (2.13)$$

The reflection parameter in this equation is based upon optical scatter which is dependent upon the geometry of a scene or target. It is most convenient to understand reflection using a coordinate system.

There are three important known geometric parameters that are used to model or collect reflectance data. These include the position of the illuminating light source, the surface normal of the target and the position of the detection device or camera. Light arriving at the surface of a scene is measured angularly with respect to the surface normal ( $\theta_i$ ), and with respect to a direction in the x-y plane designated as north ( $\phi_i$ ). The subscript  $i$  denotes that these are incident light angles from a source. As radiation is scattered from the target towards a detector, it leaves in a direction specified by ( $\theta_r$ ) and ( $\phi_r$ ). These are known as reflection angles. Angles in the  $\theta$  plane are referred to as *zenith* or *declination* angles. An angle in the  $\phi$  plane is called an *azimuth* angle.

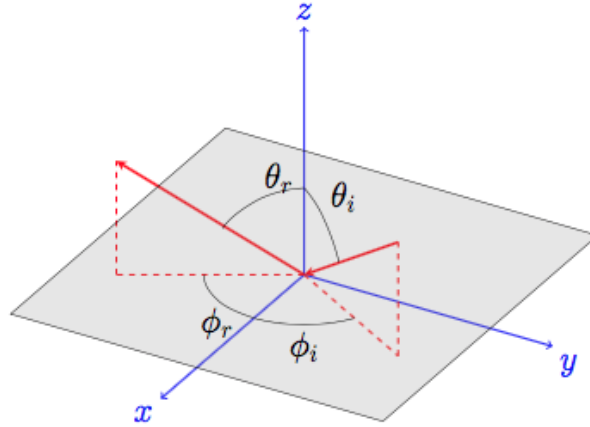


FIGURE 2.1: Reflection with respect to surface normal

In reality, light reaches the target in Figure(2.1) over some solid angle ( $\Omega$ ). This angle corresponds to light that subtends an area ( $A$ ) on the surface of a sphere. This sphere has a radius written below as  $r$ . The unit of solid angle is the steradian (sr).

$$\Omega = \frac{A}{r^2} [sr] \quad (2.14)$$

This research addresses reflectance and emission in the visible and IR bands. In the visible bands (where wavelength is relatively short), *geometric scattering* is assumed. This insinuates that light travels in straight lines as rays and bounces off surfaces as small particles. In consequence, light is not treated as a wave and interference is ignored. Longer IR wavelengths are more susceptible to interference as they approach the size of macroscopic surface features that comprise different targets. Diffraction will occur and the intensity of light that reaches an observer will vary accordingly.

Radiation scatter fluctuates based on target geometry and wavelength. Smooth surfaces reflect light in strongly directional fashion. Examples of smooth surfaces are mirrored glass, chrome or car sealant. Directional reflections are termed *specular*. Specularity is the component most commonly associated with reflection. Additional scattering components include *diffuse* and *directionally diffuse* reflections. All three components will be discussed further. A diagram of each can be seen in Figure(2.2).

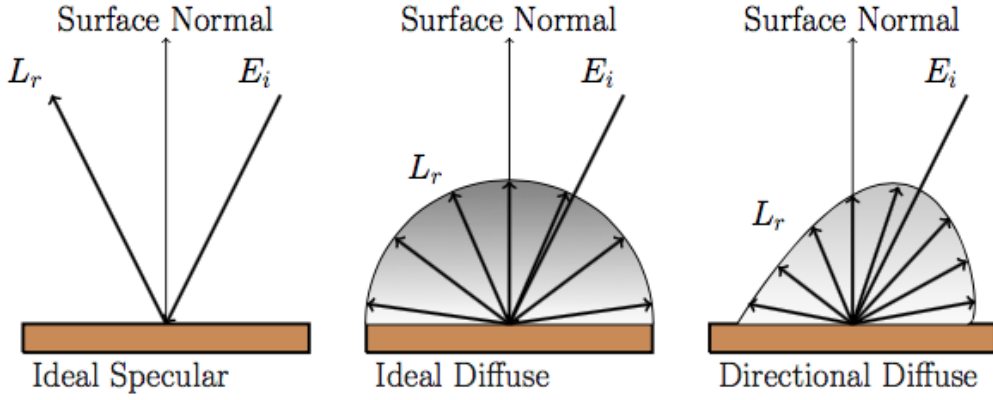


FIGURE 2.2: Three different scattering modes.

### 2.3.1 Specular Reflections

Materials that are comprised of smooth surfaces or flat facets reflect light without volume scattering. This means that the solid angle of incoming radiation is preserved as light leaves the surface. It also requires that light behave in accordance with the law of reflection; that all the light not absorbed or transmitted through a surface will leave the plane at an angle equal to the incident angle.

$$\theta_i = \theta_r \quad (2.15)$$

Using Fresnel's equations, incident light that is normal to a dielectric (non-conductive) target surface reflects light as a function of the index of refraction of the dielectric ( $\eta_2$ ) and the index of the air above the target ( $\eta_1$ ).

$$\rho = \left( \frac{\eta_2 - \eta_1}{\eta_2 + \eta_1} \right)^2 \quad (2.16)$$

Light falling on a facet at an angle will trigger a polarized reflection beam. This beam is described by its perpendicular (horizontal) and parallel (vertical) linearly polarized reflectance.

$$r_{\perp}(\theta_i) = \left[ \frac{(n^2 - \sin^2 \theta_i)^{1/2} - \cos \theta_i}{(n^2 - \sin^2 \theta_i)^{1/2} + \cos \theta_i} \right]^2 \quad (2.17)$$

$$r_{\parallel}(\theta_i) = \left[ \frac{n^2 \cos \theta_i - (n^2 - \sin^2 \theta_i)^{1/2}}{n^2 \cos \theta_i + (n^2 - \sin^2 \theta_i)^{1/2}} \right]^2 \quad (2.18)$$

Where  $n$ , the relative index of refraction, is the ratio of the surface index to the index of air ( $n = \eta_2/\eta_1$ ). If the light that falls on the surface is randomly polarized to begin with, the reflection is the average of the two components.

$$\rho = \frac{r_{\parallel} + r_{\perp}}{2} \quad (2.19)$$

Finally we can solve for the target leaving radiance ( $L_r$ ) for the ideal specular reflectance shown in Figure(2.2).

$$L_r = \frac{L_i}{2} r_{\perp} + \frac{L_i}{2} r_{\parallel} = L_i \frac{r_{\perp} + r_{\parallel}}{2} = L_i \rho \quad (2.20)$$

### 2.3.2 Diffuse Reflections

When subjected to rough surfaces, light scatters throughout the hemispherical volume seen in Figure(2.2). Such targets produce an equal radiance yield in all directions. Scattering that is perfectly uniform is known as Lambertian. This assumption implies that light intensity is directly proportional to the cosine of the angle between source light beams and a surface normal ( $\theta_i$ ). Where does this uniformity come from? The geometry of a rough surface is multifaceted. When many rays of light encounter these many facets, there is a high probability that photons will participate in multiple scatter events. It is the self shadowing of facets that redirects incoming light into the hemispherical exit lobe. A second factor that contributes to the *diffuseness* of scatter is subsurface scatter or radiative transfer. Radiation that is absorbed within a solid undergoes many scatter processes and can travel laterally below the surface. Light can escape the surface at spatial locations other than original illumination point. This progression instigates diffuse scatter.

### 2.3.3 Directional Diffuse Reflections

Light is rarely completely specular or diffuse. This means that most targets won't accurately be described by Fresnel reflections or a Lambertian lobe. Most glossy surfaces will produce a broadened lobe about the specular direction. The majority of rough surfaces

will exhibit a hemispherical lobe with a directional feature in the backscatter direction. Relatively uniform granular surfaces may be characterized by both backward and forward scattering reflectance lobes. Because the diffuse approximation rests on the idea of scatter uniformity, it is only a function of source light directionality through Lambert's cosine law, and the view/camera location ( $\theta_r$ ) is moot. To model directionally diffuse reflections that are seen frequently in nature, it is prudent to consider the directionality of incident radiation ( $\theta_i, \phi_i$ ) (note Figure(2.1)), surface geometry, and the directionality of surface leaving radiance ( $\theta_r, \phi_r$ ). This is discussed in detail in the following section.

## 2.4 Directional Scatter and BRDF

To better model the real world, directional scatter must be evaluated thoroughly. The relationship between the directional wavelength dependent irradiance ( $E(\theta_i, \phi_i, \lambda)$ ) on a plane and the directional wavelength dependent radiance ( $L(\theta_r, \phi_r, \lambda)$ ) leaving the plane is called the *bidirectional reflectance distribution function* (BRDF). The term *bidirectional* separates the BRDF from other reflectance functions discussed in this section. This metric is bidirectional because the directionality of the source illumination and the directionality of the sensor contribute to the radiance that reaches the sensor. BRDF is written below as a ratio.

$$\rho_{BRDF}(\theta_r, \phi_r, \theta_i, \phi_i, \lambda) = \frac{L(\theta_r, \phi_r, \lambda)}{E(\theta_i, \phi_i, \lambda)} [sr^{-1}] \quad (2.21)$$

Note that the BRDF has units of  $sr^{-1}$ . This is because it describes surface leaving radiance in a specific direction. To obtain the full amount of irradiance ( $W/m^2$ ) reflected into the hemisphere above a surface, simply integrate the the reflected radiance over the entire hemisphere.

To illustrate this process, consider a human observer looking at lake water. The position of the sun shining on the lake determines the amount of solar reflections or glint observed by the human visual system of the observer. Likewise, a human on the shore will observe a different representation of lake surface than a second onlooker traveling above the water in an aircraft. The bottom line is that directionality of the viewer and the illumination are important and should be considered.

*Directional hemispherical reflectance* (DHR) is a function of incident light direction and wavelength only. It has no dependency on viewer position and is described as the ratio

of total reflected irradiance to incident irradiance from a particular direction. DHR is a unit-less quantity and can be described in relation to BRDF.

$$\rho_{DHR}(\theta_i, \phi_i, \lambda) = \int_0^{\pi/2} \int_0^{2\pi} \rho_{BRDF}(\theta_r, \phi_r, \theta_i, \phi_i, \lambda) \cos\theta_r \sin\theta_r d\phi_r d\theta_r \quad (2.22)$$

For Lambertian surfaces, the above relationship can be reduced.

$$\rho_{BRDF}(\theta_r, \phi_r, \theta_i, \phi_i, \lambda) = \frac{\rho_{DHR}(\theta_i, \phi_i, \lambda)}{\pi} \quad (2.23)$$

*Hemispherical directional reflectance* (HDR) is a function of wavelength and surface leaving light direction only. It has no dependency on source light position and is described as the ratio of directional reflected irradiance to incident irradiance. HDR is a unit-less quantity and can be described in relation to BRDF.

$$\rho_{HDR}(\theta_r, \phi_r, \lambda) = \int_0^{\pi/2} \int_0^{2\pi} \rho_{BRDF}(\theta_r, \phi_r, \theta_i, \phi_i, \lambda) \cos\theta_i \sin\theta_i d\phi_i d\theta_i \quad (2.24)$$

The geometry of a target surface itself allows approximations to be made to the aforementioned reflectance functions. If a plane exhibits Lambertian properties, reflected radiance is uniformly distributed as it leaves the target. In this instance, viewer and source location do not matter and DHR is equivalent to HDR. As stated previously, surface roughness primarily determines the shape of the diffuse reflection lobe. *Roughness* is best understood as the compilation of many small micro-facets with varying surface normals. It is then appropriate to assume that each individual facet is subject to Fresnel reflections (Law of reflection). When many rays are considered over the spatial extent of a surface, light will reflect in many directions, creating the appearance of a volumetric lobe. This is pictured as specularly reflecting Light rays in Figure(2.3).

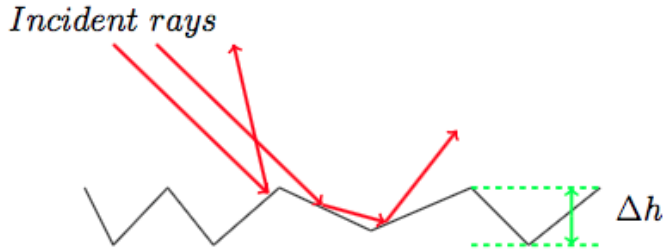


FIGURE 2.3: Microfacet scattering model.



In most models, facets are not considered individually. Instead, approximations are made about a surface based on the slope distribution of facets or the geometric similarity between all of the surface faces. In Figure(2.3),  $\Delta h$  represents the root-mean-square surface irregularity. This is just one way to model facets.

## 2.5 Directional Emissivity

Equation(2.7) alludes to the temperature dependence of emissivity. *Directional spectral emissivity* is a more general form of this equation that also includes directional and wavelength components.

$$\varepsilon(\theta, \phi, \lambda, T) = \frac{L_{\lambda\varepsilon}(\theta, \phi, T) \cos\theta d\Omega d\lambda}{L_{\lambda}^{BB}(\theta, \phi, T) \cos\theta d\Omega d\lambda} \quad (2.25)$$

$L_{\lambda\varepsilon}$  is surface leaving radiance.  $\Omega$  is the solid angle of interest and  $L_{\lambda}^{BB}$  is the radiance of a perfect blackbody.

## 2.6 Reflection Components of the Beard-Maxwell Model

There is one great inconvenience that makes the reflectance modeling process so difficult. It is the issue of generality. All object facets reflect light, but in different ways. This makes the description of reflectance hard to define. Analysts have found over time that an easy way to engineer good reflectance depictions is to use recorded data from natural scenes to create mathematical models with variable fitting parameters. These fitting parameters are then changed so that the same general function will describe multiple surfaces. This is how reflection is perceived in the minds of most humans; as a single process that all surfaces are subject to.

The Beard-Maxwell model is a set of general functions used to describe the reflectance from a faceted surface. As discussed above, this model has a general functional form which describes different surfaces by changing fitting parameters. The benefit of the Beard-Maxwell model is that these parameters have physical meaning and can be measured. Many models use arbitrary parameter values. This model also includes components which characterize the reflection modes from Section(2.3). The BRDF is written as a linear combination of specular reflectance ( $\rho_s$ ), diffuse reflectance ( $\rho_d$ ), and a volumetric reflectance ( $\rho_v$ ). Specular reflectance has angular dependencies where the diffuse and volumetric components are assumed to be uniformly distributed.

$$\rho_{BRDF}(\theta_r, \phi_r, \theta_i, \phi_i, \lambda) = \rho_s(\theta_r, \phi_r, \theta_i, \phi_i, \lambda) + \rho_d(\lambda) + \frac{2\rho_v(\lambda)}{\cos\theta_i + \cos\theta_r} \quad (2.26)$$

The specular term in the above equation is a function of the Fresnel reflections ( $R(\theta_s, n(\lambda), \kappa(\lambda))$ ) at each facet, and the standard deviation of all the slopes that make up the scene surface ( $\sigma_s$ ).

$$\rho_s(\theta_r, \phi_r, \theta_i, \phi_i, \lambda) = B \frac{R(\theta_s, n(\lambda), \kappa(\lambda))}{4\cos\theta_n\cos\theta_r\cos\theta_i} \frac{1}{\sigma_s^2 + \tan^2\theta_n} S(\theta_s, \theta_n) \quad (2.27)$$

Where  $\theta_n$  is the angle between the surface normal and the effective specular normal. This angle is surface dependent.

$$\theta_n = \cos^{-1} \left[ \frac{\cos\theta_i + \cos\theta_r}{2\cos\theta_s} \right] \quad (2.28)$$

Where  $\theta_s$  is effective specular reflectance angle. This is the angle between the effective specular normal and the angle of reflection.

$$\theta_s = \frac{1}{2} \cos^{-1} [\cos\theta_i \cos\theta_r + \sin\theta_i \sin\theta_r \cos(\phi_r - \phi_i)] \quad (2.29)$$

Finally,  $S(\theta_s, \theta_n)$  represents shadowing effects that facets have on one another. The line of sight from facet to illumination source or from facet to detector is often blocked by other facets or macrofeatures if the illuminator or detector sits low in the sky.

$$S(\theta_s, \theta_n) = \frac{1 + \frac{\theta_n}{\Omega} e^{-2\theta_s/\tau}}{1 + \frac{\theta_n}{\Omega}} \quad (2.30)$$

Here,  $\tau$  and  $\Omega$  are fitting parameters. When a regression is performed using Equation(2.27) and collected data, these parameters are changed to best represent the specific surface characterized by the data.

## 2.7 Ground and Pupil Plane Radiance

Scene images include all of the light that reaches the focal plane of a sensor. Not all of this radiation emanates from the primary light source, and not all of the light attributed to that source follows a direct path from source to target to sensor. Figure(2.3) used

rays of photons to illustrate the illumination of a rough target. The actual number of rays emitted from a source are innumerable, and photon interaction with the atmosphere and in-scene surfaces is complex. When light strikes objects sitting within the line of sight of a target, these objects become secondary sources themselves. The radiance that is detected at the pupil plane of a sensor will include contributions from these adjacent objects and light that is emitted from the atmosphere.

It is useful to compartmentalize the different components of radiation in a scene. This way all light can be accounted for. The *governing equation* of radiometry is used to keep track of the light that leaves a target and is observed at the pupil plane of the remote sensor. This sensor reaching radiance is unique to the geometric and radiometric conditions of a scene, and is therefore a signature that can be used to differentiate scenes or targets.

In the following explanation, targets are assumed to be single facets with distinct BRDFs ( $\rho$ ) described using a spherical coordinate system. Light that travels down to the target plane from sources such as the sun or atmosphere is termed *downwelling* ( $L_d$ ). Radiation traveling towards the remote sensor from below is called *upwelling* radiance ( $L_u$ ). Direct solar radiance will be described using an angular notation of  $(\theta_s, \phi_s)$ , while the view direction is denoted using  $(\theta_r, \phi_r)$ .

It was stated earlier in Chapter(2) that radiation leaves a target at the ground plane through processes of reflection ( $L_r$ ) and emission ( $L_e$ ). Radiance upwelling ( $L_u$ ) from the ground plane of the coordinate system is a linear combination of these two processes.

$$L_u(\lambda) = L_e(\theta_r, \phi_r, \lambda) + L_r(\theta_r, \phi_r, \lambda) \quad (2.31)$$

The emitted component of the equation above can be written using Kirchoff's law by subtracting the *directional hemispheric radiance* (DHR) from unity. This emissivity is then multiplied by the blackbody spectral radiance distribution ( $B(\lambda, T)$ ).

$$L_e(\lambda) = B(\lambda, T) \left[ 1 - \int_0^{2\pi} \int_0^{\pi/2} \rho_{BRDF}(\theta_r, \phi_r, \theta, \phi, \lambda) \cos\theta \sin\theta d\theta d\phi \right] \quad (2.32)$$

The reflected component is described using the linear combination of direct solar irradiance ( $E_s$ ) and the diffuse downwelling radiance from the atmosphere ( $L_d$ ).

$$\begin{aligned}
L_r(\lambda) &= \rho_{BRDF}(\theta_r, \phi_r, \theta_s, \phi_s, \lambda) E_s(\theta_s, \phi_s, \lambda) \\
&+ \int_0^{2\pi} \int_0^{\pi/2} \rho_{BRDF}(\theta_r, \phi_r, \theta, \phi, \lambda) L_d(\theta, \phi, \lambda) \cos\theta \sin\theta d\theta d\phi \quad (2.33)
\end{aligned}$$

As light travels between the ground plane and the pupil plane of the detector, it encounters the atmosphere. The fraction of light upwelling from the ground plane that reaches the detector is the product of the atmospheric transmission ( $\tau_a(\lambda)$ ) and the upwelling radiance ( $L_u$ ). Transmission is a value between zero and one. This indicates that light decreases in intensity as it travels between surface and sensor. However, there is also an additive process of path radiance ( $L_a$ ) that must be considered in the math. This suggests that radiance reaching the remote sensor ( $L_p$ ) could in fact be greater than or equal to the amount leaving the target plane.

$$L_p(\lambda) = \tau_a(\lambda) L_u(\lambda) + L_a(\lambda) \quad (2.34)$$

The emissive and reflective components of the upwelling radiance ( $L_u$ ) can be written with respect to the specular, diffuse and volumetric components. BRDF is written in component form below.

$$\rho_{BRDF}(\theta_r, \phi_r, \theta, \phi, \lambda) = \rho_s(\theta_r, \phi_r, \theta, \phi, \lambda) + \rho_d(\lambda) + \frac{\rho_v(\lambda)}{\cos\theta + \cos\theta_r} \quad (2.35)$$

Kirchoff's law is used once again to describe each emissivity component.

$$\begin{aligned}
L_e(\lambda) &= B(\lambda, T) \left[ 1 - \int_0^{2\pi} \int_0^{\pi/2} \rho_s(\theta_r, \phi_r, \theta, \phi, \lambda) \cos\theta \sin\theta d\theta d\phi \right] \\
&+ B(\lambda, T) [1 - \pi\rho_d(\lambda)] \\
&+ B(\lambda, T) \left[ 1 - \rho_v(\lambda) \int_0^{2\pi} \int_0^{\pi/2} \frac{\cos\theta \sin\theta}{\cos\theta + \sin\theta_r} d\theta d\phi \right] \quad (2.36)
\end{aligned}$$

Then the reflection component is written with respect to solar irradiance ( $E_s$ ) and the diffuse downwelled radiance ( $L_d$ ).

$$\begin{aligned}
L_r(\lambda) &= \rho_s(\theta_r, \phi_r, \theta_s, \phi_s, \lambda) E_s(\theta_s, \phi_s, \lambda) \\
&+ \int_0^{2\pi} \int_0^{\pi/2} \rho_s(\theta_r, \phi_r, \theta, \phi, \lambda) L_d(\theta, \phi, \lambda) \cos\theta \sin\theta d\theta d\phi \\
&+ \rho_d(\lambda) \left[ E_s(\theta_s, \phi_s, \lambda) + \int_0^{2\pi} \int_0^{\pi/2} L_d(\theta, \phi, \lambda) \cos\theta \sin\theta d\theta d\phi \right] \\
&+ \rho_v(\lambda) \left[ \frac{E_s(\theta_s, \phi_s, \lambda)}{\cos\theta_s + \sin\theta_r} + \int_0^{2\pi} \int_0^{\pi/2} L_d(\theta, \phi, \lambda) \frac{\cos\theta \sin\theta}{\cos\theta + \cos\theta_r} d\theta d\phi \right] \quad (2.37)
\end{aligned}$$

### 2.7.1 Approximations to the Governing Equation

The math in Equation(2.37) and Equation(2.38) can be reduced if the approximation of Lambertian facets is made. Uniform reflection implies that there is no difference between diffuse scatter and volumetric scatter, and that  $\rho_d = \rho_{HDR} = \rho_{DHR}$ . The volumetric scatter component ( $\rho_v$ ) is set to zero. The pupil-reaching radiance is then written in condensed form.

$$\begin{aligned}
L_p(\lambda) &= \tau_a(\lambda) L_u(\lambda) + L_a(\lambda) \\
&= \tau_a(\lambda) (L_e(\theta_r, \phi_r, \lambda) + L_r(\theta_r, \phi_r, \lambda)) + L_a(\lambda) \\
&= \tau_a(\lambda) [1 - \rho_{DHR}(\lambda)] B(\lambda, T) \\
&+ \frac{\tau_a(\lambda) \rho_{DHR}(\lambda)}{\pi} [E_s(\theta_s, \phi_s, \lambda) + E_d(\lambda)] + L_a(\lambda) \quad (2.38)
\end{aligned}$$

Where  $E_d$  is the integrated downwelling radiance from Equation(2.38). The directionality of the downwelling radiance can be ignored as it is uniform in most instances.

$$E_d(\lambda) = \int_0^{2\pi} \int_0^{\pi/2} L_d(\theta, \phi, \lambda) \cos\theta \sin\theta d\theta d\phi \approx \pi L_d(\lambda) \quad (2.39)$$

The  $\pi$  in the above equation is conditional based on the assumption that there is no shadowing of the target facet and the hemisphere above the facet is unobstructed. When shadowing does exist, the  $\pi$  in Equation(2.40) is replaced with  $\Omega$ . This new term is called the *sky fraction* and takes on values between 0 and  $\pi$ . As  $\Omega$  approaches  $\pi$  the target facet becomes less obstructed.

### 2.7.2 Pupil Plane Radiance in the VNIR/SWIR

The VNIR and SWIR represent the reflective spectral bandwidth. Here, the process of reflection dominates emissivity. The pupil-plane radiance ( $L_p$ ) can be tailored to describe this natural tendency. The emissive term is neglected from Equation(2.39)

$$L_p(\lambda) = \frac{\tau_a(\lambda)\rho_{DHR}(\lambda)}{\pi} [E_s(\theta_s, \phi_s, \lambda) + E_d(\lambda)] + L_a(\lambda) \quad (2.40)$$

### 2.7.3 Pupil Plane Radiance in the LWIR

The LWIR represents the emissive spectral bandwidth. In the longwave region, the irradiance of visible light sources (the sun) is dominated by emitted radiation. Therefore, the specular solar reflective term is dropped from Equation(2.39). Diffuse downwelling radiance remains a contributing factor to pupil-plane radiance.

$$L_p(\lambda) = \tau_a(\lambda) [1 - \rho_{DHR}(\lambda)] B(\lambda, T) + \frac{\tau_a(\lambda)\rho_{DHR}(\lambda)}{\pi} E_d(\lambda) + L_a(\lambda) \quad (2.41)$$

In the LWIR and MWIR, the *sky fraction* approximation for facet obstructions is not valid. Objects that shadow facets are emissive in the MWIR/LWIR and the presumption that downwelling radiance scales with a factor of zero to  $\pi$  is ill-posed.

### 2.7.4 Pupil Plane Radiance in the MWIR

In the midwave region of the spectrum, processes of reflection and emission are prevalent. The governing equation can be altered for day and night MWIR detection. During daylight hours, solar and diffuse irradiance are detected along with emitted radiation; Equation(2.39) must be used. At night, Equation(2.42) can be used to the pupil-plane radiance in the MWIR.

### 2.7.5 Pupil Plane Radiance For a Virtual Goniometer

Most goniometric measurements are made within meters of the target of interest. Atmospheric transmission and path radiance are negligible in this case. The general form of goniometric sensor reaching radiance can be written by neglecting  $\tau_a$  and  $L_a$ .

$$L_p(\lambda) = [1 - \rho_{DHR}(\lambda)] B(\lambda, T) + \frac{\rho_{DHR}(\lambda)}{\pi} [E_s(\theta_s, \phi_s, \lambda) + E_d(\lambda)] \quad (2.42)$$

## Chapter 3

# Background

### 3.1 Modeling Tools

#### 3.1.1 Blender Physics Engine

Creating accurate models of nature requires very good synthetic scene generation. Many computer-aided design (CAD) softwares give users the ability to etch, bend and connect different shapes or planes to create objects with precision. Entire target scenes can be created by deliberately placing CAD objects within a virtual three-dimensional space in an attempt to mimic reality.

For example, creating a scene of sand might require the design of several different particles that are cloned, rotated and individually placed with respect to one another in the form of a sand pile.

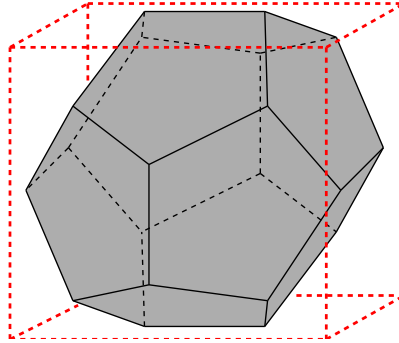
A sand scene might be comprised of thousands of objects. Placing each object individually would be incredibly tedious and time consuming. Even if users had the ability to place the objects quickly, could they be posed in a physical fashion that realistically represents nature?

Using Blender 3-D built-in physics engines, one can create a scene of objects that interact based on the physical properties (mass and shape) defined by the user. The simulation of rigid body collisions, fluid motion, and force field interactions can all be accomplished using Blender 3-D. Each mesh object in a Blender 3-D virtual scene is subject to friction and damping.

Individual mesh facets influence collisions between in-scene objects. This implies that a convex hull does not define the physical bounds of a soil particle created in Blender



3-D. For instance, a multi-faceted particle is bounded by its facets rather than a sphere or a six-sided cube with similar volume (Figure(3.1)).




---

FIGURE 3.1: A mesh object (gray) with convex hull (dashed red). Blender allows for mesh interactions rather than just using a convex hull for physics simulations

### 3.1.2 DIRSIG

Scenes developed using the aforementioned Blender 3-D tool can be thought of as a superposition of many flat facets. Using the Digital Imaging and Remote Sensing Image Generation Tool (DIRSIG), computational radiometry is applied to each facet in a scene through ray tracing (Schott, 2007). This allows for the construction of models from first principles through the numerical assembly of facets. Temperature, illumination, scene geometry, and sensor configuration are all defined by the DIRSIG user (Eismann, 2012). The output of any DIRSIG simulation is a synthetic image. The signal at each pixel in the image corresponds to spectral radiance that is detected by the DIRSIG sensor. As this radiance can be attributed to visible or infrared radiation, target reflectance and emissivity can be calculated from this data.

DIRSIG images are dependent upon user selected sub-models. Such inputs might include reflectance properties to be assigned to facets or atmospheric data which may modify the intensity of light reaching the DIRSIG sensor. Cameras can also be created and modified virtually within the DIRSIG environment. Users must also select parameters of solar position and target view angle in order to initialize ray tracing and data collection. Each preset parameter is gathered and correctly implemented through the execution of a simulation file.

The compartmentalization of DIRSIG data inputs allows for remote sensing experimentation. This research includes the analysis of novel DIRSIG scenes using standardized

radiometry and material properties. These scenes are a collection of facets oriented in three-dimensional space. Unique material properties can be assigned to every individual facet in a scene. Why is this important? With the ability to make individual reflectance assignments, scenes of mixed solids and contaminated surfaces can be modeled with respect to radiometry and geometry.

### 3.1.3 NEFDS

In order to accurately model a realistic scene, the appropriate geometry and material properties must be used. Defining the reflectance of pure materials (much less mixed solids) is a complicated process. Most naturally occurring materials are comprised of asymmetric particles arranged in an asymmetric orientation. This leads to directionally varying reflectance. In DIRSIG, scenes are evaluated at changing target view angles and illumination positions. Thus, the assignment of correct reflectance properties is imperative if realistic signatures are to be obtained using models.

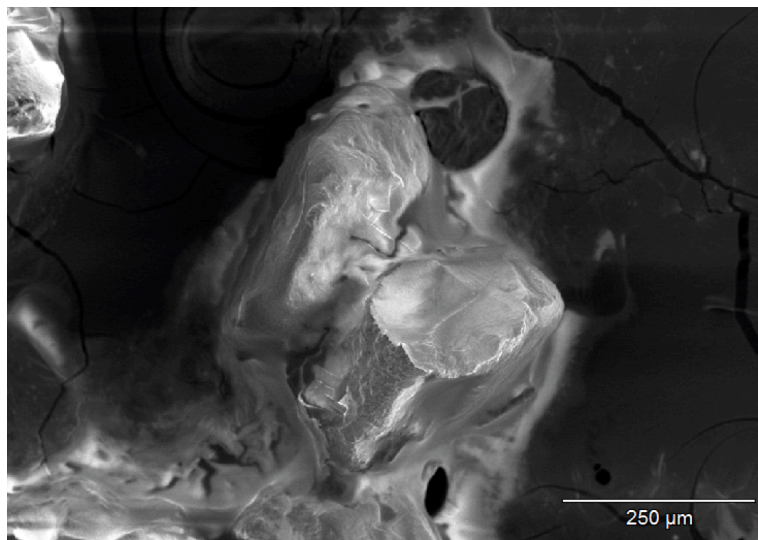
Spectral libraries are a good place to obtain directionally accurate material data. One such library that includes BRDF signatures of many materials is the Nonconventional Exploitation Factors Data System (NEFDS). The NEFDS provides a standardized database of reflectance information. To obtain this data, the National Geospatial-Intelligence Agency (NGA) has selected and examined twelve target categories containing more than 400 different materials and mixtures. Each material in the database has been measured goniometrically using precisely calibrated sensors and experimental procedures. Laser polarization measurements in the specular and backscatter directions provide data that can be used to tease out descriptions of specular, diffuse and volumetric scatter. Using the Beard-Maxwell BRDF model paired with these measured data points, regression is performed to find the optimal reflectance coefficient for each view angle at every illumination position. Because there are a large number of free parameters in this BRDF model, and these parameters correspond to physical material properties, NEFDS parameters tend to closely mimic experimental observations. The actual NEF product is a list of BRDF parameters for each specific measurement of each target in the database. NEFDS measurements are performed at multiple wavelengths, providing a measuring stick for wavelength dependent results produced using synthetic DIRSIG scenes.

### 3.1.4 Electron Microscopy

Even if DIRSIG can accurately simulate the radiometry for most remote sensing scenarios, output images will be poor representations of reality if the input scenes are dissimilar

to actual targets of interest. As discussed in section 3.1.1, Blender can be used to create pseudo targets. It is important that these reconstructions look physical.

Electron microscopy provides high resolution target images which can be used to create 3-d Blender prototypes for DIRSIG. The figure below is a mixture of sand and a calcium chloride solution.



---

FIGURE 3.2: Scanning electron microscope (SEM) image of sand mixed with a calcium chloride solution

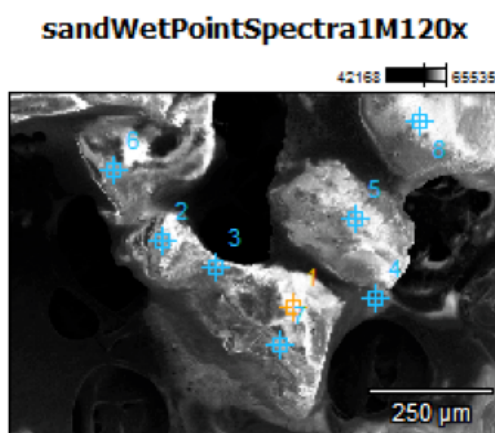
#### 3.1.4.1 Electron Microscopy Principles

To create an electron microscope image, a target specimen is first bombarded with an electron beam generated by an electron gun. In the case of the scanning electron microscope (SEM), this beam is scanned raster style across the specimen. As the beam electrons impinge upon the specimen, multiple effects occur. If the target is dense and has a high atomic number, beam penetration will be small and it is likely that many beam electrons will find their way back out of the specimen to be detected by a photo-multiplier tube (PMT) or charge coupled sensor device (CCD). It is also likely that the electron beam may loosen outer (weakly bound) electrons which can also escape the specimen and contribute to imaging. This is known as secondary electron imaging. By changing the electron beam probe diameter, current, divergence angle and voltage, users may maximize image resolution, contrast and depth of focus.

### 3.1.4.2 X-Ray Microanalysis

If a specimen of mixed materials is being observed (Figure 3.2 for example), it is important that each material in the mixture can be identified. When synthetic Blender scenes are crafted, it is crucial that the appropriate reflection and emission properties are assigned to each facet. Using X-Ray microanalysis, the correct material make-up of each portion of a specimen can be found (Figure 3.3).

(A)



(B)

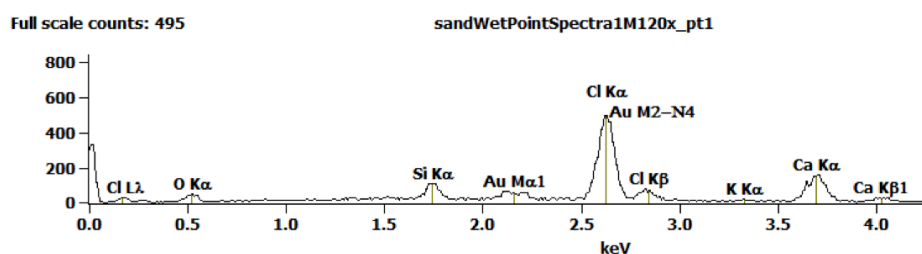


FIGURE 3.3: (Top) Cross hairs indicate points on the specimen chosen for microanalysis. (Bottom) Histogram of X-Ray signal with energy for cross hair number 1.

Histograms such as the one in Figure 3.3 indicate the relative proportions of the elemental make-up at specific geometric positions on a target specimen. This specific histogram corresponds to point one (highlighted in yellow) of the SEM image. The specimen being analyzed is sand mixed with a calcium chloride solution. The histogram includes large

peaks corresponding to calcium and chlorine that indicate the presence of these elements at point one in the image. The small silicon peak reveals the presence of sand beneath the calcium chloride solution. This material information gives guidance as to how such a target should be modeled. It can be assumed that since the quantity of calcium chloride dominates that of silicon at this point, the material properties of *CaCl* should be assigned to the corresponding facets of a Blender replica model. Many points on the target should be analyzed in order to make accurate material assignments within a synthetic scene.

These informative histograms are generated through the detection of X-Ray emissions. Atomic bonds of particles within a specimen include tightly bound inner-shell electrons and loosely bound outer electrons. When the electron beam of an SEM impinges upon a specimen, inner electrons are energized and elevated to outer atomic energy shells. As electrons make this transition between energy levels, X-Rays are emitted corresponding to the energy difference between the initial and final energy states. The geometry of each atomic element produces specific X-ray energies, and by the quantity of this energy, individual elements can be identified.

## 3.2 Mixed Solid Targets

A primary goal of this research is to model non-pristine materials and targets that have been subjected to contamination. The ability to perform simulations on weathered materials is desired because it is not always practical to perform *in situ* measurements. The geometry of *in situ* targets is not always transferable to laboratory measurement devices without modifying surface characteristics. This problem may be circumnavigated through the use of virtual scene simulations. With Blender, it is possible to deposit contaminating particles using methods that preserve the geometric integrity of a scene.

### 3.2.1 Soil Particles

Creating a target of homogeneous soil particles is a preliminary study that must be performed before complex scenes are developed. A soil scene provides a testbed upon which the Blender physics engine can be explored without the added complexity of material mixtures. Modeling a plane with realistically oriented sand particles was the aspiration for *Soil Scene 1*.

Considerations must be made in order to accurately model soils as particles. These characteristics include: the size distribution of particles, the chemical makeup of soil, the shape and surface area of soil and the arrangement of individual particles.

The chemical makeup of targets in DIRSIG is obtained from databases of materials measured in goniometric fashion. The reflectance information from a database is applied individually to facets in a synthetic scene to produce radiometric ray-trace results that are consistent with each material being modeled.

Soil size distribution is a well probed characteristic. The diameter of sand particles vary in size between  $0.05mm$  and  $2mm$  Ben-Dor et al. (1999). Clay and silt have diameters less than  $0.05mm$ . Particle size has much to do with the ability of a surface to hold water and settle into a state of equilibrium. Stokes law indicates that larger particles should settle faster than smaller particles.

Shape and surface area of soil can be described as soil structure. This characteristic describes how soil particles aggregate or stick together. This is dependent upon the chemical makeup of soils as well as total charge balance between cations and negatively charged soil particles. Soil structure determines pore spacing which is directly related to amount of water and gas flow within a target. The stability of pore spacing is dependent upon wetting, climate and disintegration of organic soil components. Compaction of soils is the result of pore structure deterioration. This change in soil can impact detected soil spectra Ben-Dor et al. (1999).

It is soil structure that is most difficult to simulate. Porosity is difficult to create synthetically. However, force-mass interactions of charge and wind can be imitated in blender. Soil density can be altered by varying the size distribution of particles in a scene.

### **3.2.2 Soil Particles With Chemical Contaminants**

When dealing with mixed materials, a linear combination of constituents is often used to define their radiometry. This is a bad approximation for two reasons. First, the assumption of a linear combination ignores backscatter, which is a primary and defining component of target reflectance signatures. Second, linear combinations ignore intimate mixing that contributes to small scale shadowing and multi-bounce optical effects.

To better model soils contaminated with chemicals, the structure and chemical content of aggregated particles should be investigated and recreated with precision.

A survey conducted by the U.S. Department of Transportation and the Federal Highway Administration (Kociolek, 2013) gives insight into the machinery and chemicals used to treat and maintain dirt roads. Chemical road treatments are performed by 73% of county, state and federal agencies in the United States. Most treatments consist of a liquid chemical spray or a solid mixture process. Chemicals used most commonly in solid and liquid form include magnesium chloride ( $\text{MgCl}$ ) and calcium chloride ( $\text{CaCl}$ ).

To visualize the structure of soil-chemical mixtures, electron microscopy and X-Ray microanalysis can be employed. Figure 3.2 reveals the geometric consequences of treating sand particles with a calcium chloride solution. The prevalence of particle aggregation is evident and should be incorporated into synthetic scene designs.

### 3.2.3 Man Made Surfaces With Soil Contaminants

Man made targets are regularly contaminated by soil, dirt and dust. As the amount of contamination varies, the detected reflectance and emittance signature will also change. Though many manufactured targets are more specular than natural scenes, contamination can muffle this reflectance feature in unsystematic fashion. This can make spectral attributes of man made surfaces less obvious. Because of the volatility of surface weathering, there are many variable combinations of solids that have not been measured and recorded. Goniometric analysis of contaminated man made targets has been limited up to this point Kerekes et al. (2013), but such investigations are critical for target detection at off-nadir viewing positions.

### 3.2.4 Spectral Features of Soil Targets

Soil particles are comprised mostly of rock-forming minerals. These minerals, such as silica, are an agglomeration of ionic bonds. In the presence of external forces and charges, these bonds will vibrate. Fundamental molecular vibrations are known as *reststrahlen*, and the spectral reflectance features stemming from these vibrations are called reststrahlen bands. It has been observed (Lyon, 1964) that the spectral contrast (height of reststrahlen peak) of reststrahlen bands is dependent upon particle size. This contrast tends to decrease with decreasing particle size. A plot exhibiting reststrahlen bands and spectral contrast is displayed in Figure (3.4). Other observations by Salisbury and Wald (1992) and Johnson et al. (1998b) suggest that porosity as well as size distribution impact the size and shape of reststrahlen bands.

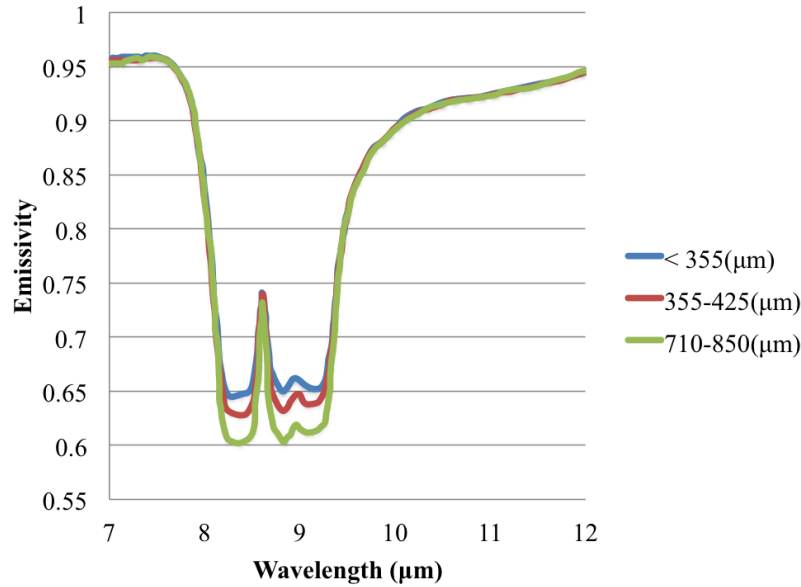


FIGURE 3.4: Emissivity plot representing three different soil particle sizes. Data is adopted from Deloye et al. (2011). Note that the spectral contrast increases with particle size within the  $8.2\mu\text{m}$  -  $9.5\mu\text{m}$  window.

Soil comprised of exclusively smaller grains is less porous than a target composed of larger solid grains. When photons impinge upon a finely powdered target, they penetrate the surface between particles and undergo multiple light-matter interactions. After several bounces, light that does manage to reflect back out of the powder could be traveling in nearly any hemispherical direction. Therefore, the decrease in spectral contrast described above coincides with the increase in diffuse volumetric scattering Vincent and Hunt (1968), and the reduction of detection limits for target recognition.

It is not only aggregates of soil that impact the balance of specular, multiple, and volumetric scattering. Soil signatures simultaneously depend upon the individual grain geometry and wavelength dependent optical properties. Salisbury and Wald (1992) and Moersch and Christensen (1995) both describe the complex relationship between the geometry of a single soil grain, and the optical properties of soil. For example, quartz is characterized by nearly perfect emissivity at  $7.4\mu\text{m}$ . Both the index of refraction of quartz and the index of air are approximately equal to 1 at this wavelength. The result is the absence of grain boundaries and nearly perfect transmission. Particle size matters very little at this wavelength, and the coinciding signature is mostly influenced by the optical properties of quartz. Particle geometry becomes notable between  $8.2\mu\text{m}$  -  $9.5\mu\text{m}$ . In this region, the imaginary portion of the complex index of refraction is



very large compared to the real coefficient. Consequently, radiation traveling through quartz is subject to severe path loss. Compared to larger soil grains, smaller particles are more emissive at these wavelengths, and the radiation is largely volume scattered. There is a greater chance for radiation to be emitted from small quartz grains because photons will encounter more grain boundaries before it is reabsorbed or converted to heat. The added boundary interactions provide more preabsorption opportunities for emission. This illustrates the complex relationship that geometry and optical properties have upon scattering modes.

Additionally, small particles often cling to larger particles of sand and soil. Observations of large particles covered with fine particles reveal additional diffuse volumetric scatter (Salisbury and Wald, 1992, Johnson et al., 1998b). In fact, fine particle coatings are found to scatter independently and incoherently. This behavior is dissimilar to the reflection of tightly packed particles which act as an optically thick surface and scatter light coherently. Not only does incoherent scatter lead to decreased spectral contrast, it also alters the shape of the reststrahlen bands. Clean soil particles have smooth rounded reflectance peaks while smaller particles or unwashed particles have flat reflectance features. This implies that the shape of a soil spectral curve will be defined by the reflectance of fine particles if they are present.

It has been shown that human interaction and weathering alters the geometric description of soils (Johnson et al., 1998b). Dirt and sand that is undisturbed by humans is subjected to wind, rain, dew and temperature cycling. These processes tend to wash away superficial particles, and the particle size distribution at the optically active layer does not include the fine particle coatings that were previously discussed. In situ measurements of disturbed soil do include many small (5-75 micron) particles that adhere to larger grains. The inclusion of these leeching dust specks leads to an increase in volume scatter and a strong increase in the emissivity of disturbed soil. The relationship between emissivity and wavelength of different soil scenarios is shown in Figure (3.5).

Within the scattering process, there exists a delicate balance between porosity and the accumulation of small clinging particles. This was shown by Johnson et al. (1998b) in an effort to recreate the appearance of undisturbed soil by packing and tamping a dirty disturbed soil target. When disturbed soil is tamped, its porosity is reduced. Even so, packing disturbed soil does not yield a spectral signature similar to that of undisturbed soil. This is an indication that the scattering due to porosity and clinging fines are separate processes. Figure(3.5) displays an in situ representation of disturbed, tamped and undisturbed soil.

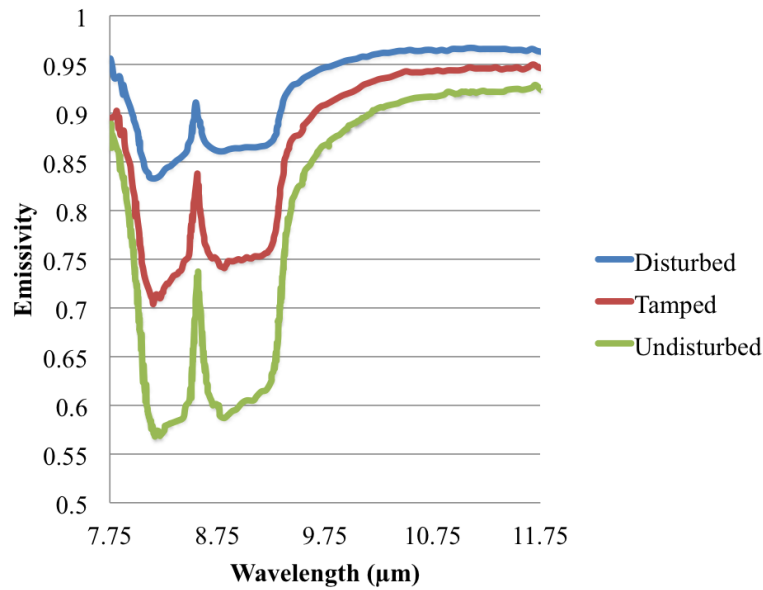


FIGURE 3.5: Emissivity plot representing disturbed, tamped, and undisturbed soil. Data is adopted from Johnson et al. (1998b).

Further, in situ disturbances are difficult to replicate. Spectral target analysis is often performed by evaluating field samples in a lab environment. However, the process of sieving causes fine particles to become detached from larger grains and the integrity of the field measurement becomes compromised. This also means that the collected spectra may be interpreted incorrectly. Although it is difficult to recreate disturbed soil, the *washed* appearance of an undisturbed target can be nearly recreated using a wet sieve process (Figure (3.6)).

It is not just the geometry and chemistry of a target that determines the signature that is captured by remote sensing. Radiation signatures are often directional, and the impacts of data collection methodologies are not negligible. In Figure (3.7), the quartz emissivity signature is shown to change with sensor viewing location in the zenith plane. Emissivity magnitude decreases in the reststrahlen bands when the sensor is positioned at large zenith angles. In comparing the plots in Figure (3.5) and Figure (3.7), it is clear that without an understanding of effects due to off-nadir viewing, one might confuse the signature of a target composed of large grains with that of an agglomeration of smaller grains. It is important to state that this view angle effect is incorporated into each measurement simultaneously with the physical phenomenologies due to optical properties, and target geometry. Before conclusions are drawn with respect to a signature, the impacts of remote sensing techniques and procedures should be understood.

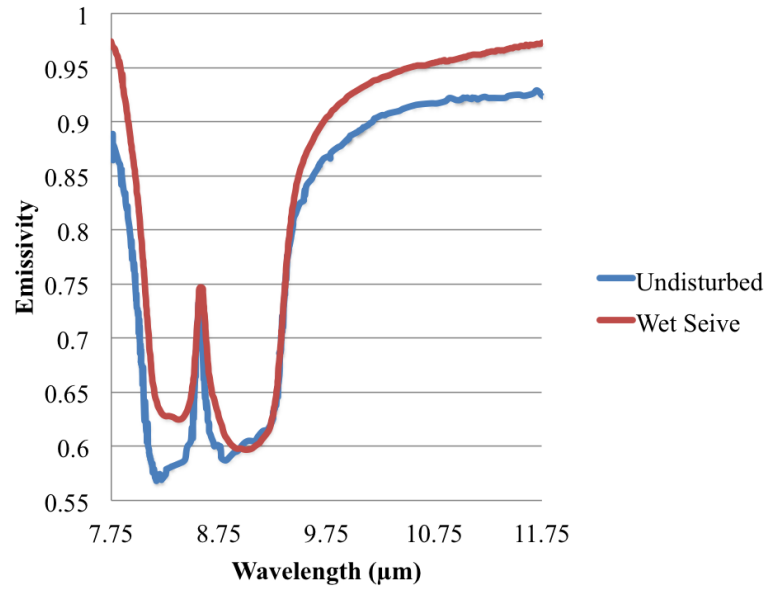


FIGURE 3.6: Emissivity plot shows an undisturbed field sample compared to a lab measurement that was wet seived. Data is adopted from Johnson et al. (1998b).

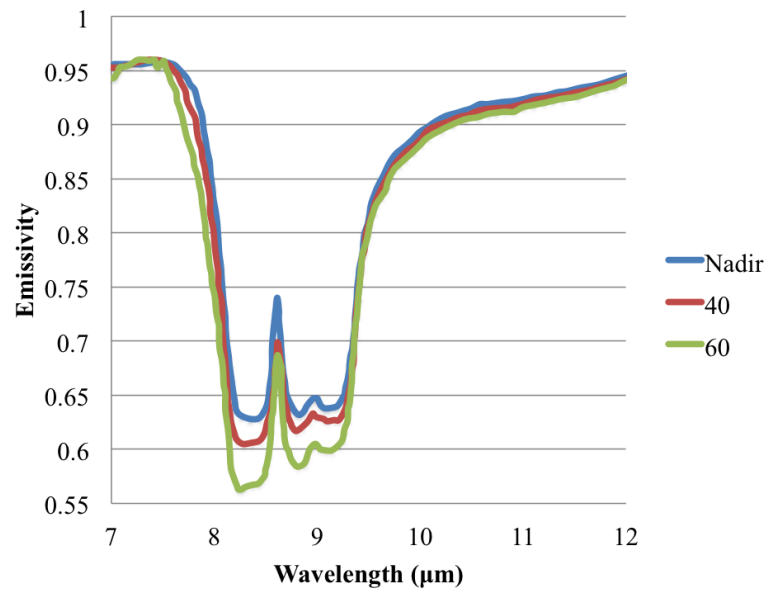


FIGURE 3.7: The emissivity signature of quartz changes with sensor location in the zenith plane. Emissivity magnitude is notably reduced in the reststrahlen bands as sensor zenith angle increases from  $0^\circ$  -  $60^\circ$ . Data is adopted from Deloye et al. (2011).

## Chapter 4

# Methodology

The generation and measurement of mixed solid materials is complex. The ultimate goal is to produce and measure a synthetic target with sensor reaching radiance that mimics in situ soil signatures. Recorded signal varies due to target geometry, chemical composition and scene radiometry. A process to incorporate all three of these variables into a verified physical model is the subject of this chapter. A methodology has been developed to create, measure and evaluate mixed solid targets.

The modeling process for the BRDF of soils has taken many forms. It has been described using geometric facets (Torrance and Sparrow, 1976, Maxwell et al., 1973), coherent backscattering theory (Mishchenko et al., 2006, 1999, Dlugach et al., 2011, Tishkovets et al., 2011), and radiative transport (Hapke, 2012b). Differences in models exist because the relationships between geometric, radiometric, and chemical parameters are not explicitly known. This could mean that phenomenology has been excluded from simulation. It might also indicate that the interactions between model parameters are related inappropriately in mathematical theory. For instance, it may be difficult to determine whether certain spectral features are the byproducts of optical properties, soil geometry, or a combination of both parameters (Moersch and Christensen, 1995). Even if optical parameters are well known, failure to integrate appropriate geometry may produce spectral signatures that do not represent measured observations.

It is important to state what this model is not. The method used in this work is not an attempt to mathematically integrate all of the variables and processes that result in the univariate measure of reflectance or emissivity. It does not calculate signatures from optical properties explicitly. It is not a parameter-based model containing arbitrary functions that are fit to data curves. This model does not define surface geometry as a probabilistic distribution of facets (Maxwell et al., 1973) or isotropic bulk densities

(Hapke, 2012a,b). It does not assume that a scene of thousands of irregular particles will scatter as a linear or weighted combination of individual phase functions solved independently of one another (Hapke, 2012a,b).

This is a model, which is focused on scene geometry, and simulates the reflectance of the complex mixtures of solids. This is an avenue to explore the phenomenology of particle size distribution, density, and intimate mixing. Most importantly, the model easily bundles together the chemical, radiometric, and geometric components of material signatures.

## 4.1 Scene Construction

The problem with most particle radiance models is that they rely on physical assumptions to come to a closed form analytic solution, or they are contrived by performing regressions with a limited number of particle scenes. By using the Blender 3-d graphic design software, geometrically precise scenes can be created. A virtual particle scene created in Blender 3-D is comprised of particles that look and act like solid particles. This scene need not rely on simple shapes to represent reality, but may contain multifaceted polygons that can be used to produce realistic soil approximations. Also, the computational nature of these scenes enables precise and tailorable target design. The ability to quickly and incrementally alter scenes is a luxury absent from the laboratory. The following steps describe how physically based Blender scenes are formed and prepared for radiometric simulation.

### 4.1.1 Microscopy

Before individual particles are created, they should be observed. In this way size distribution and facetization can be accurately represented. Since most soil particles have diameters between 2mm and  $50\mu\text{m}$ , microscopy is a useful tool. Figure (4.1) shows a scanning electron microscope (SEM) image of quartz based sand.

X-ray microanalysis was also performed using the SEM. When soil particles are bombarded with electrons, ionization of the internal atoms results in X-ray emission that coincides with a specific energy. By analyzing the detected energy, the material make-up of each facet surface can be determined. This also makes the modeling of contaminated soils possible. It provides both the geometry and disposition of particle groupings. Blender 3-D was used to generate a grain geometry contaminated with small dust particles (Figure (4.2)).

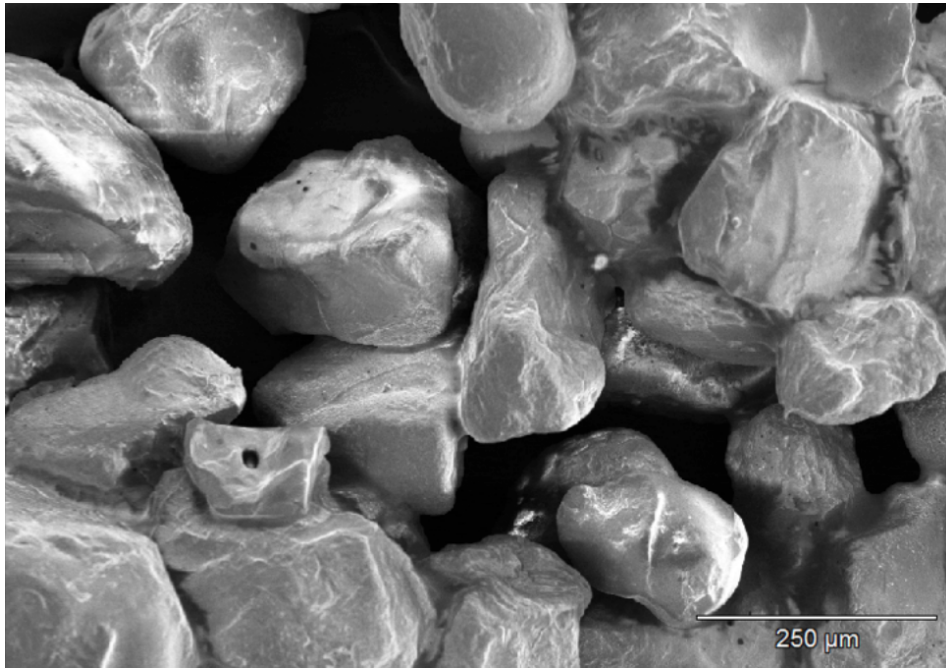


FIGURE 4.1: Silica based sand particles observed under a scanning electron microscope. Images like these provide templates for soil objects in Blender.

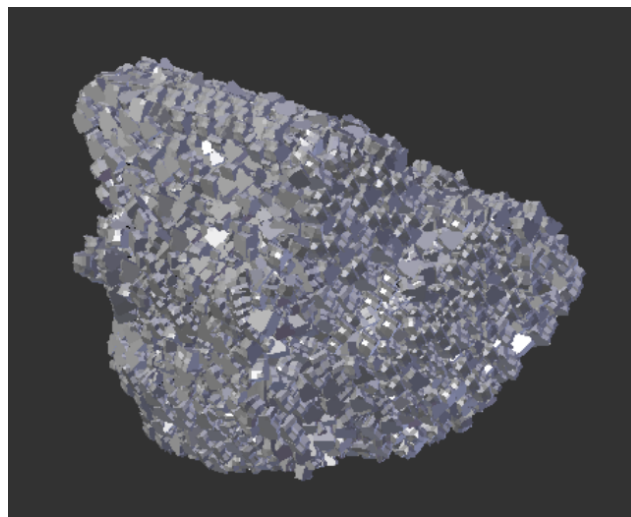


FIGURE 4.2: Blender model of a large soil grain contaminated with clinging fine particles.

### 4.1.2 Blender 3-D Modeling

As alluded to in the previous section, most of the scenes in this study begin at the micro level. Mesh objects of different geometries are rotated, translated and extruded to produce objects that match the 3-d geometry of granular targets.

Once the objects are created, material properties are assigned. Spectral signatures for many pure targets have been collected by Rochester Institute of Technology (RIT) and the United States Geological Survey (USGS). Another deep library that includes BRDF signatures of many materials is the Nonconventional Exploitation Factors Data System (NEFDS). Each individual facet of a Blender object can be assigned with spectral properties from any of these libraries. The goal of this research is to characterize mixed materials. By mixing facetized objects that have been assigned specific physical characteristics, mixed material spectra can be created.

The mixing process can be performed using the Blender 3-D physics engine. This software allows for objects in a scene to interact physically with one another. Instead of treating objects as convex hulls (Figure (4.3)), each grain in a scene possesses the face-tized shape crafted by the user. Mass, shape, gravity, electromagnetic forces and winds can all be included within simulations. To model a natural soil scene, particles are not individually placed by hand. They are treated as rigid bodies and are dropped onto a surface where they interact with each other and the surface itself. This creates a 3-dimensional scene, shown in Figure (4.3), that is more physical than those used in the derivation of many well known reflectance functions (Torrance and Sparrow, 1976, He et al., 1991, Nayar and Oren, 1995).

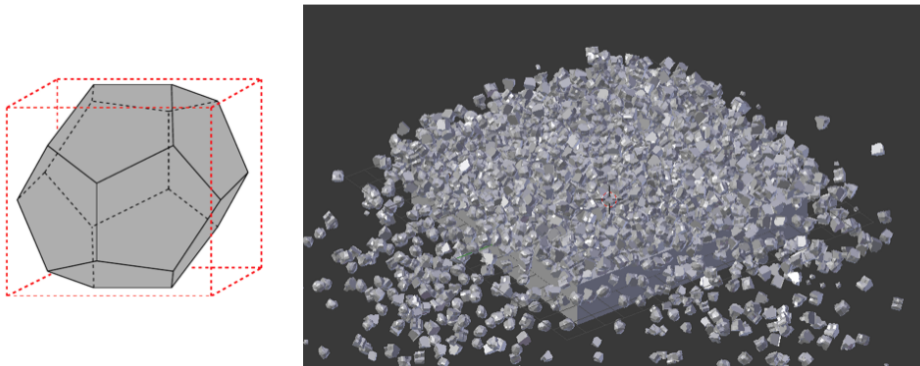


FIGURE 4.3: In Blender all object facets can interact in a scene rather than the red cubic convex hull shown on the left. Particles on the right fall and lay physically using the Blender physics engine

Soil scene simulations in Blender 3-D are motion pictures. At each frame, particle position is calculated using the mass, shape and external forces preprogrammed into the physics engine. A single frame from this motion picture is used to create a scene for radiometry simulation. Motion picture frames are exported from Blender 3-D as OBJ (.obj) files. These files include the numerical geometry that defines a scene. This includes the position in x,y,z coordinates of all object vertices. Object faces are defined as a collection of numbered vertices. The name of the material assigned to each face is also exported within the OBJ file.

### 4.1.3 ODB Files

The ODB file is the final geometric output of scene creation. Within this file, the basic units of length are defined. Also, scenes can be multiplied and patched together forming larger landscapes. Each motion picture frame can be translated, scaled and rotated with respect to a single point of origin. This reference frame is relayed to DIRSIG.

## 4.2 Virtual Hardware

In order to perform BRDF or directional emissivity analysis on virtual scenes, a virtual goniometer can be developed in DIRSIG. Ideally, all iterative hemispherical measurements should be performed and analyzed upon the execution of a single file. The construction of this file is the subject of this section. It includes the DIRSIG simulation file, shell-file construction, python editing and ENVI file analysis. The work flow for this process is displayed in Figure (4.4).

### 4.2.1 DIRSIG Simulation File

Once a scene has been created, exported and packaged as an ODB file, a DIRSIG simulation is performed to map the radiometric interaction between the scene, the environment and a sensor. These three variables are completely described within separate Extensible Markup Files XML files. These files can be modified using a python editor if one wishes to alter the scene, atmosphere or camera. The DIRSIG simulation file is an executable parent file that uses the scene, environmental and sensor information to perform a geometric ray trace of light from the source to the sensor and provide an output image. This output image is in the form of an ENVI image file. It can be observed and analyzed



using ENVI image display software, or it can be imported and manipulated within math scripting software such as Matlab or python.

#### 4.2.2 Shell File Creation

The shell file allows a user to define parameters of a DIRSIG scene and execute a radiometric ray trace. This file has the form of a bash script and initiates the execution of goniometric measurements. It can be executed from the command line and has four functions.

First, the execution of the shell file opens Matlab and initializes an output text file that will be used for analysis. This text file is a place holder for output radiance and wavelength values. It is initially left blank.

Next, the code allows the goniometer parameters to be set from the command line. These parameters are necessary DIRSIG inputs. They include the distance between the ground and imaging system, the angular resolution of the goniometer in azimuth and zenith, the position of the solar source, the total irradiance ( $W/cm^2$ ) emanating from the source, the balance between direct source illumination and hemispherical illumination and the name of the scene geometry file that will be subjected to the radiometry.

Third, a python editor executes DIRSIG simulation files. This editor is explained thoroughly in the next section.

Matlab is then triggered once again to calculate average radiance from the output Envi image files. It then appends the radiance and corresponding wavelength data to the output file created in step one.

In summary, this bash script contains the execution code for each step of the goniometric measurement.

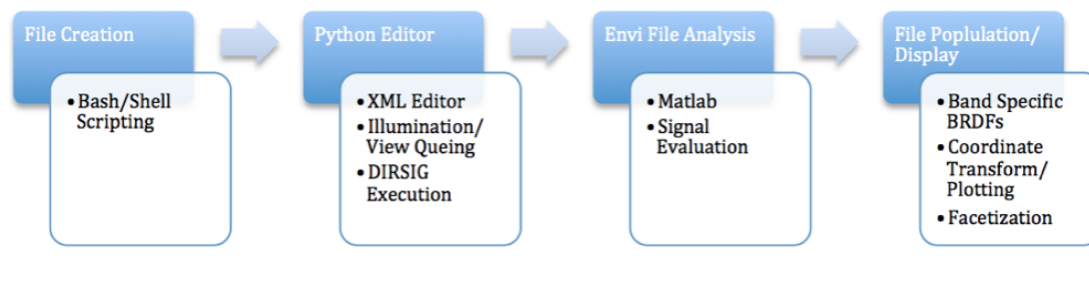


FIGURE 4.4: Workflow for the virtual goniometer tool.

### 4.2.3 Python Editor

A virtual goniometer could be formed using a bash script alone. However, making changes to the configuration would be tedious and the importance of a python editor can not be overstated. For without the editor, there exists a tool without a brain.

A full hemispherical goniometer measurement could require more than one hundred DIRSIG simulation runs. For each run, Extensible Markup Files (XML) files are called to provide scene, atmospheric, sensor and tasking information. The creation of all of these files is tedious and inflexible. Without the python editor, a change to the imaging platform focal length would require the user to edit an XML file for every simulation file in the batch. This might require handling more than one hundred simulation files individually.

The python XML editor provides a process for editing a single simulation file rather than hundreds. By using one simulation to queue each goniometric measurement, it becomes easy to change different aspects of the simulation. This includes measurement geometry, sensor specifications and the target scene.

The overarching function of this python file is to incrementally edit and execute a single DIRSIG simulation for each predefined sensor and source position. This way, a single file can be used to produce a multitude of measurements.

### 4.2.4 ENVI File Analysis

When DIRSIG is executed, it produces an image file (.img). The contents of this file depend on the imaging platform used in the simulation. Each device is sensitive to specific spectral bands. This means that a device will successfully convert scene photons to signal electrons for a specific and finite band of wavelengths. For each of these bandpass regions, image files contain radiance values ( $W/cm^2sr$ ) for each spatial pixel of the two-dimensional sensor array.

Sensors do not exhibit perfect sensitivity at all wavelengths. Every simulation photon that hits a detector does not necessarily result in a signal electron. Therefore, solving for BRDF requires compensation for device sensitivity. Detectors typically have spectral response functions that describe how efficiently photons are converted to signal over a range of wavelengths. Irradiance ( $W/cm^2$ ) at a specific wavelength is found by multiplying incoming flux by the response function at that same wavelength. This value of irradiance should be used in Equation (2.21) to solve for wavelength specific BRDF.

To come up with a single BRDF value for a bandpass region, seek the mean irradiance value. The total amount of signal that can actually be detected over a bandpass region is found by weighting the flux ( $\Phi_i(\lambda)$ ) by the entire response function ( $R(\lambda)$ ) and summing over all wavelengths.

$$S = \int \Phi_i(\lambda) R(\lambda) d\lambda \quad (4.1)$$

Gaussian shaped response functions are used in the DIRSIG default imaging platform. This platform has three bands corresponding to red, green and blue radiation.

A Matlab script was written to average sensor pixel values. Then, the code generates and applies response weighting functions for each bandpass region. These functions were each modeled with a Gaussian shape to match the DIRSIG sensor. A visual example of the response function model is shown in Figure (4.5). With recorded output radiance from DIRSIG, and appropriately weighted irradiance, Equation (2.21) can be evaluated for BRDF.

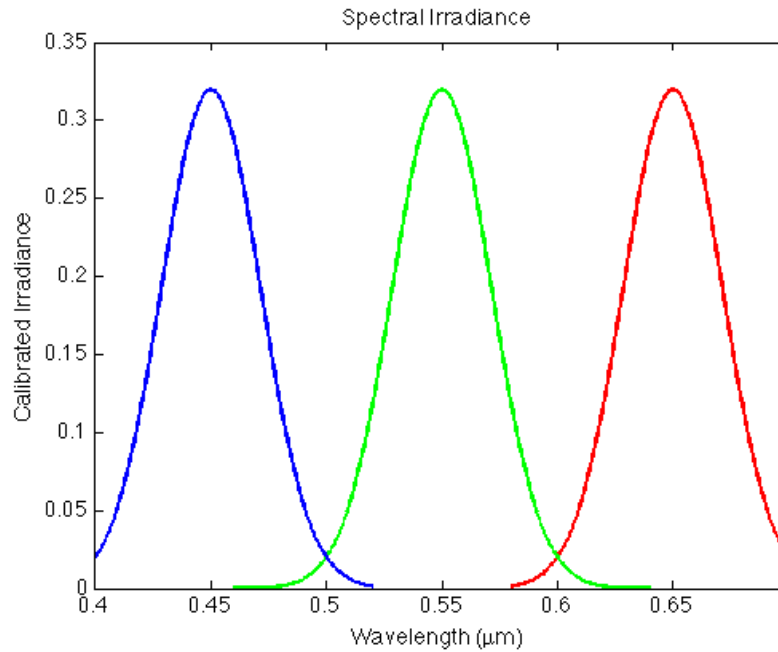


FIGURE 4.5: Example of R,G,B spectral response functions applied to scene irradiance.

### 4.2.5 Display

Directional reflectance and emissivity are metrics that can be used for target discrimination. Goniometric evaluation of these measurables requires 3 dimensions. Matlab does have a 3-D plot function, but it yields a 2-D image. Users can only view hemispherical plots from a single viewing angle and the plot can not be rotated. To create a more interactive 3-D representation of data, Blender 3-D modeling software can be employed. In addition to scene design suites, this software has a python scripting editor that can be exploited and used as a data plotter.

Creating 3-D plots is a three step process. First, it is important to realize that making measurements with a goniometer is a process performed in spherical coordinates. The sensor attached to any goniometer is positioned about a hemisphere in angular intervals. In contrast, Blender 3-D uses an X,Y,Z coordinate system. In order to plot hemispheric data with Blender 3-D, a coordinate transform is performed. Zenith angles are represented by  $\theta$  while  $\phi$  describes azimuth.

$$x = r \sin \theta \cos \phi \quad (4.2)$$

$$y = r \sin \theta \sin \phi \quad (4.3)$$

$$z = r \cos \theta \quad (4.4)$$

Once data is transformed to X,Y,Z coordinates, a python script is used to plot the values as vertices. The last step in the process is to render facets for the mesh of vertex data points. For every four vertices, a face is created.

The result is a 3-D mesh object that represents a collection of hemispheric data points. Users can rotate their view angle to observe the plot from all sides. One also has the ability to zoom in or out. Because the plots are Blender mesh objects, multiple plots can be displayed and viewed simultaneously. This can give the user a direct visual comparison of different signatures in 3-D.

An experimental suite was created in Blender 3-D to simulate a user interface for signature evaluation. The simulation makes use of the "Sun Position" Blender add-on. This tool includes information provided by NASA and NOAA that is used to report the position of the sun at any location on earth given the day and time. Users can input an observation time of interest and Blender 3-D will report the position of the sun in the sky. This source position can be used as an input to a functional reflectance model (or

DIRSIG) to obtain goniometric measurements. The data can then be plotted using the process described in the previous paragraphs.

For the purpose of this study, solar position was fed into a function developed by Nayar and Oren (1995) to describe the BRDF of sand. BRDFs were calculated and plotted as mesh objects for all hemispheric solar positions at five degree zenith and 10 degree azimuth resolution. Then, when a user selects a target location on earth and time of day, a python script reads in the solar position data and will display the BRDF mesh plot that most closely fits the sun position and target location. The target scene used in this simulation was a soil tire track. Figure (4.6) shows the Blender 3-D interface. These BRDF plots were not calculated in real time, but a function could be coded to perform that task. This demonstration is crude, but it shows that the Blender 3-D software can be used as a versatile display tool.

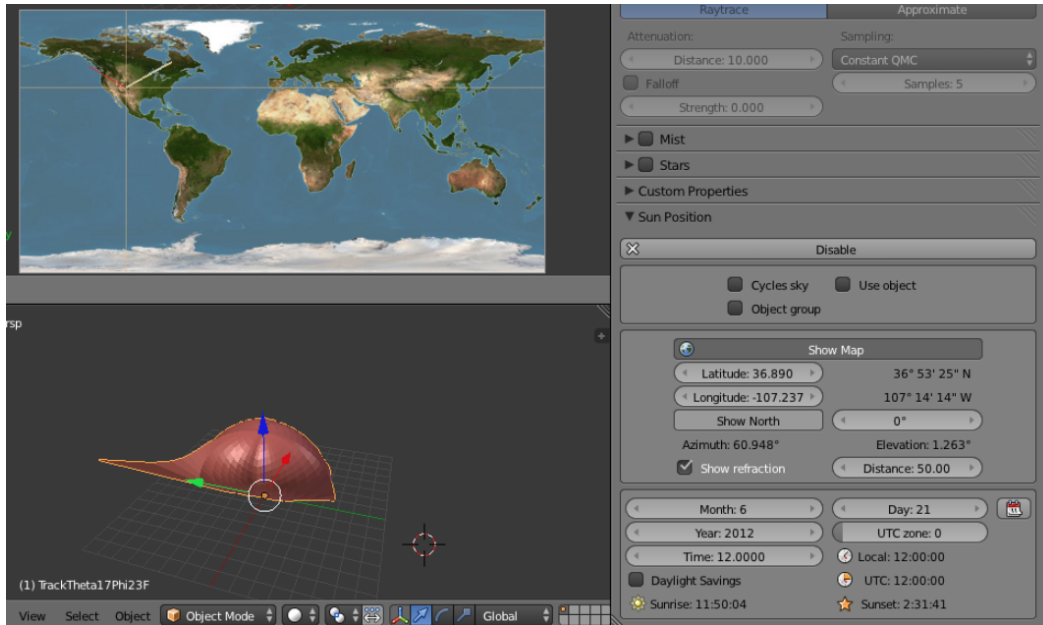


FIGURE 4.6: An example of hemispheric data plotted using the Blender 3-D software

### 4.3 Goniometric Modeling of Soil in the Visible Regime

If DIRSIG is to be used as a tool that is comparable to a goniometer, it should yield measurements that agree with field and laboratory studies. One way to validate such a tool is to recreate an experiment performed with actual goniometer hardware. Duplicating a collect requires the replication of the scene, sensor and experimental procedures.

If the results of the virtual experiment equal those produced using a physical scene and sensor, it indicates that the virtual detector configuration could be used for other virtual scenes and experiments. Work performed by Wang et al. (2010) can serve as a template for a virtual system. In that study, a goniometer mounted imaging spectrometer was used to determine BRDF.

#### 4.3.1 Scene Recreation

Two scenes were observed in the lab based study (Wang et al., 2010). One target consisted of flattened soil that was comprised of small grains. The second target included agglomerated clods of particles.

Section (4.1) described a method to create a virtual scene of particle grains using Blender 3-d modeling software. This process accounts for the physical geometry of the scene. Even so, particle size must still be determined. Soil particulates range in diameter from  $0.5\mu m$  to  $2mm$  (Simms et al., 2009). Particles of four different sizes ( $320\mu m$ ,  $640\mu m$ ,  $1.28mm$  and  $2mm$ ) were used for the virtual construction of the scene. These four evenly distributed geometries were multiplied many times to create a scene with greater than seven thousand particles. After running the Blender 3-D physics engine as discussed in Section (4.1), this scene was exported. Twenty five instances of the scene were tiled together to create the final soil scene that was used as a target for the DIRSIG goniometer.

#### 4.3.2 Goniometer Re-creation

To validate this study, the DIRSIG goniometer from Section (4.2) was built as a replica of a hardware system used by the University of Lethbridge in Alberta Canada (Wang et al., 2010). In their experiment, and in ours, a  $35mm$  focal length camera was used at a hemispherical measurement distance of  $1.78m$ . The imaging system was sensitive to wavelengths between  $400$  and  $700nm$  with a spectral resolution of  $0.5nm$ . Distinct spectral bands were represented as gaussian responsivity functions at  $0.45$ ,  $0.55$  and  $0.65nm$ . At an observation distance of  $1.78m$ , the Hamamatsu C8484-05G imaging spectrometer used by Wang et al. (2010) has an instantaneous field of view (IFOV) of  $0.88m$  in the x-axis and  $0.67m$  in the y-axis. Only 140 pixels in each spatial dimension from the center of the IFOV were used for BRDF analysis in that study. This was an effort to ensure that the same target sample was observed at every sensing position. The consequence of using  $140^2$  pixels for analysis is a reduced IFOV of  $0.092m$ . The 140 pixel configuration was mimicked in the virtual experiment. The light source in both

the physical experiment and the virtual experiment was placed at a zenith/declination angle of  $30^\circ$  from nadir. In the virtual experiment, light was modeled as a point source. This layout is a close approximation to the halogen light source used in the laboratory at the University of Lethbridge.

### 4.3.3 Experimental Procedures

The virtual hardware that was described in Section (4.2) was programmed to take measurements at view zenith angles between  $0^\circ$  and  $80^\circ$  and azimuth angles over the full  $360^\circ$ . Angular resolution of  $20^\circ$  was used for both the zenith and azimuthal dimensions. The measurement geometry used by the University of Lethbridge was limited by the physical size of the imaging system and only produced data from zenith view angles between  $0^\circ$  and  $60^\circ$ . Like in Wang et al. (2010), the target was illuminated by a static source that remained in the same  $30^\circ$  zenith position throughout the goniometric data acquisition.

After data was collected for every view location, average sensor reaching radiance (described in Subsection (4.2.4)) was used in conjunction with Equation (2.21) to find BRDF for each spectral band. This can be solved without using a calibration panel (as was done by Wang et al. (2010)) because the irradiance ( $E(\theta_i, \phi_i, \lambda)$ ) that is incident upon the virtual target is completely defined by the DIRSIG user. A more complete discussion of this process was presented in Section (4.2).

### 4.3.4 Goniometer Modifications

The particle soil scenes created for this research include hundreds of thousands of mesh objects that must be recorded in computer memory for use in DIRSIG simulations. A single instance of a particle model commonly exceeded 350 megabytes of storage. Scenes were typically constructed by tiling no less than twenty-five of these instances together to form large target areas of soil. Because so many objects are considered in a simulation, run times can be lengthy. Typical run times for the full goniometric data collection detailed in Subsection (4.3.3) would span two full days using DIRSIG 4.5 (A much improved version of DIRSIG now exists). It was concluded that the camera used in DIRSIG should be optimized.

A study was proposed to find the minimum number of pixels required to reproduce a desired soil signature in DIRSIG. Spectral BRDF curves produced in Subsection (4.3.3) were used as baseline signals. The 140 pixel camera configuration used in the previous

subsection was systematically reduced, and full goniometric measurements were performed and evaluated for each reduced number of camera pixels. This study would reveal the spatial resolution needed to perform measurements at a observation distance of  $1780mm$ . With less pixels, overall run time was reduced.

### 4.3.5 Complex Soil Scenes

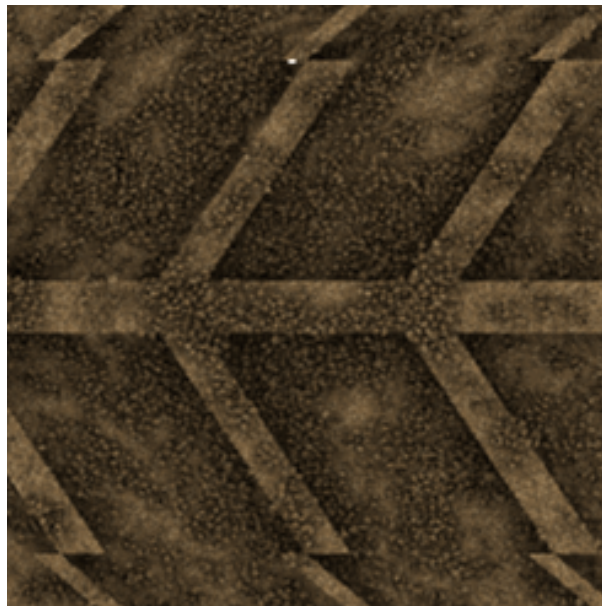
With virtual goniometer hardware in hand, more complex soil scene geometries can be explored. Scenes can be created that exhibit human interaction with soil. Weathered soil can also be modeled.

A tire track scene was constructed using the Blender 3-D graphic design software to analyze the BRDF of a scene with significant macro-features. Depicted as a DIRSIG image in Figure(4.7), the treads of the track are approximately  $8mm$  extrusions. The track was covered with particles of three different diameters ( $400\mu m$ ,  $630\mu m$ , and  $2mm$ ). Both the particles and the tire track itself were assigned the same soil material reflectance properties. This spectral curve was obtained from the USGS spectral library. Only one instance of the tire track was used in the final target scene that was fed into DIRSIG. This single instance was positioned at the center of the sensor field of view. Twenty-four instances of the soil scene described in Subsection (4.3.1) were tiled around the tire track feature. The virtual goniometer described in Subsection (4.3.2) was used to collect data at hemispherical view angles.

Changes in weathering and porosity alter the reflectance signature of soil (Lyon, 1964, Salisbury and Wald, 1992, Johnson et al., 1998b). A scene was built to include physical parameters of wind and electric charge to more physically model a weathered scene. Using this scene, an experiment was developed to study the change in signal due to particle size distribution. Altering the soil scene from Subsection (4.2.1) to include many smaller particles should create a noticeable change in porosity, and a different reflectance signature.

As stated previously, the initial soil scene contained evenly distributed particles in the  $320\mu m$  -  $2mm$  range. Grains interacted as rigid bodies and were subjected to gravity. The new target described above contained many smaller particles. Particles in the  $700\mu m$  -  $2mm$  range comprised 25% of the scene. Particles between  $160\mu m$  and  $700\mu m$  made up 75% of the particles in the scene. All particles were subjected to wind. This means that a directional vectorized force (in addition to gravity) was applied to the scene. Much of the soil was also assigned the physical parameter of electric charge. In-scene particles that are *charged* repel other *charged* particles and attract grains without

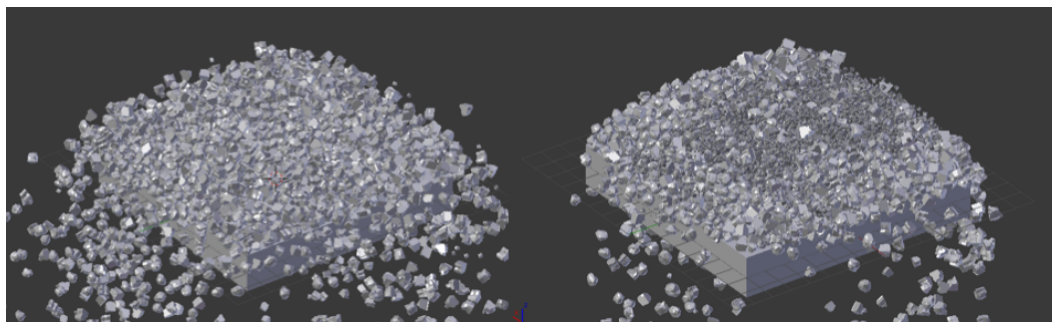





---

FIGURE 4.7: A tire track scene was built to observe the BRDF of soil subjected to human interaction

charge. With the addition of new forces and smaller particles, added complexity was added to the original soil scene. The original scene and the scene with additional small particles can be compared in Figure(4.8).




---

FIGURE 4.8: The original soil scene (left) exhibits an equal distribution of large and small particles. The target on the right is comprised of 25% large grains and 75% small grains.

The goniometric measurement described in Subsection(4.3.2) was used to measure the weathered scene. By using the same experimental protocol, BRDF results could be compared to those of the original soil scene.

## 4.4 Goniometric Modeling Using the NEFDS

The optical properties of targets used in conjunction with DIRSIG are obtained from databases of materials. The reflectance information from a database is applied individually to facets in a synthetic scene to produce radiometric ray-trace results that are consistent with each material being modeled. Directional hemispherical reflectance (DHR) signatures for many pure targets have been collected by Rochester Institute of Technology (RIT) and the United States Geological Survey (USGS) (<http://speclab.cr.usgs.gov>). Reflectance spectra for the sand particles created for this simulation were found in the USGS database. Each individual facet of a Blender 3D-generated object can be assigned with spectral properties from any of these libraries. A goal of this research is to characterize mixed materials. By mixing facetized objects that have been assigned specific optical characteristics, mixed material spectra can be created. These material descriptors require DHR data to describe diffuse materials (soils) and directional reflectance data to define specular materials (painted metals).

Another deep library that includes BRDF signatures of many materials is the Nonconventional Exploitation Factors Data System (NEFDS). The NEFDS provides a standardized database of reflectance information. To obtain this data, the National Geospatial-Intelligence Agency (NGA) has selected and examined twelve target categories containing more than 400 different materials and mixtures. Each material in the database has been measured goniometrically using precisely calibrated sensors and experimental procedures. Laser polarization measurements in the specular and backscatter direction provide data that can be used to tease out descriptions of specular, diffuse and volumetric scatter. Using the Beard-Maxwell (Maxwell et al., 1973) BRDF model paired with these measured data points, regression is performed to find the optimal reflectance coefficient for each view angle at every illumination position. Because there are a large number of free parameters in this BRDF, and these parameters correspond to physical material properties, NEFDS parameters tend to closely mimic experimental observations. The actual NEF product is a list of BRDF parameters for each specific measurement of each target in the database. NEFDS measurements are performed at multiple wavelengths, providing a measuring stick for wavelength dependent results produced using synthetic DIRSIG scenes.

For materials that are characterized by strong specular scattering, the directional reflectance measurements provided by the NEFDS are especially important. Since measurements by Kerekes et al. (2008) investigated the spectral signatures of soiled automobiles, a DIRSIG model was built to include a target of soil contaminated car paint.

Directional reflectance was not measured by Kerekes, therefore the surrogate reflectance properties of blue colored car paint were mined from the NEFDS.

#### 4.4.1 Soil Contaminant Study Using NEFDS Data

Soil often contaminates specular man-made targets. These targets will be misrepresented by a DIRSIG sensor if inappropriate material files are assigned to the objects being mixed. For targets with a specular quality, actual reflectance is large in certain view directions and smaller in others. In order to model the reflectance variability properly, DIRSIG requires directional reflectance information should be used to describe these targets.

The Non-conventional Exploitation Factors Data System (NEFDS) was detailed in Section (3.1). It is a standardized database of directional reflectance information. It contains data for many man made materials, including car paints.

The blue painted virtual surface used in this work was attributed with a full BRDF material file from the NEFDS. This means that when a DIRSIG sensor views the painted target from the specular direction it will detect a very high level of radiance. Likewise, a DIRSIG sensor situated at an azimuth angle that is perpendicular to the specular plane of the car paint will observe much less radiance because car paint is a very specular material. The soil particles used as contaminants in this study were assigned with a directional hemispherical reflectance (DHR) file from the USGS. Without the geometric complexity created in Blender 3-D, a plane assigned with the soil DHR would possess the same level of reflectance in both the specular and perpendicular viewing locations (Figure(4.9)).

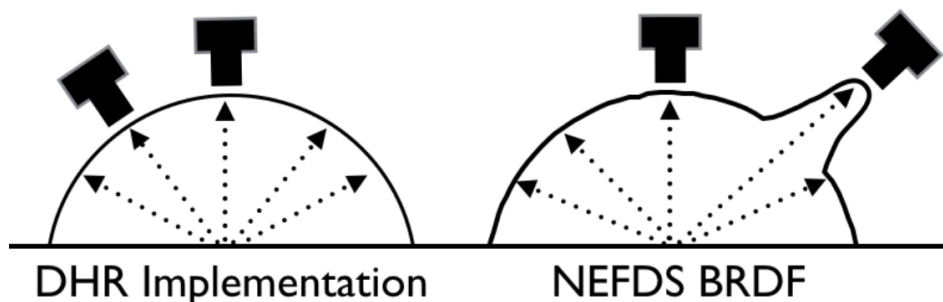
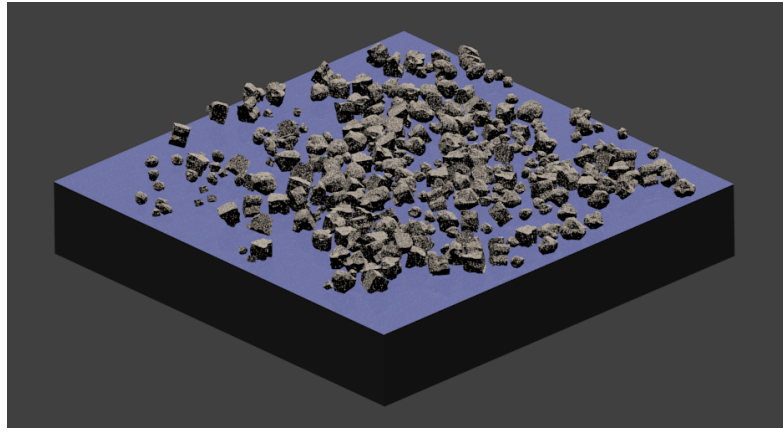


FIGURE 4.9: Uniform radiance is detected at all hemispherical view angles when DHR files are assigned to facets in DIRSIG. Preferential scattering can be observed when NEFDS data is used within a simulation

A study was formed to evaluate a mixed target of car paint and soil. Blender 3-D physics engine was used to create seven separate mixed target scenes. In each scene, a plane of blue car paint was covered with a different amount of soil contaminant. Seven different levels of contamination were simulated. The percentage of contaminant coverage was found using a Matlab script that was written to classify pixels as either car paint or soil. To do this, the radiance value of a pixel known to be uncontaminated car paint was used as a threshold value to separate clean and dirty pixels. Figure (4.10) shows a rendering of contaminated car paint that is similar to scenes used in this study.




---

FIGURE 4.10: Using Blender 3-D, a mixed target of blue car paint and soil was created

The bi-directional reflectance of each mixed target was calculated by DIRSIG within the solar plane ( $0^\circ$  or  $180^\circ$  from solar azimuth), and perpendicular to the solar plane ( $90^\circ$  or  $270^\circ$  from solar azimuth). The virtual hardware and illumination conditions described in Section (4.3) were used for this experiment. The spectral description of soil was derived from DHR files. Three separate spectral files were used to characterize the blue car paint. The first group of DIRSIG collections was performed using a DHR derived emissivity file for dirty blue car paint. As expected, Figure (4.11) shows that using a clean flat target attributed with this material file gives a Lambertian reflectance signature. The second group of observations used a DHR derived file for clean blue car paint. Although reflectance was lower for clean paint, using this emissivity file resulted the same Lambertian reflectance trend (Figure (4.11)) that was observed for the dirty paint. Full directional BRDF of washed blue car paint was extracted from the NEFDS and used for the third set of measurements.

After all of these tests, the position of the solar source was modified to evaluate the change in signal under new illumination conditions. Zenith angles of  $0^\circ$  and  $50^\circ$  were used for the additional data collections.

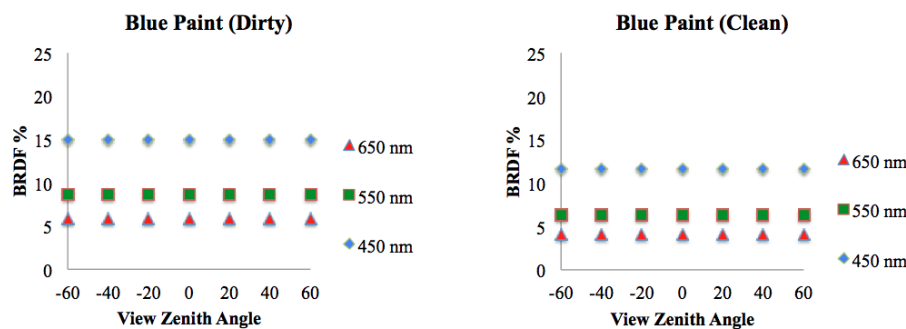


FIGURE 4.11: The chart on the left depicts DIRSIG generated bi-directional reflectance of a flat target assigned with a DHR based emissivity file of dirty blue car paint. Note that reflectance values do not vary with view angle indicating Lambertian behavior. The second chart (right) shows the same target scenario with a clean blue paint emissivity file. Reflectance values change between the dirty and clean paint, but both are Lambertian.

## 4.5 Soil Features in the Longwave Infrared

Subsection (3.2.4) discussed Longwave Infrared (LWIR) spectral features native to quartz based soil. These reflectance bands, called reststrahlen bands, between wavelengths of  $8\mu m$  -  $10\mu m$  are the byproduct of molecular vibrations. The shape and magnitude of these features are directly related to particle size. Weathering and human disturbance contribute to the distribution of different particle sizes within a sample. It was discussed that small fine particles cling to larger soil particles when the ground is dug up and overturned. The presence of the fine dusting, combined with altered porosity, distinctly changes the size and shape of sample signatures. A plan was developed to model the thermal spectrum of disturbed soil and to calculate the directional emissivity.

### 4.5.1 Geometry

This model of disturbed soil begins with a geometric description at the microscopic scale. As alluded to the previous discussions of Blender 3-D, mesh objects of different geometries are rotated, translated, and extruded to produce objects that match the 3-D geometry of soil grains. Scanning electron microscope (SEM) images provided a visual template for particle design. An example image can be seen in Figure (4.12).

In previous discussion, it was explained that weathering and human disturbance contribute to the distribution of different particle sizes within a target sample. It was observed that small fine particles cling to larger soil particles when the ground soil is

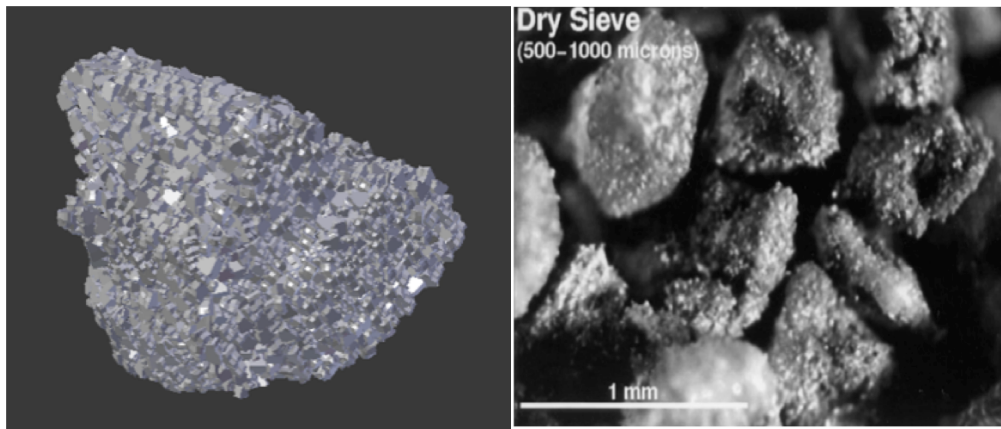


FIGURE 4.12: A soil particle covered dust grains (left) is one example of precise geometric modeling that is native to Blender 3-D. Scanning electron microscope images (right) reveal small dust particles clinging to larger grains (Johnson et al. 1998).

sifted or dug up and overturned (Johnson et al., 1998a, Salisbury and Wald, 1992). The presence of the fine dusting, combined with altered porosity, distinctly changes the magnitude and shape of sample spectral signatures. The scene built to model disturbed soil included superfine ( $50\mu m$ ) dust grains clinging to larger sand or soil particles. In Blender 3-D, a dusty sand particle was created through a simple process. First, a large grain particle ( $300\text{--}1000\mu m$ ) was designed. Then, a multitude of superfine particles were formed. Next, the facets of the large grains were subdivided into smaller faces that have a diameter that is close in size to the dusty fines. By aligning particle faces, each piece of dust was easily abutted to the larger particle. A parent-child relationship was set between the large grain and the fine particulates. This ensured that the large grain and the dust grains remained in contact during rigid body simulation. This also allowed for grains of each size to be assigned their own unique material spectra before the final geometry was exported to DIRSIG. A Blender 3-D representation of a dusty particle is depicted in Figure (4.12).

Realistic pose and mixture of scene constituents were created with the Blender 3-D physics engine. To model a natural soil scene, particles were not individually placed by hand. User placement of thousands of objects would be incredibly tedious and would likely produce an unphysical result. Each particle was treated as a rigid body and was dropped onto a surface where particle interactions occurred. Grains eventually settled into a physical 3-D soil scene. This process was performed for each particle size distribution and is illustrated in Figure (4.13).

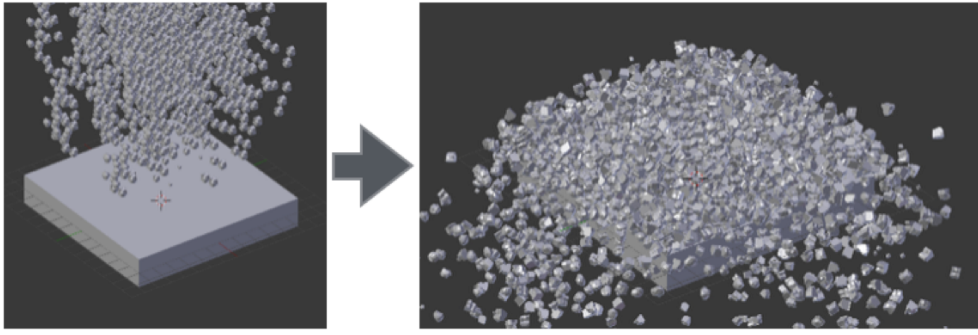


FIGURE 4.13: The process of scene building is based upon physics engines in Blender 3-D. Above, particles fall onto a surface where they settle naturally in space.

### 4.5.2 Hyperspectral Sensor

Before simulations were produced for the reststrahlen scene, it was important to develop a detector that could measure broadband LWIR signatures. The goniometer dimensions that were used in previous sections were also utilized for this sensor. The spectral response of the sensor was modified. Instead of using a three band sensor, 951 rectangular spectral bands were used. Spanning  $4.48\mu\text{m}$  -  $14.02\mu\text{m}$ , this sensor possesses  $10\text{nm}$  resolution. The spatial response matches that of Section (4.3.2) and Section (4.3.4).

### 4.5.3 Chemistry

Before analysis of emissivity can be performed, the spectral response of the scene should be validated with empirical emissivity measurements. Ideally, emissivity simulated over the range of the sensor should be similar, in size and shape, to that of disturbed soil observed in the field (Johnson et al., 1998b). It is known that large and small soil particles have distinct spectra (Salisbury and Wald, 1992) from the incoherent emission of radiation. Fortunately, LWIR emissivity spectra of soil for many size distributions (including  $50\mu\text{m}$  grains) has been published (Simms et al., 2009). This data can be extracted and converted to emissivity files. With the correct geometry and pure spectral characteristics in hand, the DIRSIG goniometer should be able to create a spectral signature that mirrors that of disturbed soil.

To tune the DIRSIG signature to match actual field measurements of disturbed soil, the reststrahlen scene can be systematically altered by gradually removing fine particles from the larger sand grains. A scene with large particles that are completely covered with small fines should produce a spectral emissivity curve that looks similar to a curve representing  $50\mu\text{m}$  particles. As the fines are removed, the material properties of the



larger particles should have a greater impact on the overall spectral signature of the mixed soil target. The desired scene geometry is the one that most closely represents disturbed soil.

#### 4.5.4 Radiometry

It should be reemphasized that the content of DIRSIG images is based on the amount of radiance that is detected by a virtual sensor. Radiance that is measured by a DIRSIG imager or a laboratory sensor has multiple components. Radiation leaves a target to be detected through processes of reflection ( $L_r$ ) and emission ( $L_e$ ). Radiance upwelling ( $L_u$ ) from the ground/target plane is a linear combination of these two processes and has been expressed in Equation (2.32).

In order to know target emissivity, the emissive and reflective components of Equation (2.32) must be separated. Empirical methods used to separate these terms are non-trivial. To calculate emissivity, downwelling radiance ( $L_d$ ) must be known or measured. Downwelling radiance is the radiation from the sky or a light source that illuminates a target. The equation used in DIRSIG and in the laboratory to find spectral emissivity is

$$\epsilon_{sample}(\lambda) = \frac{L_{target}(\lambda) - L_d(\lambda)}{L_{BB}(\lambda, T_{target}) - L_d(\lambda)}. \quad (4.5)$$

$L_{target}$  describes the radiance measured from a target by a DIRSIG sensor. Temperature dependent blackbody radiance ( $L_{BB}$ ) refers to radiance calculated according to the Planck equation. Note that the temperature used to calculate blackbody radiance must match that of the sample if correct emissivity is to be derived.

Obtaining emissivity using Equation (4.5) is a conditional process (Kerekes et al., 2013). When the temperature of the downwelling atmosphere is similar to that of the target, there is little contrast between values in the numerator of Equation (4.5). This results in small emissivity values that may be dominated by noise. Also, if the values in the denominator of Equation (4.5) have similar magnitudes, the emissivity equation becomes unstable. For these reasons, performing good emissivity measurements in the field or laboratory is hard to do. On very clear days, downwelling radiance ( $L_d$ ) is relatively stable and the sky is usually much colder than the sample of interest. In this scenario, Equation (4.5) provides good results. When conditions are imperfect, the sample temperature and the atmospheric temperature are knowingly altered in experimental situations in order to increase the contrast between radiance values. The accuracy of



the emissivity results also depends on how well the temperature of the sample is known. Temperature emissivity separation and curve smoothing techniques are often employed to find actual temperatures from a selection of probable temperatures.

Using DIRSIG to gather emissivity data does require some experimental manipulation, but the process is relatively easy and does not call for the post-processing described above. Users have control of in-scene radiance sources. By removing these sources, the downwelling terms of Equation(4.5) are nullified and a simple ratio remains.

$$\epsilon_{sample}(\lambda) = \frac{L_{target}(\lambda)}{L_{BB}(\lambda, T_{target})} \quad (4.6)$$

DIRSIG allows in-scene objects to be attributed with a specific temperature. This implies that the temperature of an object scene can be defined by the user, and blackbody radiance ( $L_{BB}$ ) is completely known. The user's control of radiation sources and temperature allows for emissivity to be solved painlessly.

With this theory in mind, the process to create emissivity simulations can be defined. First, import geometry into DIRSIG using .obj files. These files contain the locations of all the vertices and edges of objects in the target scene. Next, multiple instances of target geometry are defined within a .odb file. This allows for the size of a target to be expanded. Material (.mat) files are configured to link temperature and wavelength dependent spectral properties to facets in the scene. In this study, a temperature of 300K was used to define target radiance and blackbody radiance. To impose the conditions of Equation 3, irradiance from the in-scene light source is set to zero. This parameter is set within the atmosphere (.atm) file. Last, sensor geometry and response are defined. The sensor used in simulation must be configured within the platform file to be responsive in the desired wavelength range. Spectral resolution of 10 nm was used in this work.

Using the scenes and modeling techniques described above, the LWIR soil signatures in the reststrahlen bands can be modeled. Emissivity can be found for a sample of disturbed soil. DIRSIG provides user control of temperature and source radiance, which allows for reflection and emission to be evaluated separately. This process provides a method to simulate *in situ* soil signatures. Recreation of such scenes is difficult in a laboratory setting (Johnson et al., 1998b).

## 4.6 Modeling the Signatures of Particle Size Distributions

Soils subjected to different environments have different size distributions. The impact of particle size on soil target signatures was discussed in Chapter (3). With a virtual DIRSIG goniometer, spectral soil features related to unique distributions can be simulated.

Quartz based soil and sand particle size distributions have been measured at various locations world-wide (Bachmann et al., 2007, 2009, 2010). Both visible and LWIR spectra have been recorded for quartz soil of many different sieve sizes (Salisbury and Wald, 1992, Simms et al., 2009). Using the DIRSIG tools discussed in the previous sections of Chapter (4), soil reflectance signatures resulting from specific size distributions can be modeled. Scenes containing different sizes of particles should have unique porosity and volumetric scattering properties.

### 4.6.1 Geometry

In this work, the parameter of particle size distribution is defined using sand that was collected from the Virginia Coast Reserve Long-Term Ecological Research site (VCR-LTER) (Bachmann et al., 2007, 2009, 2010). The distributions used in this experiment are shown as histograms in Figure (4.14). Each distribution was collected at a different transect of the same site on North Smith Island, Virginia. Soil samples were sieved to separate particles and weighed to determine the percentage of each particle size within the sample. Three different distributions were used for this model. As seen in Figure (4.14), distribution (a) was nearly uniform. Particles within this distribution ranged in diameter from  $10\mu m$ - $600\mu m$ . Distribution (b) was a bimodal distribution. Particles from this sample ranged in diameter from  $100\mu m$ - $600\mu m$ . Greater than 70% of the particle in the scene were either  $150\mu m$  or  $600\mu m$  in diameter. Samples from the Bachmann measurements most closely mimicked distribution (b). Distribution (c) was practically unimodal with greater than 70% of the particles having a diameter of approximately  $150\mu m$ .

Each particle distribution in Figure (4.14) was treated as a multitude of rigid bodies that were dropped onto a surface where particle interactions occurred. Grains eventually settled into a physical 3-D soil scene.

The density of the scene was altered by the addition of more particles. The change in density was calculated using a volumetric bounding box within the Blender 3-D software. After the rigid body physics engine was applied, the number of particles within

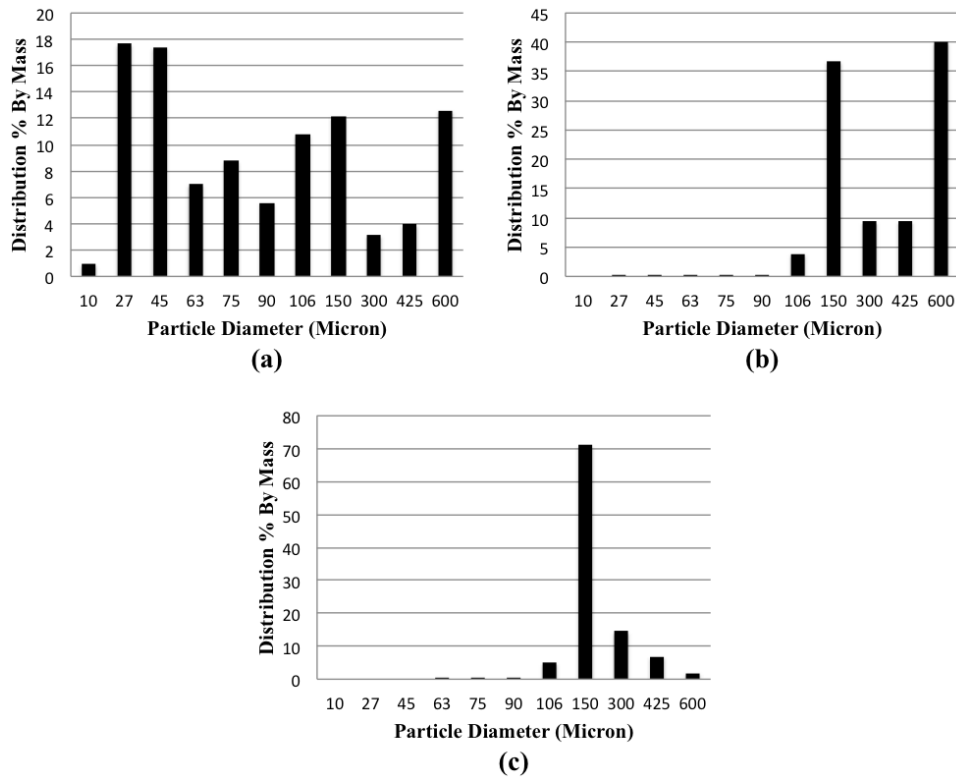


FIGURE 4.14: Scenes used within the DIRSIG simulations were fashioned using three particle size distributions. Distribution (a) was more uniform with respect to particle diameter. Distribution (b) was bimodal with the majority of particles possessing diameters between  $150\mu m$ - $600\mu m$ . More than 70% of particles in the unimodal Distribution (c) had a diameter of  $150\mu m$ .

a bounded volume was calculated. Figure (4.15) shows the geometric representation of two particle scenes that have the same size distribution (Distribution (b)), but differ in grain density by 29%.

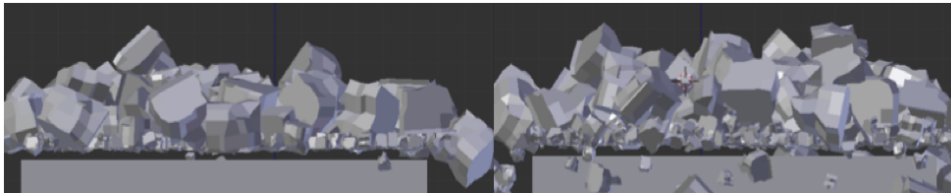


FIGURE 4.15: The scene on the right was 29% more dense than the scene on the left. Pores in the high-density scene are more completely filled than those corresponding to the low-density target.

### 4.6.2 Chemistry

Before each geometric scene was inserted into a DIRSIG radiometric simulation, spectra were assigned to the facets of each particle. Spectral reflectance and emissivity response curves represent how each facet will respond to interaction with a photon. Absolute reflectance of pure quartz was assigned to each particle in both the high-density, and low-density configurations for the distributions shown in Figure (4.14) (a) through (c). A total of 6 quartz scenes were considered. Both a high and low-density scenes were developed for each of the three particle size distributions.

To investigate the impact that soil density has upon the spectral signature of a mixed soil sample, reflectance properties of both magnetite and quartz were included in a single scene. A high-density scene and a low-density scene of mixed soil were created. The trends observed by Bachmann et al. (2014) were thought to be a byproduct of smaller magnetite grains physically mixed with larger quartz grains. Therefore, the distribution shown in Figure (4.14b) was used for each of the two mixed scenes. As is seen in Figure (4.16), the smallest particles ( $106\mu\text{m}$  and  $150\mu\text{m}$ ) were given the spectral signature of magnetite. All particles larger than  $150\mu\text{m}$  were attributed with the absolute reflectance of pure quartz.

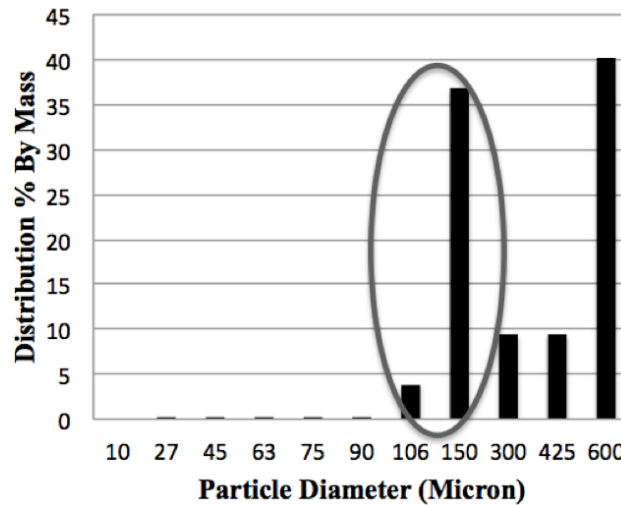


FIGURE 4.16: Distribution (b) from Figure (4.14) was used to describe a mixture of quartz and magnetite. Particles with  $106\mu\text{m}$  and  $150\mu\text{m}$  were attributed with the spectral properties of magnetite. Larger particles were represented as quartz in the DIRSIG simulations.

### 4.6.3 Radiometry

In Equation (2.39),  $L_p$  describes the radiance reaching the sensor produced by a DIRSIG simulation or a physical imaging system. With radiance in hand, solving for BRDF should be straight forward. However, sensors do not exhibit perfect sensitivity at all wavelengths. This was explained theoretically in Section 4.2.4. Every simulation photon that hits a detector does not necessarily result in a signal electron. Therefore, solving for BRDF requires compensation for device sensitivity. Detectors typically have spectral response functions that describe how efficiently photons are converted to signal over a range of wavelengths. The virtual sensor used in this experiment was characterized by Gaussian shaped response functions centered at  $450nm$ ,  $550nm$ ,  $650nm$ ,  $868nm$ ,  $1000nm$ , and  $1915nm$ . Bachmann et al. (2014) also analyzed spectral reflectance at these wavelengths at a shorter observation distance. Half nanometer spectral resolution was used. The virtual sensor was positioned 1.78m from the virtual soil surface. A reduced instantaneous field of view (IFOV) of 0.092m was evaluated in an attempt to maintain a constant view of the scene as the sensor zenith angle was increased. This sensor configuration matches that of the University of Lethbridge goniometer system version 2.5 (ULGS-2.5) (Wang et al., 2010). Prior to simulation, the total scene irradiance,  $E$ , is specified by the user. The solar illumination source was initially positioned with a zenith angle of  $30^\circ$  from nadir. Scenes with a solar zenith angle of  $20^\circ$  were also subjected to simulation. DIRSIG will not allow for remotely sensed signal to exceed that of the illumination source.

Using the scenes and modeling techniques described above, the BRDF of pure quartz and mixed soils can be modeled. BRDF was calculated for samples of quartz, having different particle size distributions and density. Additional BRDF models were simulated for samples of mixed quartz and magnetite. Within each scene, rays are traced from the illumination source, to the soil sample, and then on to the sensor. Light often interacts with multiple grain boundaries as it travels. At times these grains are different materials that possess unique chemical and optical properties. The result is a reflectance signature that represents the intimate mixing of chemical properties within the sensor IFOV.

## 4.7 Directional Reflectance and Emissivity of Lab Targets

The plethora of recorded field and lab data has given credence to the simulations created in the previously described studies. Without the spectral curves documented in publications and lookup tables, scene-sensor experiments linked to soil targets could not

be validated. To test more complex models and simulations against the physical world, data should be collected first hand.

#### 4.7.1 Directional Emissivity Measurements

Longwave Infrared (LWIR) measurements were obtained for a quartz based sand target, and a target of similar sand that had been contaminated with calcium chloride. The intent of the collection was to observe changes in spectral contrast as the sensor view angle varied from nadir to grazing. The sample itself included sand that was calibrated for size and spectra. Equation (4.5) was used to solve for emissivity at each sensor location. The spectrometer chosen for the experiment was the D&P Instruments Model 102F microFTIR. System specifications for this device are shown in Table(4.1)

Parameter	D&P Instruments Model 102F microFTIR
Spectral range	2.0 to 16.0 $\mu m$
Spectral resolution (FWHM)	$4cm^{-1}$ at $2\mu m$ , 1 sec/scan
Spectral sampling	$4 cm^{-1}$

TABLE 4.1: Spectrometer specifications for directional emissivity measurements

As discussed in 4.5.3, Equation (4.5) becomes unreliable if there is not adequate thermal contrast between the target and the sky surrounding the sample. To provide the necessary contrast, a medical heat pad was placed beneath each soil sample. The difference in temperature between the heated soil and the cold sky provided adequate separation to maintain stability in Equation (4.5). Evidence is displayed in Figure (4.17).

Calcium chloride was applied to one of the two soil targets with a concentration of 38%. The contaminant was dispensed uniformly at a rate of  $0.27 gal/yd^2$ . This is the rate recommended by the Occidental Chemical Corporation for use on unpaved roads. The contaminated target is shown in Figure (4.18).

Data was collected with  $10^\circ$  angular resolution in the zenith dimension. Eight measurements were made between nadir viewing and  $70^\circ$  zenith. At each viewing position, downwelling radiance was measured using a calibrated Infragold panel ( $\epsilon = 0.04$ ). The temperature of both the soil target and the Infragold panel were measured using an Exergen IR thermometer. Soil targets ranged between  $33$  and  $39^\circ C$ . The Infragold panel maintained temperatures between  $21$  and  $23^\circ C$ . Emissivity was determined by using the Christiansen transmission feature of quartz ( $\lambda = 7.4\mu m$ ) as a benchmark. At this wavelength, the index of refraction of quartz approaches that of air. The result is a narrow band of near perfect emission ( $\epsilon = 0.98$ ).

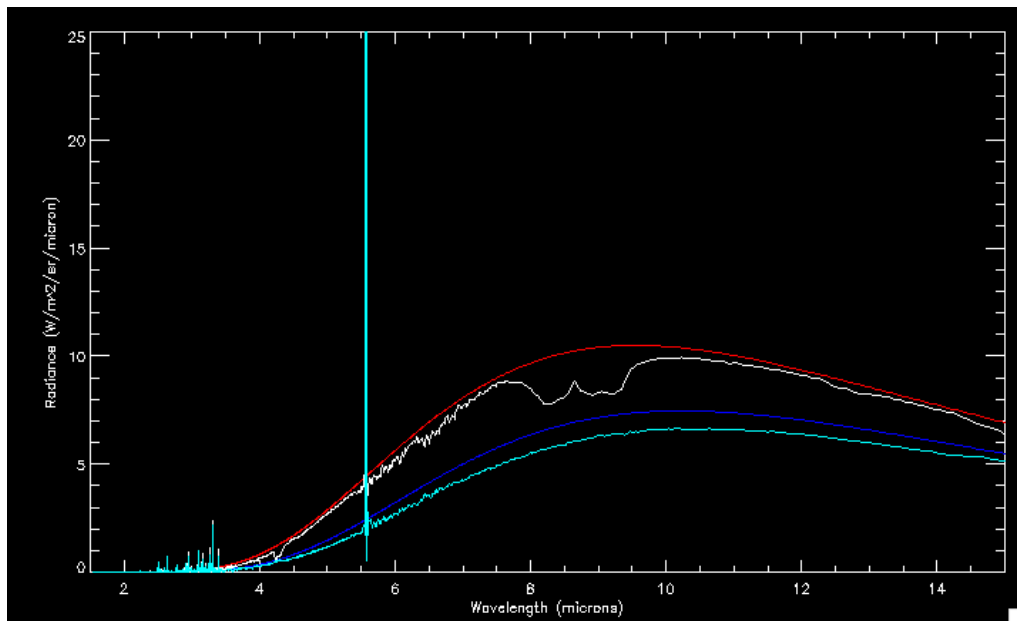
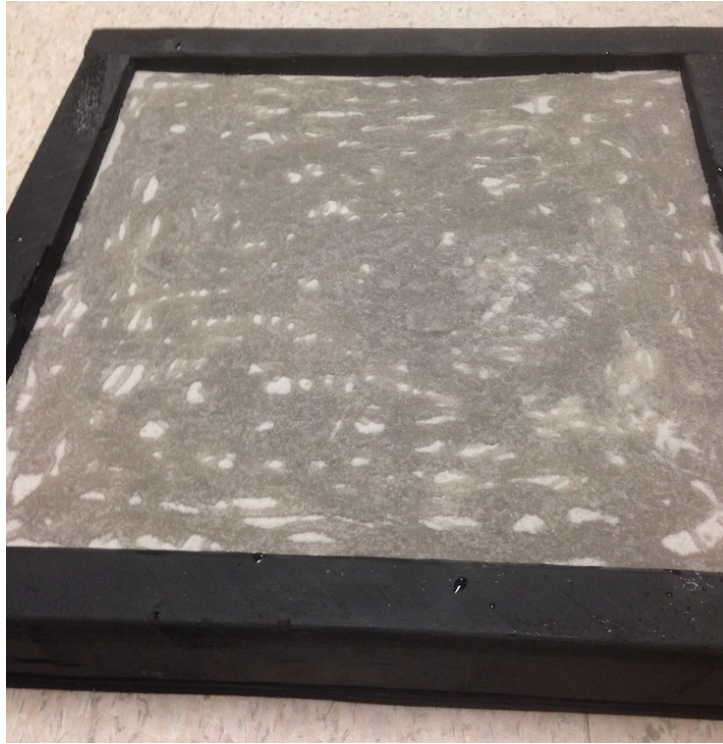


FIGURE 4.17: Soil radiance (white curve), background downwelling radiance (cyan curve), warm blackbody radiance (red curve), and cool blackbody radiance (blue curve) are plotted together using the D&P 102F FTIR. Separation between the target and downwelling radiance curves was generated through the use of a heating pad strategically placed below the surface of the measured soil targets. This separation provides stability for the calculation of thermal emissivity.

#### 4.7.2 BRDF of Soil with Calcium Chloride Solution

In Chapter 1, the example of a dirt road was given to illustrate the need for the BRDF analysis of soils. Studying mixed soil road targets is interesting because roads are subjected to both human contact and the weather. An investigation into spectral signature manipulation due to tire track features was described in 4.3.5. Rain and wind impact the fine dust coatings that contribute to spectral signatures in the LWIR. Within this research project these disturbed soil effects were discussed and simulated using DIRSIG.

To resist the effects of wind and improve the longevity of soil roadways, chemical treatments are often sprayed superficially upon road surfaces. The most common chemicals used for this task include sodium chloride and calcium chloride (Kocielek, 2013). Figure (3.3) shows electron microscope imagery and X-ray microanalysis data for soil treated with calcium chloride. When treatments are applied to soil, particles agglomerate. Particles held together by chemical mixtures give the geometric appearance of larger particles. X-ray microanalysis indicates that calcium and chlorine may dominate the spectral signatures of particle facets. It is obvious that both the geometry and spectral description




---

FIGURE 4.18: Calibrated sand with 38% calcium chloride solution

of a dirt road target will be altered by chemical mixing.

An effort to measure and simulate the RGB reflectance spectrum of chemically contaminated soil is proposed. Methodology has been developed for both the experimental and modeling arms of this study.

#### 4.7.2.1 BRDF of Collection with GRIT

The chemical mixture described above has not been characterized in accessible databases. Goniometric data was collected in order for simulations of this sample to be validated. This measurement was performed using the goniometer of the Rochester Institute of Technology (GRIT). GRIT (Figure (4.11)) is a half meter hemispherical goniometer equipped with a high resolution spectroradiometer (Peck et al., 2015). For a half meter observation distance viewed at nadir, a  $5^\circ$  field of view (FOV) fore optic produces a  $4.37\text{cm}$  diameter IFOV on the sample. Spectral range, resolution and sampling of the spectroradiometer are denoted in Table (4.2).



Parameter	FieldSpec 4 Hi-Res Spectroradiometer
Spectral range	350-2500 nm
Spectral resolution (FWHM)	3 nm @ 700 nm 8 nm @ 1400/2100 nm
Sampling interval	1.4 nm @ 350-1050 nm 2 nm @ 1000-2500 nm
Scanning time	100 ms

TABLE 4.2: Specifications for the high resolution spectroradiometer that is used in conjunction with GRIT.

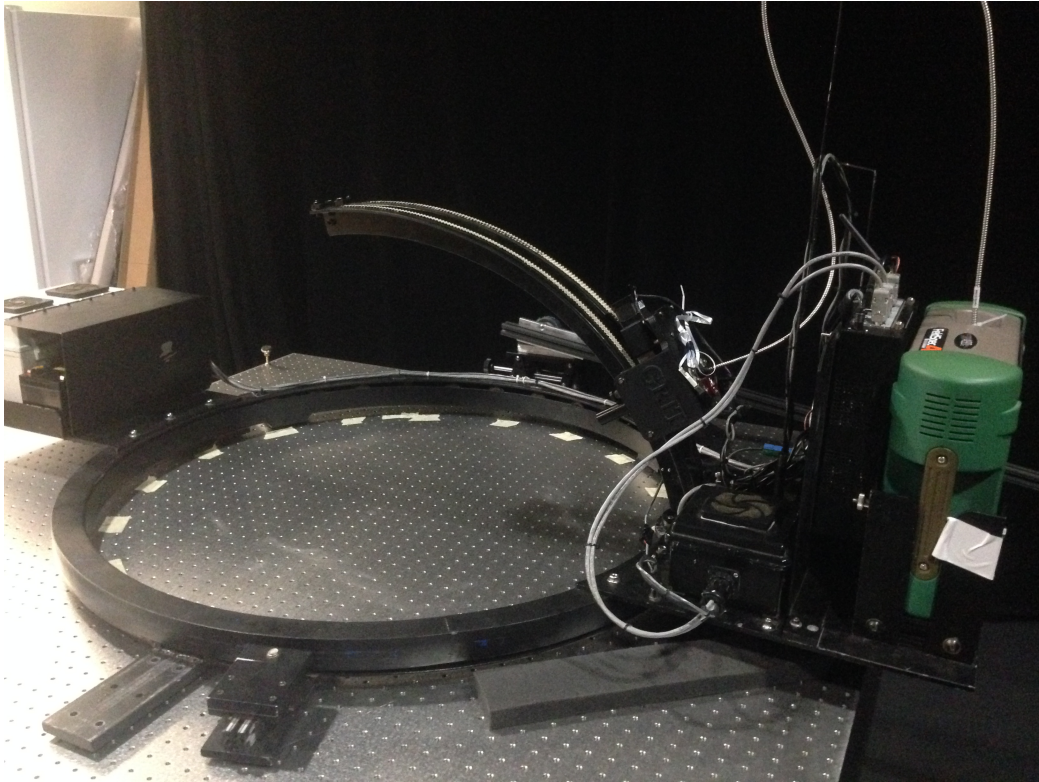


FIGURE 4.19: The goniometer of the Rochester Institute of Technology (GRIT)

Directional reflectance measurements were made in both the principal and perpendicular viewing planes for targets of calibrated sand, sand with CaCl contaminant, pure CaCl in powdered form, and oven-baked CaCl solution. Hyperspectral reflectance curves of these targets were fed into DIRSIG for use in the simulation and validation of contamination models

#### 4.7.2.2 BRDF Simulation

After SEM images were taken and data was collected using the GRIT system, scenes were created in Blender 3-D. A DIRSIG grayscale rendering of a soil scene with  $300\mu m$ - $600\mu m$  grains is displayed in Figure (4.20). Spectral reflectance of sand or calcium chloride was assigned to individual facets of each particle in the scene. Simulations were then performed using the virtual DIRSIG hardware referenced throughout Chapter 4. The DIRSIG imaging platform was constructed to replicate the specifications of the GRIT system. This included a half-meter arc radius and a  $5^\circ$  fore optic. Simulated BRDF was calculated using the procedures of Section (4.2).



FIGURE 4.20: A rendering of a soil scene created in Blender 3-D. Individual particles range in diameter from  $300\mu m$ - $600\mu m$ . This geometry serves as the scene input of a DIRSIG simulation

## Chapter 5

# Results

### 5.1 Goniometer Recreation and Soil Study

Recall from Section 4.3 that a primary goal of this research was to create virtual measurement hardware with outputs that can be compared to empirical laboratory and field measurements.

A goniometric collection of soil reflectance data gathered at the University of Lethbridge by Wang et al. (2010) was modeled in DIRSIG. The light source in this study was placed at a  $30^\circ$  declination angle and measurements were taken with an angular resolution of  $20^\circ$  in the zenith dimension. Empirical BRDF results from Wang et al. (2010) yielded several notable reflectance features in the principal solar plane and in the perpendicular plane. Sensor positions that share the same azimuthal plane with the sun or light source are said to be *in plane* or in the *principal plane*. Sensor locations that have azimuthal angles  $90^\circ$  from solar/source azimuth are said to be in the *perpendicular plane*. A visual representation of these view geometries is presented in Figure (5.1).

The soil simulation results (Figure (5.2)) show strong opposition effect backscatter in the principal plane with maximum reflectance values for red, green, and blue bands occurring at a zenith angle of  $40^\circ$  from nadir. All measurements taken at backscatter view angles had higher reflectance than data collected at forward scattering angles. This trend can be attributed to the shadow hiding opposition effect (SHOE) (Hapke, 2012a). A picture of this effect in the principal plane is shown in Figure (5.1). The lack of a reflectance peak in the forward scattering plane indicates that geometric features of the target shadow and occlude one another. Data taken at larger declination angles is strongly influenced by this effect. In the perpendicular plane (Figure (5.3)), peak reflectance occurred at nadir where the least amount of shadowing and occlusion occurs.

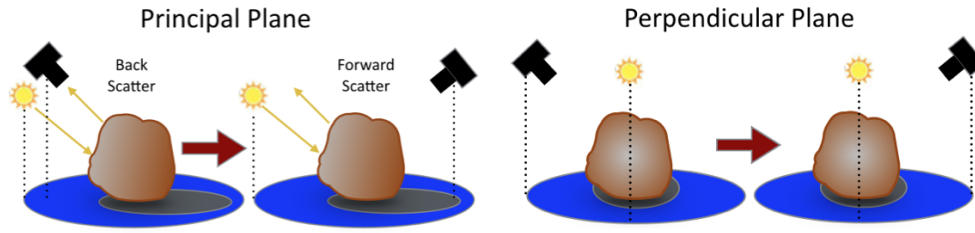


FIGURE 5.1: Principal plane (left) measurements are made when a light source and a sensor have the same azimuth angle, or when the source and sensor have azimuth angles that are  $180^\circ$  apart. In the perpendicular plane (right), the least amount of shadowing and occlusion is observed when the sensor is directly above the target. Because the light source is located in a plane that is perpendicular to the sensor, the reflectance decreases uniformly as the sensor zenith angle is increased from the nadir position. Darkness dominates the shadowed regions of a target resulting in fewer reflected rays traveling between the target and the sensor. Reduced spectral contrast is a byproduct of these shadows. Unique reflectance features also arise from the intimate mixing of grains, scattering albedo, grain transmittance, and sample density.

This is also illustrated in Figure (5.1). Reflectance decreased uniformly as the view zenith angle increased in both the positive and negative direction. Simulated BRDF in the red, green and blue bands all vary from the measured lab data by an average of less than 6% of BRDF percentage, with standard deviations between 4% and 5%. There was 8% error of BRDF percentage in the blue band perpendicular plane measurements. All other measurements matched the measured data within a 6% error. The spectral contrast in both planes also says something about the geometry of the soil scene.

In both the principal and perpendicular planes Figures(5.2-3), the red channel reflects more than the green band, which exhibits higher reflectance than the blue band. This aligns with human perception of soil. Dirt appears more red to humans than it does green or blue. Each band displays a similar BRDF shape in the principal and perpendicular planes. This reflectance description was also observed in the empirical data.

The sensor geometry of forward and backscatter in the principal plane is defined in Figure (5.1). Unlike physical measurements, DIRSIG simulation of principal plane BRDF will not include the shadowing effects caused by the detector itself. Particle self-shadowing is the only shadowing mode included in the simulation. The most particle self-shadowing occurs in the forward scattering direction of the principal plane at large sensor declination angles. At these sensor locations, Figure (5.2) shows that the spectral contrast between red, green, and blue bands is the smallest. This indicates that within shadows, there is little reflectance and that the true spectral nature of a sample will be masked. It is also observed that in the backscatter direction of the principal plane, spectral contrast is the highest. In the perpendicular plane (Figure (5.3)), spectral contrast remains



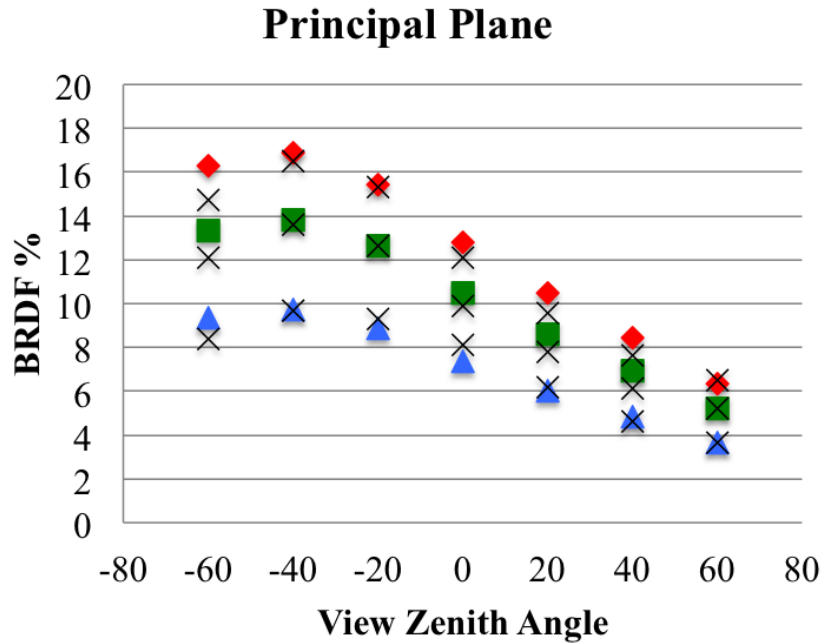


FIGURE 5.2: DIRSIG simulated principal plane BRDF data for a soil scene replica of the experiment performed by Wang et al. (2010). Data collected by Wang et al. (2010) is displayed in black. Red, Green and Blue curves correspond to 450, 550, and 650nm respectively. Note the presence of a backscatter peak near the location of the illumination source ( $-30^\circ$  zenith).

relatively constant across all view zenith angles indicating that shadowing changes very little. When it does change, BRDF decreases in uniform fashion as the sensor zenith angle increases. This is expected for sensor positions in the perpendicular plane because the sensor does not detect the majority of forward and backscattered light. These trends are clearly visible in both the empirical and simulated results.

It was shown that DIRSIG based virtual hardware can be used to accurately measure the BRDF of a soil scene. However, each data point in Figures (5.2-3) required greater than 120 minutes of DIRSIG run time. A study was performed to explore whether the reflectance features described above could still be observed if fewer pixels were used to make the measurement. Using fewer pixels requires minimized ray tracing within DIRSIG, and saves simulation time. Results of this experiment can be seen in Figure (5.4). Sensors with  $20^2$ ,  $35^2$ ,  $70^2$  and  $140^2$  pixels were used in the principal plane to perform the comparison. Although there was some variance in the data. There was essentially no change in radiance or curve shape when fewer pixels were utilized. The dominant curve features were observed in all cases.

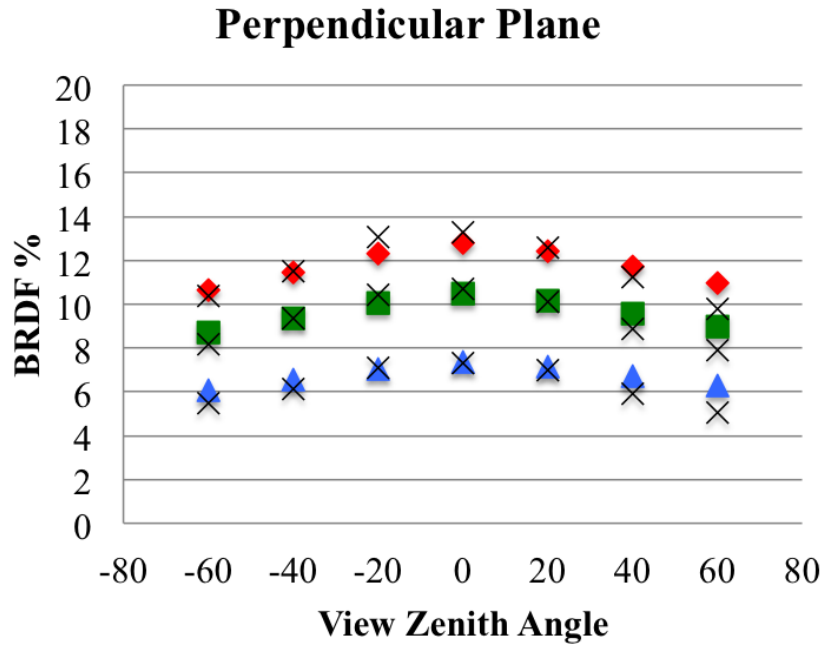


FIGURE 5.3: DIRSIG simulated perpendicular plane BRDF data for a soil scene replica of the experiment performed by Wang et al. (2010). Data collected by Wang et al. (2010) is displayed in black. Red, Green and Blue curves correspond to 450, 550, and 650nm respectively.

To validate the assumptions of geometric shadowing made above, and to understand how signatures might change with illumination, the illumination conditions were modified in DIRSIG. Figures (5.2-3) were obtained using a point source representation of the sun. It was determined that a different lighting scenario should be explored. In this test, the geometric soil scene used to generate Figures (5.2-3) was recycled. A portion (80%) of the source irradiance was distributed uniformly about the hemisphere above the sample. The remaining 20% of the irradiance originated from the location of the solar point source. This means that light rays were impinging upon the sample from all hemispherical directions. A reduction in shadowing, and a corresponding reduction in the SHOE effect was observed. DIRSIG results displayed in Figures (5.5-6) highlight this reduction. In the solar principal plane, the back scatter hot spot was muted. There remains some indications of geometry because data points collected in the back scatter direction still have higher radiance values than those generated in the forward scattering direction. Also, radiance data observed near grazing angles exhibits far less change because of illumination originating from the hemisphere above the target. This effect is most noticeable in the perpendicular plane. The radiance curve begins to fall off at large

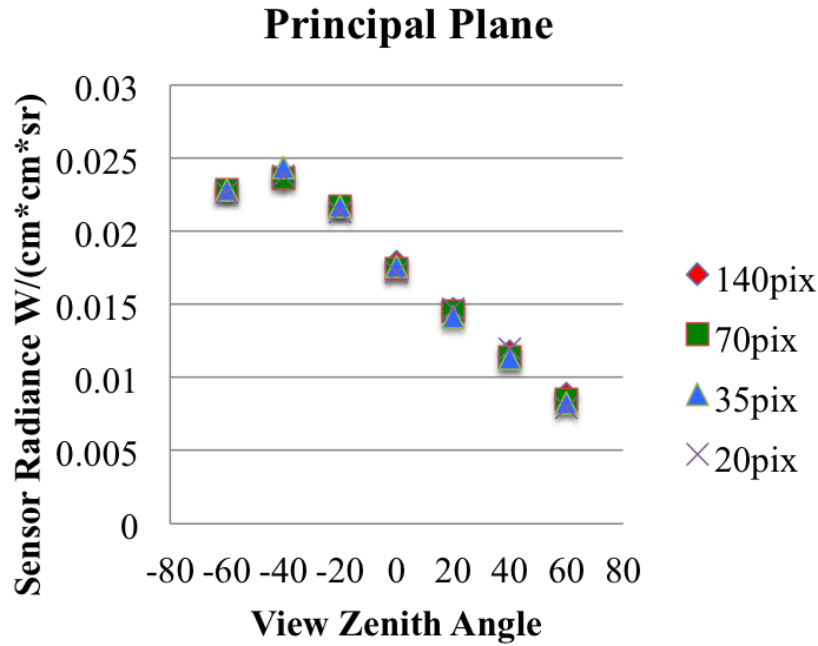


FIGURE 5.4: DIRSIG soil simulation of the same scene with varying resolution

declination angles before increasing at the largest zenith angles due to contributions from hemispherical illumination. In both planes, it is evident that illumination geometry has a noticeable impact on reflectance and sensor reaching radiance.

## 5.2 Complex Soil Scenes

### 5.2.1 Tire Track Scene

After establishing that surface reflectance could be accurately simulated for soil particle features, a tire track imprint was designed in Blender 3-D to study larger scene geometries (Figure (4.7)). It was shown in the previous section that particle sized extrusions create shadowing effects, and impact BRDF. It was expected that feature shadowing would be amplified within simulations that included larger macro-features. Figure (5.7) shows a DIRSIG generated image of the tire track scene with the illumination source at zenith angles of  $30^\circ$  (left) and  $75^\circ$  (right). Shadowing is apparent, and it is expected that BRDF should have a smaller magnitude when the light source is positioned lower in the sky.

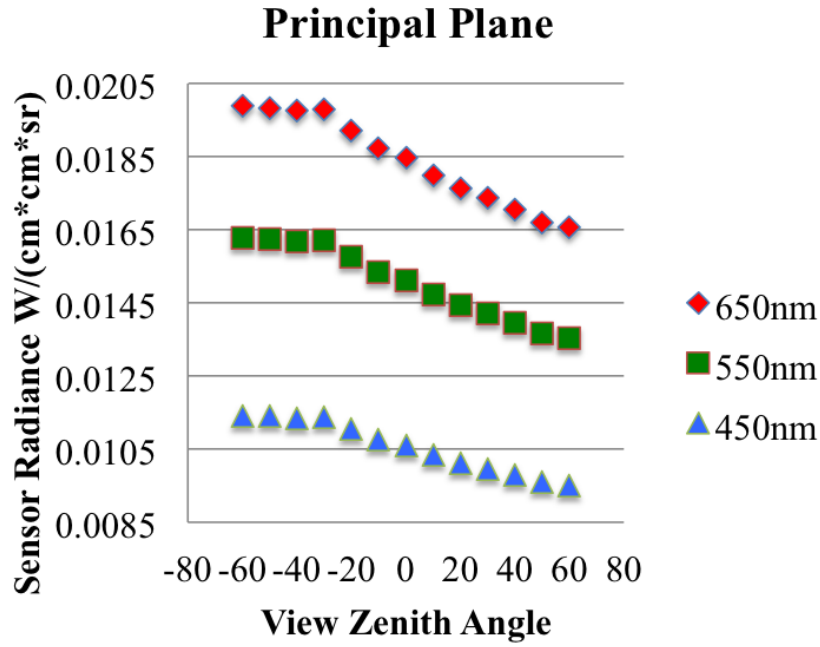


FIGURE 5.5: In plane DIRSIG generated soil radiance with 80% of the illumination uniformly distributed over the hemisphere above the sample

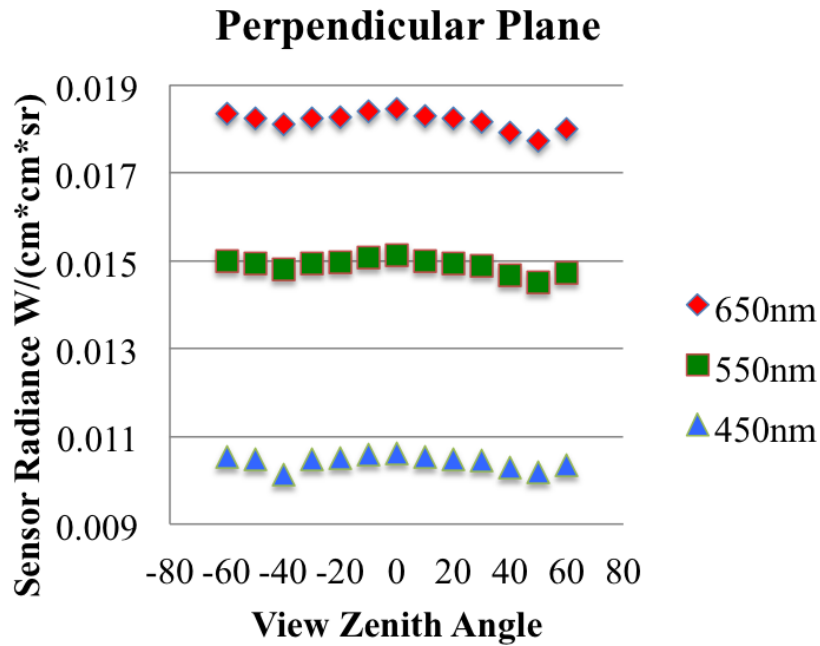
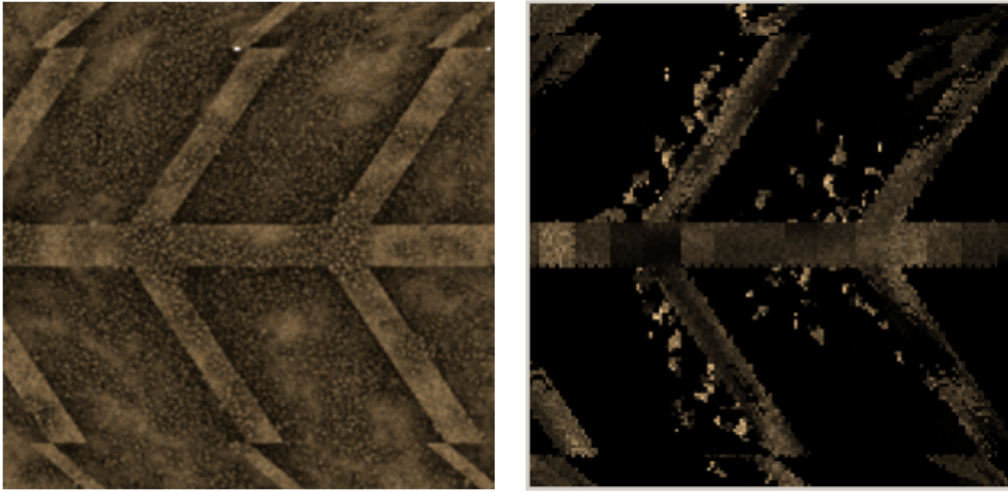


FIGURE 5.6: Perpendicular plane DIRSIG generated soil radiance with 80% of the illumination uniformly distributed over the hemisphere above the sample






---

FIGURE 5.7: DIRSIG renderings of a tire track scene. The light source azimuth is the same in both images. The source location of the image on the left is at a zenith angle of  $30^\circ$  and the source of the image on the right has a zenith of  $75^\circ$

Using the virtual goniometer, BRDF was collected for illumination source positions corresponding to  $0^\circ$ ,  $45^\circ$ , and  $90^\circ$  azimuth angles. Like in section 4.2.5, Blender 3-D was used to display three dimensional plots of BRDF. To provide orientation, a small yellow orb was also plotted at the position of the illumination source. Figures (5.8-10) show the change in BRDF based on light source position. In each of the three images, the source azimuth was set to  $0^\circ$ . Zenith angles were preset to  $30^\circ$  (Figure (5.8)),  $55^\circ$  (Figure (5.9)), and  $75^\circ$  (Figure (5.10)). Data points are plotted hemispherically by sensor viewing position. Points plotted at greater distances from the vertex of the hemisphere indicate large reflectance magnitude compared to data points plotted closer to the center of the hemisphere. By observing the plots, it is obvious that the presence of the  $8mm$  tire track macro-features produces a non-Lambertian BRDF. Note that the BRDF magnitude of most of the view angles decreases as the source gets lower in the sky. This is because shadowing is increasing at most view angles. Also notice that increasing the source declination angle causes primary backward and forward scattering to occur at larger sensor declination angles. This is an expected result. Lastly, note that the BRDF plot looks less like a diffuse reflectance function as the source gets lower in the sky. This effect was also observed by Peck et al. (2015). In fact, BRDF magnitude at large sensor zenith angles increases as the source zenith angle increases. Figure (5.10) shows that when the source is at a  $75^\circ$  declination, the magnitude of reflectance remains high for large sensor zenith angles, but is almost zero for most other sensor positions. This indicates two things. First, tire track features disallow light from being reflected

to near nadir sensing positions. Also, the plot confirms the physical assumption that rough surface reflectance becomes more directional and less diffuse as the illumination source approaches surface grazing angles.

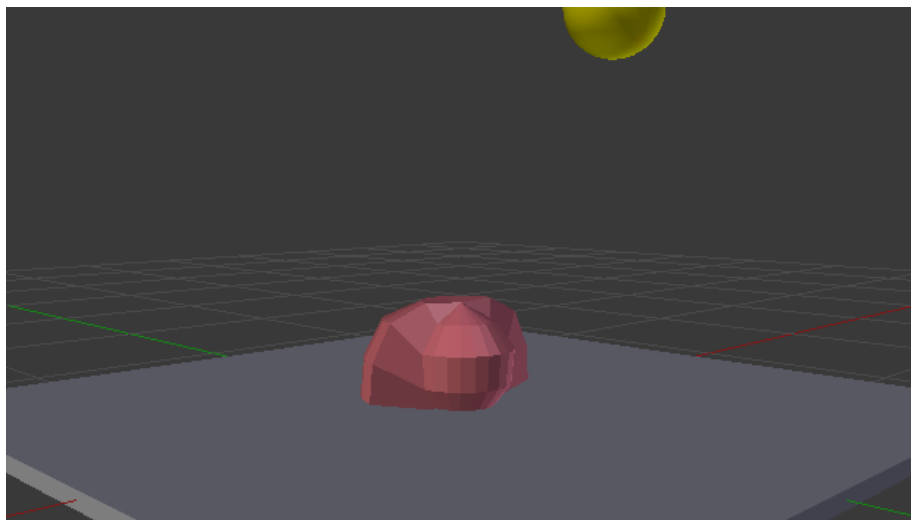


FIGURE 5.8: DIRSIG rendered BRDF of the tire track scene. BRDF is displayed in three dimensions using Blender 3-D. The light source is positioned at a zenith angle of  $30^\circ$

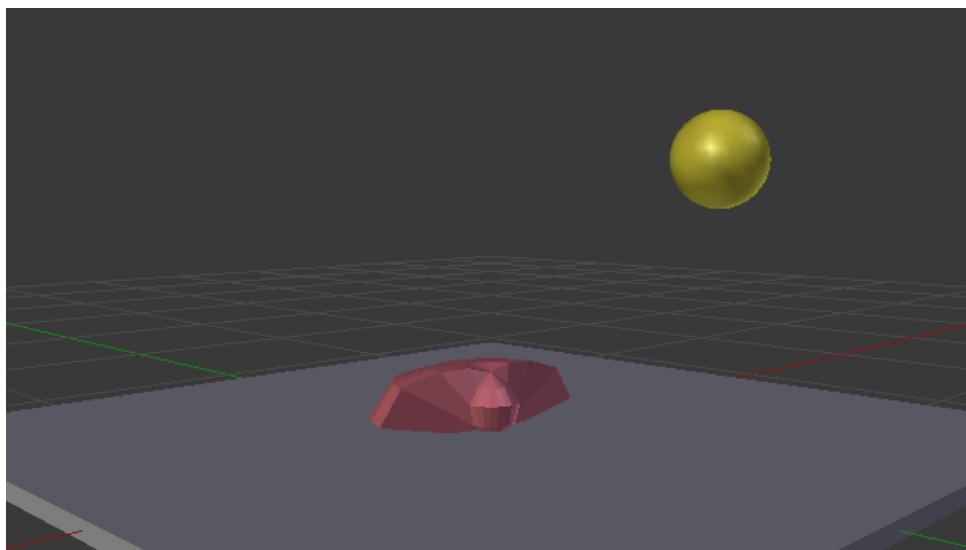


FIGURE 5.9: DIRSIG rendered BRDF of the tire track scene. BRDF is displayed in three dimensions using Blender 3-D. The light source is positioned at a zenith angle of  $55^\circ$

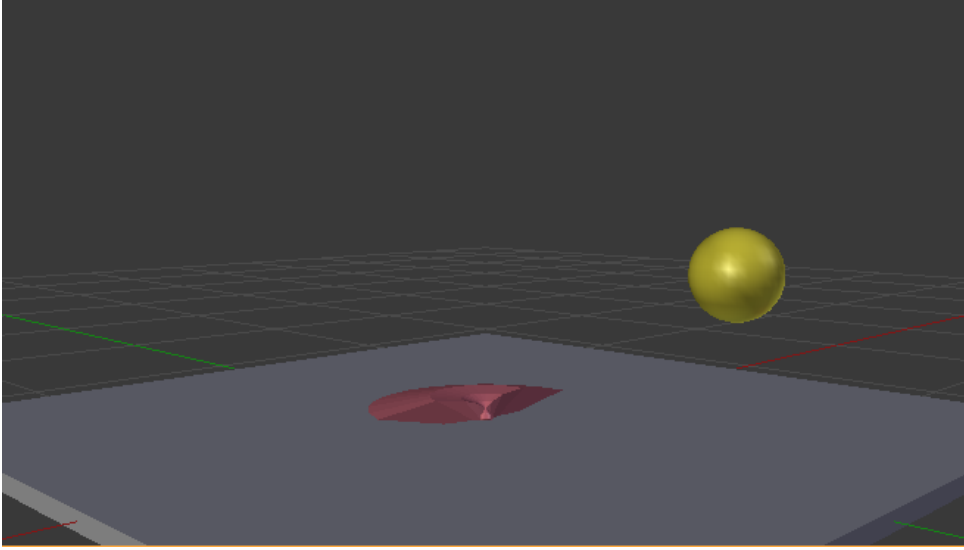


FIGURE 5.10: DIRSIG rendered BRDF of the tire track scene. BRDF is displayed in three dimensions using Blender 3-D. The light source is positioned at a zenith angle of  $75^\circ$

### 5.2.2 Modeling the Effects of Porosity and Particle Size

Section (4.6) discussed the experimental methods for the radiometric simulation of particle scenes with varying size distribution and chemical content. First, scenes of quartz soil were created. Three different size distributions of pure quartz were used to build targets with Blender 3-D. A high-density and a low-density target was formed for each distribution of quartz. In all, six pure quartz targets were used for simulation with the DIRSIG virtual goniometer.

BRDF values were simulated for quartz scenes at intervals of  $20^\circ$  between zenith angles of  $-60^\circ$  and  $60^\circ$  in the principal and perpendicular planes. These two measurement planes are defined by the positions of the illumination source and the virtual sensor. Measurements are said to be in the principal plane if the source and sensor share the same azimuth angle or if the source and sensor have azimuth angles that are separated by  $180^\circ$ . In the perpendicular plane, the sensor azimuth is positioned  $90^\circ$  from the source azimuth. Both measurement scenarios are illustrated in Figure (5.1).

For each of the three distributions, the low-density simulation results are plotted with the high-density results. BRDF percentage is plotted against sensor zenith angle. The zenith plane position of the illumination source is indicated in plots of the principal plane. The data provides some interesting insights into the impact of particle size distribution. As was previously stated, the relationship between soil density and reflectance has been

modeled and observed with some variance in results. Several observations indicated that a dense geometry of soil is more reflective than a sample with lower density (Capaccioni et al., 1990, Georgiev et al., 2009, Kaasalainen, 2003, Dematte et al., 2010, Shepard and Helfenstein, 2011). Models have confirmed this result (Hapke, 2012b). However, observations by Bachmann et al. (2014) indicate that the relationship between density and reflectance may be more complicated.

The model results displayed in Figure (5.11) support both claims. The signature gathered from the uniform distribution (Figure (4.14a)) indicates that at backscattering view angles, the dense sample is more reflective than quartz that is less dense. As the sensor moves to positions associated with forward scattering, less dense soil is more reflective. It was observed by Peck et al. (2015) that the position of the scene illumination source might also contribute to these trends. It is also noted that reflectance fall off in the perpendicular plane is not truly uniform. This indicates that particle geometry and size distribution have an observable effect on soil signatures. For a sample that contains particles of many sizes, such as the uniformly distributed soil, it is likely that much of the available pore space will be filled as soil settles. At higher densities, pores may fill completely. This results in a varied distribution of large and small particles at the topsoil layer. In the backscatter direction, porous light traps become rare and smaller particles can be sensed. In the forward scattering direction, shadowing is prevalent. Any light that does bounce from small grains into the forward scattering direction will likely be blocked by large particles before it can reach the sensor. If a sample of the same distribution was less dense, larger grains would dominate the geometry of the topsoil and shadowing in the forward direction would be less severe. These trends are observed in the results corresponding to the uniform distribution of quartz, and they are displayed in Figure (5.11).

A different trend is evident when the geometry of the soil surface is represented by the bimodal and unimodal distributions. Lower density samples of both distributions were modeled to have stronger reflectance signatures than more dense samples of the same distribution (Figure (5.12)). This implies that for the samples in this experiment, pore spacing was measureable. In the scenes depicting dense soil representations of these narrow size distributions, grains on the very top surface of the sample tended to settle relatively far from one another. This geometric separation of large particles resulted in an observable variance in surface height. When bimodal and unimodal distributions were used in less dense Blender 3-D scenes, grains at the top surface were more tightly grouped. The change of top surface height in these scenes was less severe. This difference in topsoil surface height has been used previously in physical optics based BRDF models and is referred to as *effective surface roughness* (He et al., 1991). This implies that even

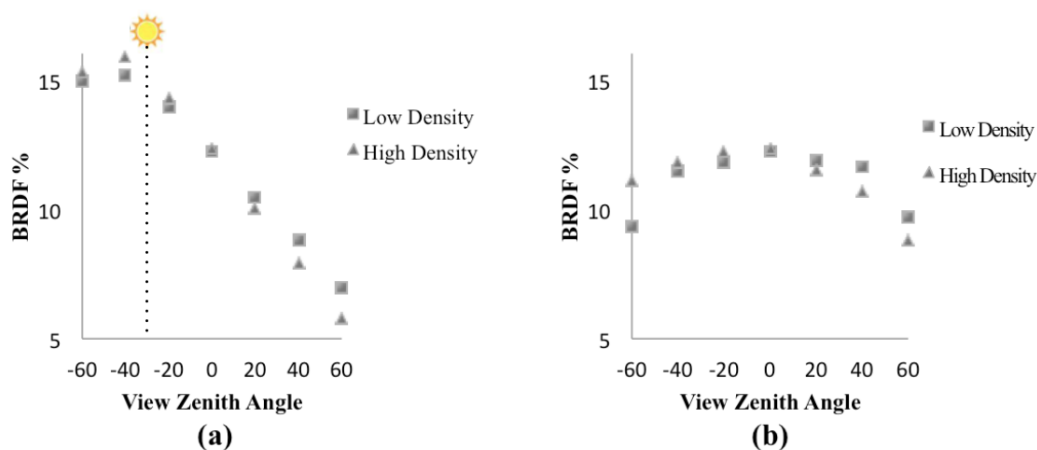


FIGURE 5.11: BRDF of quartz at 650nm is plotted in the principle plane (a) and perpendicular plane (b) for a uniform particle size distribution. The effect of density on BRDF varies based upon sensor location. The location of the illumination source in the principal plane is indicated by the sun icon

if the same particle size distribution is manifested in two separate samples, these samples can have different surface texture. Such a change ultimately alters the level of measured signal. It explains how a less dense sample, with a very specific particle size distribution, will be observed to be more reflective than soil with higher density.

An additional test was performed to explore the believability of the aforementioned results. To ensure that the trends shown in Figures (5.11-12) were not simply the product of unique geometry, additional simulations with different geometric deposition were carried out and the variability of the produced reflectance was calculated. Three additional scenes were created using the Blender 3-D physics engines. The bimodal particle size distribution was used in each scene. The same number of particles was used in each scene. The only difference between the simulations was the initial positioning of the rigid body particles prior to implementation of the physics engine. Standard deviations were calculated for each BRDF value. This deviation is plotted with the original BRDF results in Figure (5.13). There was overlap between the standard deviations of the low-density and high-density quartz signatures. Only three of the fourteen low-density data points were within a standard deviation of the high-density trend line. The model seems to consistently predict that a low-density sample of quartz that is defined by the aforementioned bimodal distribution will reflect more light than a higher density soil that shares the same distribution.

The bimodal particle size distribution was also used to evaluate the effects of density for soil samples that contained a mixture of quartz and magnetite particles. Within the

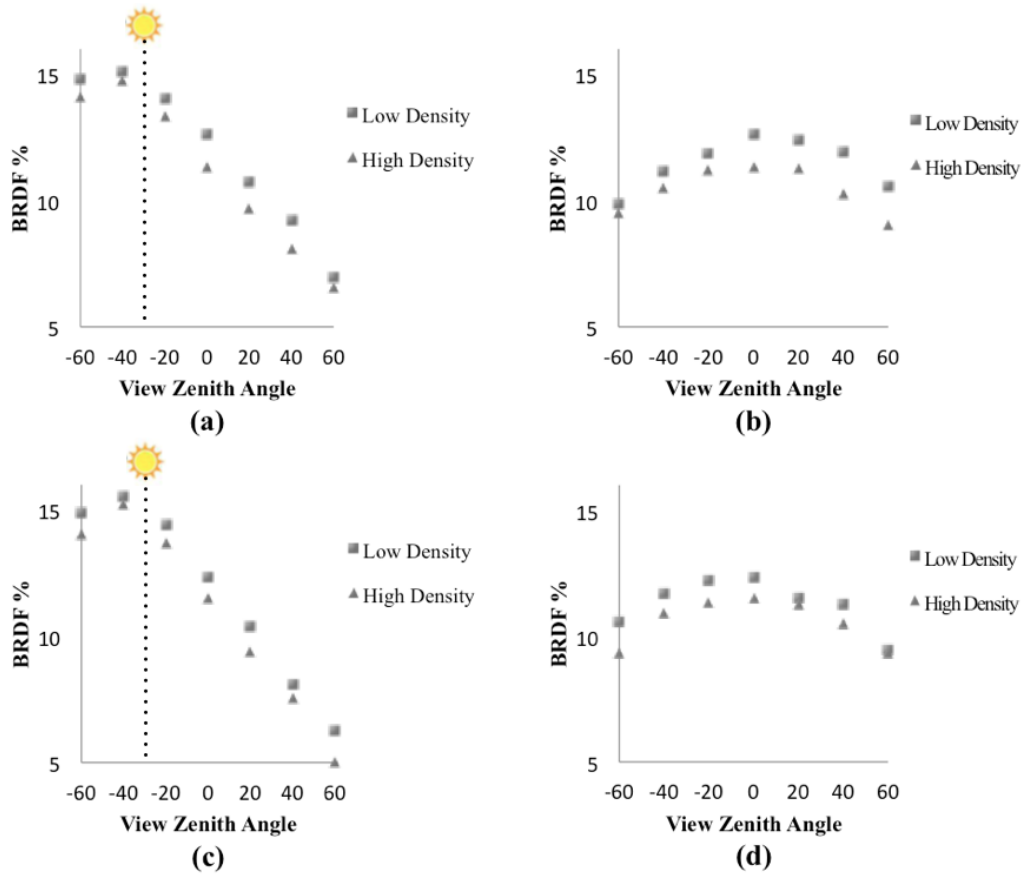


FIGURE 5.12: BRDF at 650nm is plotted in the principal plane (a,c) and perpendicular plane (b,d) for a bimodal particle size distribution (a,b) and a unimodal particle size distribution (c,d). In both scenarios, low-density soil appears more reflective than high-density soil.

Blender 3-D sample, small particles ( $106$  and  $150\mu\text{m}$ ) were given the spectral signature of magnetite. All particles larger than  $150\mu\text{m}$  were represented as pure quartz. This distribution was used because it closely resembled the distribution observed by Bachmann et al. (2014)]. In that paper, soil that was denser was observed to reflect less than sand with higher levels of porosity. It was assumed that this result was a consequence of small black magnetite particles that more completely fill pore spaces when soil is dense. To test this, a DIRSIG simulation was created using the scene described above. The illumination source was positioned  $20^\circ$  from nadir in the zenith plane. BRDF values were calculated in the visible and shortwave infrared (SWIR). The reflectance characteristics of the mixed soil are compared with pure quartz in Figure (5.14).

This DIRSIG-based model shows that the results observed by Bachmann et al. (2014) may have been partially caused by the particle size distribution of the sample soil.

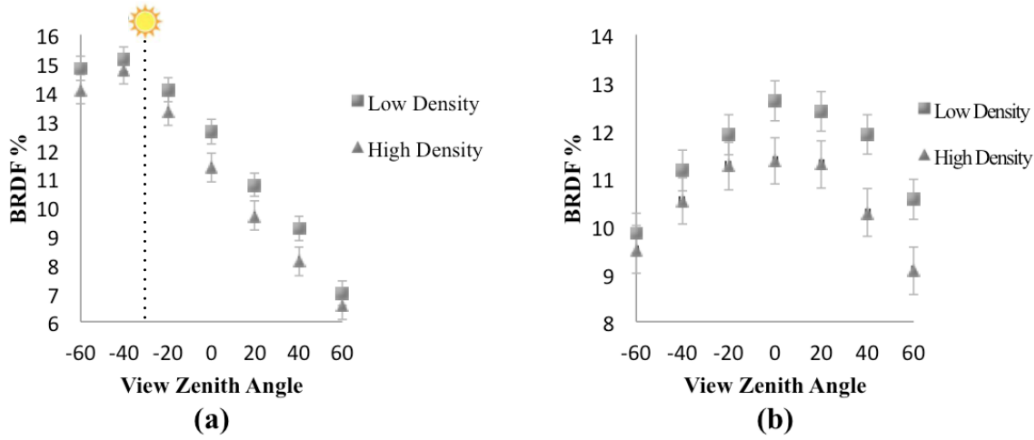


FIGURE 5.13: Mean and standard deviation from three separate scenes of similar particle size distribution and density were plotted in the principal (a) and perpendicular plane (b). The lack of overlap in the trend lines suggests that the model will consistently predict that soil samples with bimodal distributions will be more reflective in low-density scenarios.

The plots in Figure (5.14) also confirm the notion that the effects of magnetite are more pronounced in high-density samples. Figure (5.14a-c) correspond to a high-density soil sample and reveal a noticeable decrease in the reflectance of soil containing small magnetite grains. A much smaller reflectance gradient exists in Figure (5.14d-f), which describe a low-density sample. Bachmann also observed there to be greater variance in measurements collected in the SWIR. The spectral reflectance of quartz contrasts more with the reflectance of magnetite in this regime (Bachmann et al., 2014). This trend is observed in the simulation results displayed in Figure (5.14). All plots in this figure include standard deviation error bars which were calculated using the reflectance simulation of 5 separate geometric representations of the respective high and low density scenes. Standard deviation is larger in the low-density scene. Not only is the reflectance gradient in the  $450nm$ ,  $1000nm$ , and  $1915nm$  bands less distinct for the less-dense scene, there is less certainty in the results. This is a product of transient porosity features in the 5 different simulations of the low-density scene. There was less change in porosity between each representation of the high-density scene.

For a bimodal distribution, spectral contrast due to density has been observed to increase as phase angle increases (Bachmann et al., 2014). The DIRSIG model presented in this work also predicts this tendency. Figure (5.15) shows that the increase in contrast of a quartz and magnetite mixture occurs at visible and shortwave infrared wavelengths. As expected, contrast is greater in the SWIR, and increases with larger phase angles. This simulation did not consider coherent scatter beyond that which was captured in

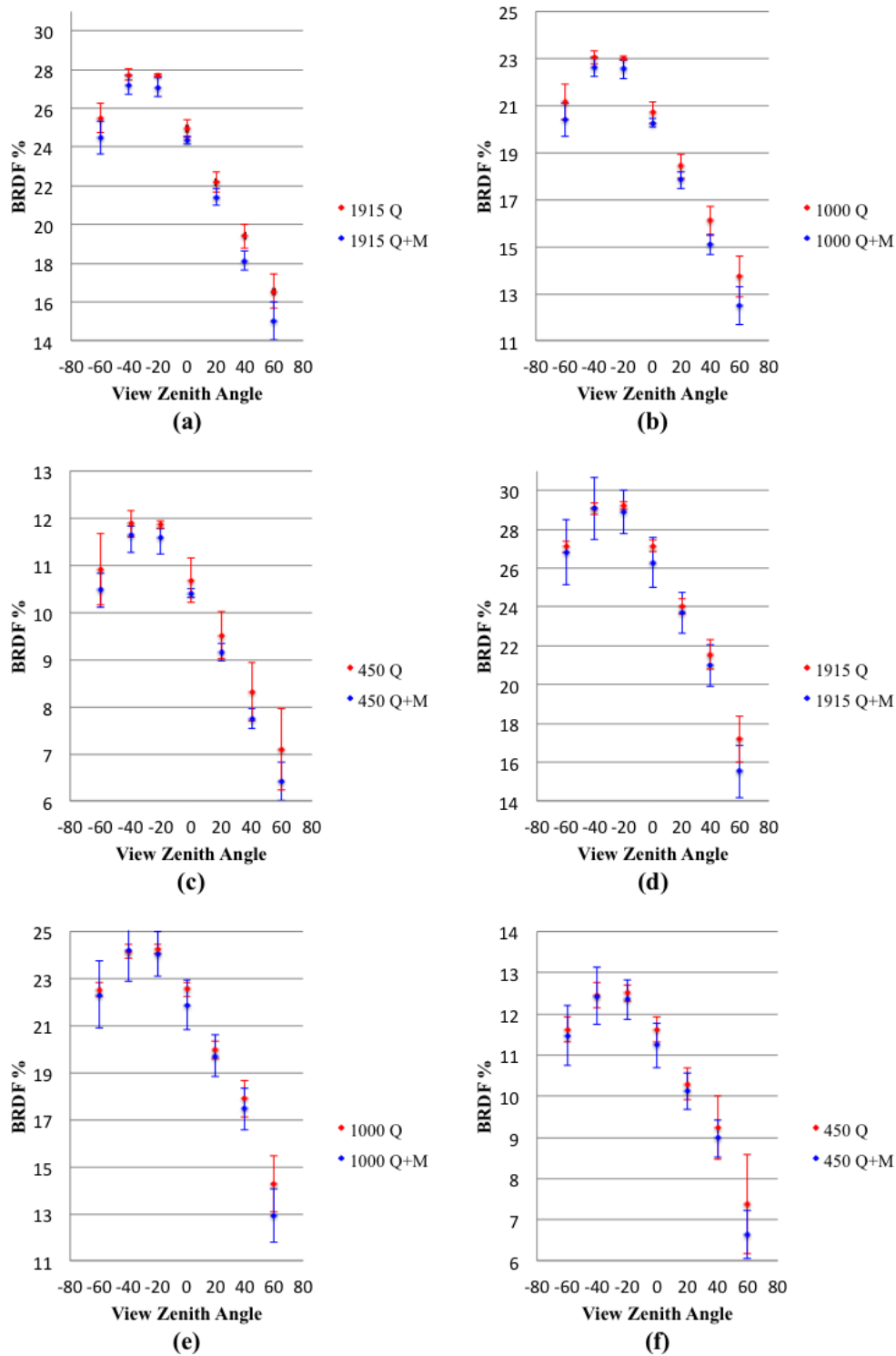


FIGURE 5.14: BRDF results from different mixture and density scenarios were plotted in the principal plane at 1915, 1000, and 450 nm. In the high-density plots (a-c), the impact of intimate mixing between magnetite and quartz was defined by a noticeable drop in reflectance at all viewing angles. There was very little variance between the BRDF of mixed soil and pure quartz in the low-density scenario (d-f). In each simulation, the illumination source was positioned with a zenith angle of 20°.



the reflectance measurements of the USGS. Therefore, the trend of increasing contrast that was observed by Bachmann et al. (2014) can be at least partially attributed to the intricacies of soil geometry that are associated with pore spacing, particle size and surface texture.

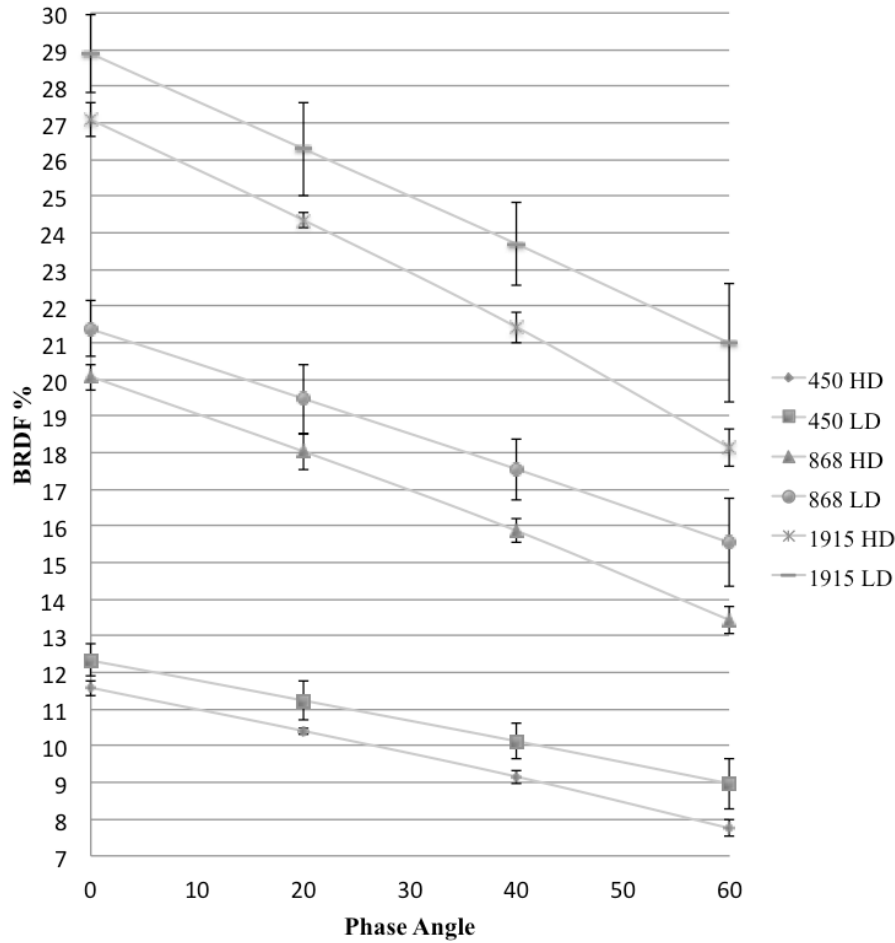


FIGURE 5.15: Variance between the reflectance of high-density soil and low-density soil for a bimodal distribution of magnetite and quartz was shown to increase as phase angle increased. The effect was more dramatic in the SWIR. These effects have been observed in previous lab analysis (Bachmann et al., 2014).

### 5.3 BRDF Simulation Using the NEFDS

A simulation was performed to model soil contamination upon a piece of painted blue car metal. Painted metal reflects light in specular fashion, so the accuracy of the BRDF measurements depend on the inclusion of accurate directional reflectance material files.

The Non-conventional Exploitation Factors Data System (NEFDS) contains the directional reflectance description for blue car paint. Contamination scenes attributed with DHR derived material files and NEFDS material files were simulated using goniometric sensing in DIRSIG. It was expected that a non-Lambertian BRDF would be generated, and that reflectance trends could be modeled with the percentage of contamination surface coverage.

Figures (5.16-19) show the contamination scene and the BRDF simulations created using NEFDS and DHR derived material files. For each of the car scene simulations, the illumination source was modeled with a  $30^\circ$  zenith angle. Several trends can be noted. There is little difference between results simulated with NEFDS and Non NEFDS material files for scenes that include high levels of contamination coverage (Figures (5.16-17)). This is because the primary material being sensed by the imaging platform is soil, which scatters less directionally than the blue car paint. Both NEFDS material files and DHR files predict that the magnitude of blue band reflectance will begin to dwarf the green and red bands as more blue car paint is exposed.

Principal plane plots generated using the NEFDS in Figures (5.16-19) also help to explain the geometric scattering of soiled surfaces that were evaluated in Section (5.1). In these two figures, the backscatter BRDF characteristics match those of the original soil scene described in Section (5.1). In the direction of specular scatter, a lobe emerges as photons begin to interact with the intimate mixture of soil and car paint. Within this lobe, the BRDF magnitude of the blue band approaches, and eventually exceeds the magnitude of the the green and red bands. This shows that the DIRSIG tool is capable of capturing both red band dominant backscatter of radiation and the directional diffuse/specular reflection that is characteristic of blue car paint. It is apparent that the specular forward scatter becomes more definitive as the contaminant is removed from the metal car surface. As this occurs, contrast between the spectral bands increases when viewed in the forward scattering direction. Also, the BRDF magnitude of the blue band meets or exceeds that of the red and green bands at all view angles when surface coverage falls below 44% (Figures (5.18-19)).

The removal of soil from the scene creates a BRDF feature in the perpendicular plane that is omitted when DHR material files are used exclusively. Strong specular lobes are not seen in the perpendicular plane, but a noticeable peak does emerge in correspondence with the nadir viewing position. The perpendicular plane plot derived from DHR files (Figure(5.15)) predicts a more Lambertian reflectance curve.

After performing analysis on the contamination scenes with  $30^\circ$  illumination zenith, the study was extended to explore signature variations due to light source position.

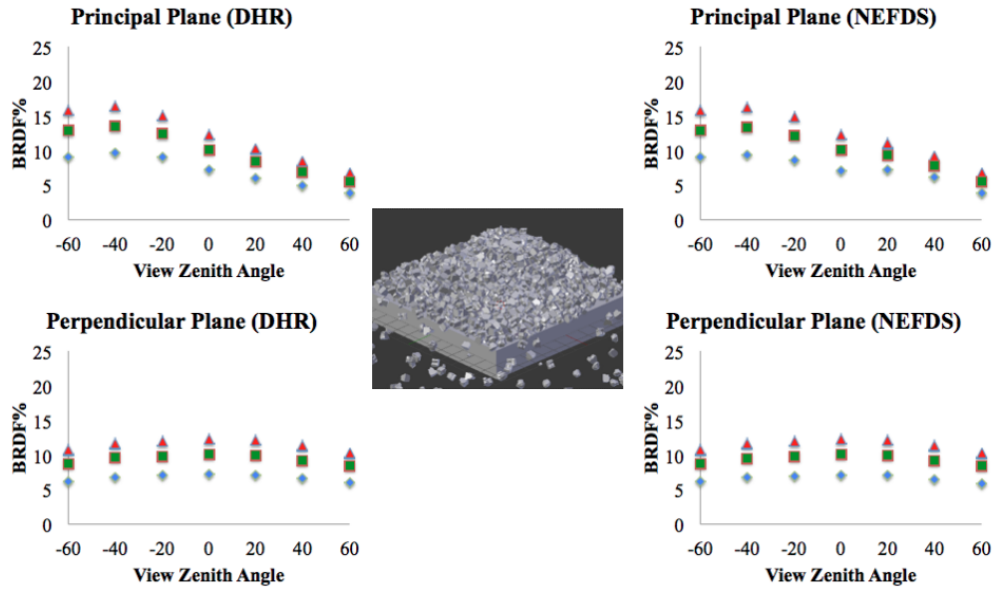


FIGURE 5.16: BRDF simulation results for Car Scene 1 (98% surface coverage). Paint and soil DHR material files were used to create the two plots on the left. Directional reflectance data from the NEFDS was used to produce the curves on the right. The image in the center is the Blender 3-D representation of the sample scene. Data was simulated at 650 (red), 550 (green), and 450 nm (blue).

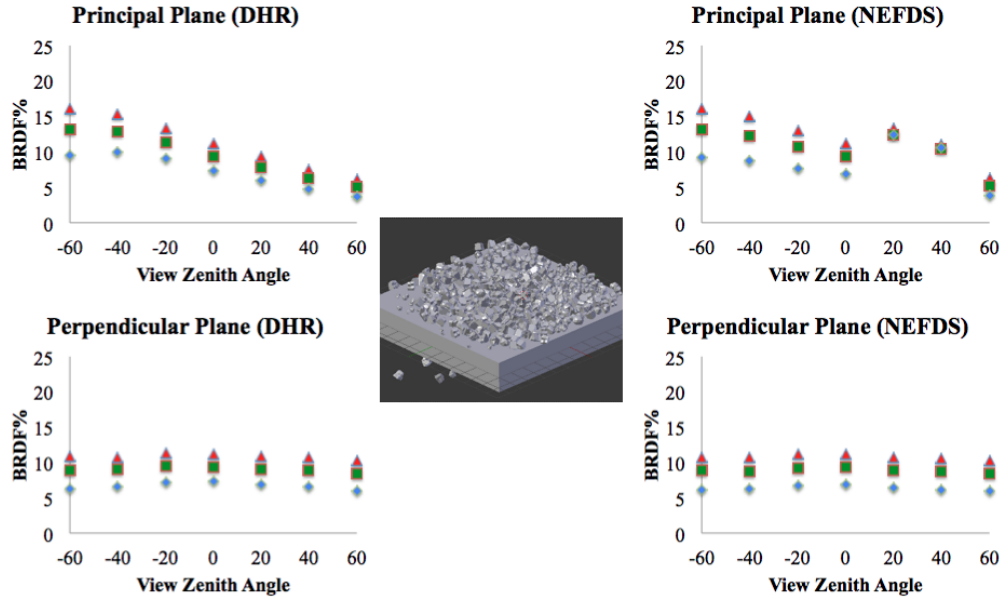


FIGURE 5.17: BRDF simulation results for Car Scene 2 (90% surface coverage). Paint and soil DHR material files were used to create the two plots on the left. Directional reflectance data from the NEFDS was used to produce the curves on the right. The image in the center is the Blender 3-D representation of the sample scene. Data was simulated at 650 (red), 550 (green), and 450 nm (blue).

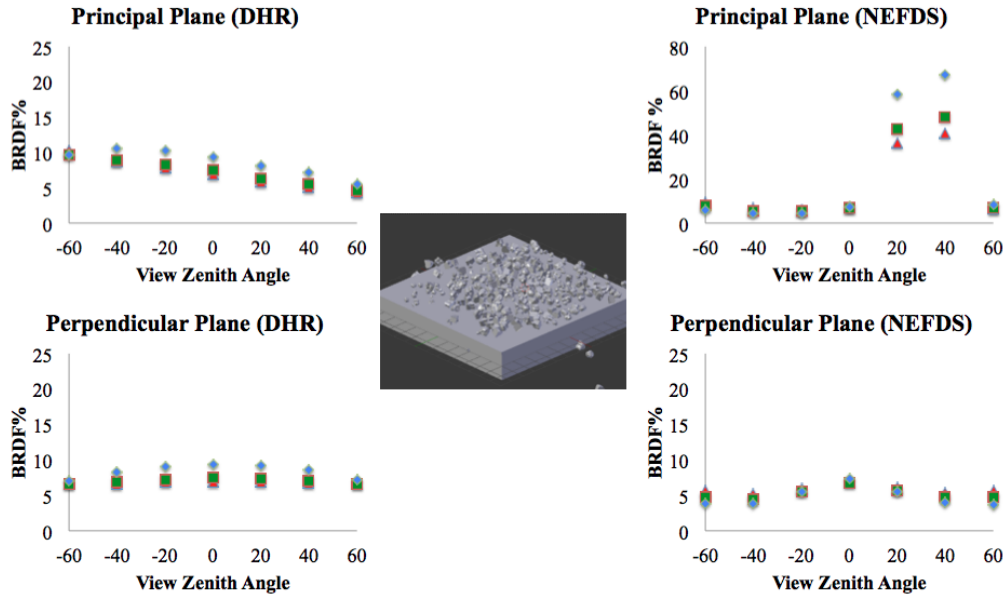


FIGURE 5.18: BRDF simulation results for Car Scene 5 (44% surface coverage). Paint and soil DHR material files were used to create the two plots on the left. Directional reflectance data from the NEFDS was used to produce the curves on the right. The image in the center is the Blender 3-D representation of the sample scene. Data was simulated at 650 (red), 550 (green), and 450 nm (blue).

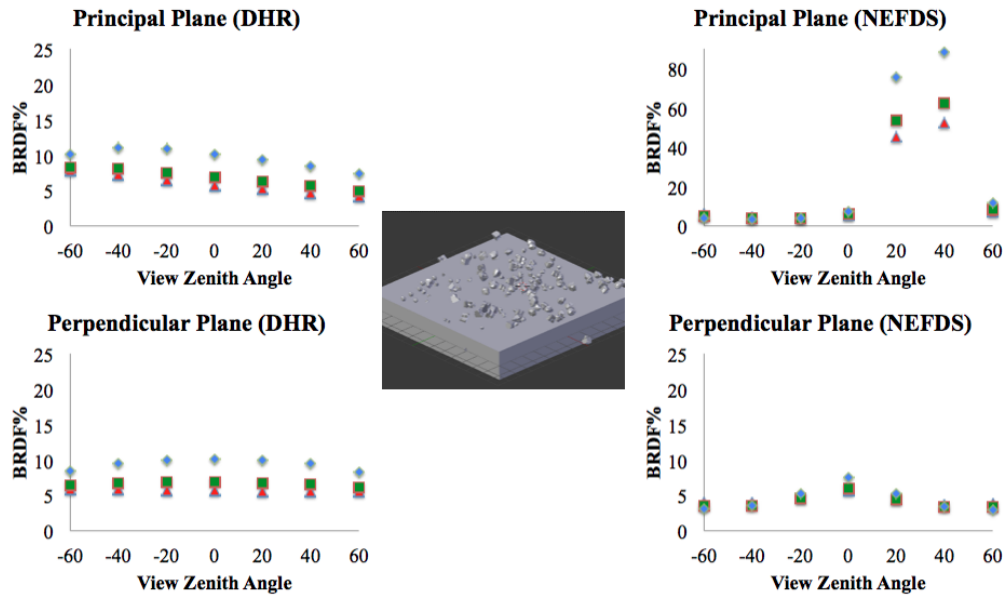


FIGURE 5.19: BRDF simulation results for Car Scene 6 (27% surface coverage). Paint and soil DHR material files were used to create the two plots on the left. Directional reflectance data from the NEFDS was used to produce the curves on the right. The image in the center is the Blender 3-D representation of the sample scene. Data was simulated at 650 (red), 550 (green), and 450 nm (blue).

Additional data was collected for source zenith angles of  $0^\circ$  and  $50^\circ$ . With a source positioned at nadir, BRDF falls off sharply when the sample is viewed at zenith angles greater than  $20^\circ$ . When there is a large amount of contaminant coverage, reflectance is fairly uniform at sensor positions of zenith  $> 20^\circ$ . As contaminant is removed, diffuse scatter from the soil particles is reduced, and reflectance falls off further for view zenith  $> 40^\circ$ . This change in signature can be observed in Figure (5.20).

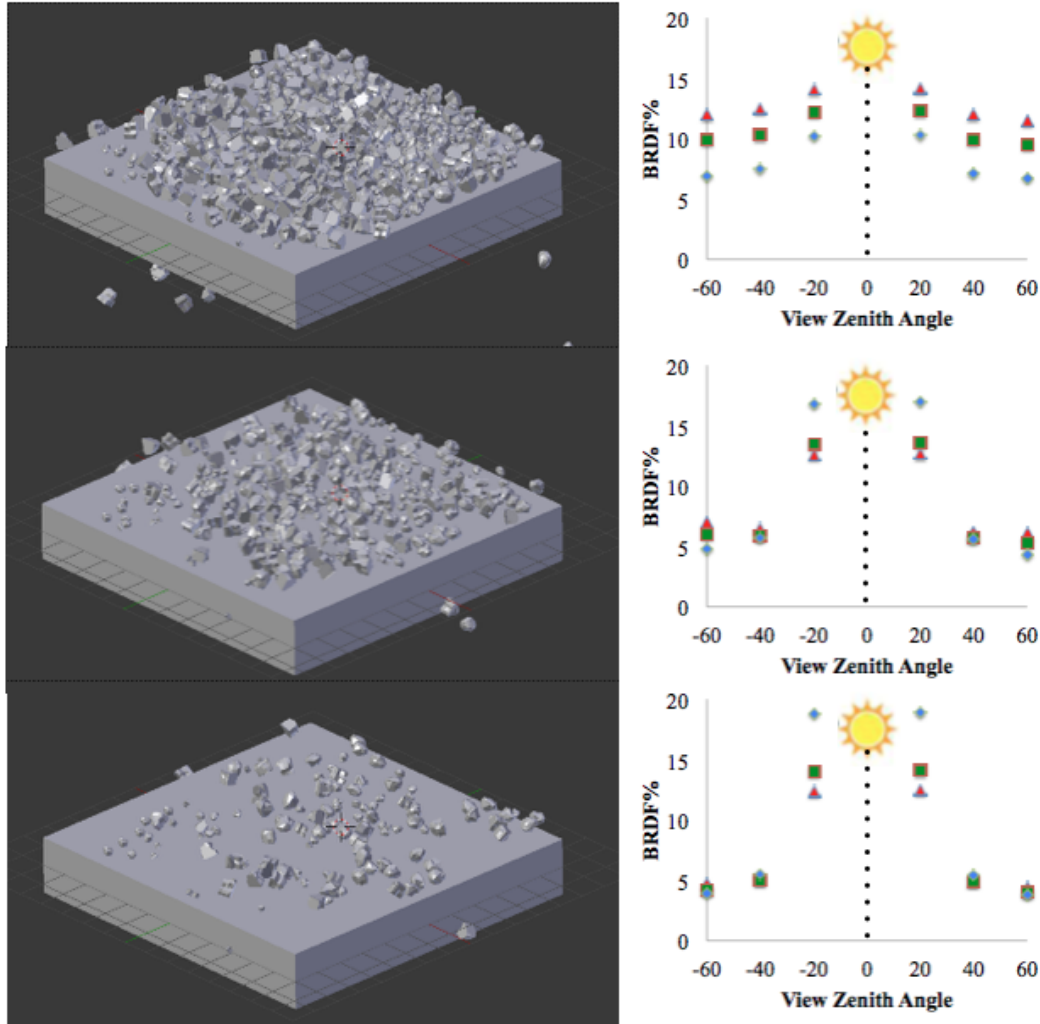


FIGURE 5.20: BRDF car contamination simulation results for 90% coverage (top), 44% coverage (middle) and 27% coverage (bottom). The scene light source was positioned at nadir. Reflectance falls off at zenith angles  $> 40^\circ$  as soil contamination is removed

When the light source was positioned with a zenith angle of  $50^\circ$ , several BRDF features were evident. In the principal plane, the backscatter hot spot was sensed at a zenith location between  $40^\circ$  and  $60^\circ$  from nadir. It makes sense that the back scatter peak

would shift to larger zenith angles as the source is positioned lower in the sky. The forward scatter lobe also exhibited the same angular shift in the zenith plane. The other significant characteristic of this geometry is that shadowing effects and backscatter are observed at zenith angles between nadir and  $20^\circ$ . This indicates that more occlusion is occurring in the  $50^\circ$  source zenith scene compared to simulations performed with a zenith angle of  $30^\circ$ . A reduction in BRDF magnitude is a consequence of the increasing levels of occlusion. The BRDF curves for the  $30^\circ$  source scene and the  $50^\circ$  source scene are displayed in Figure (5.21).

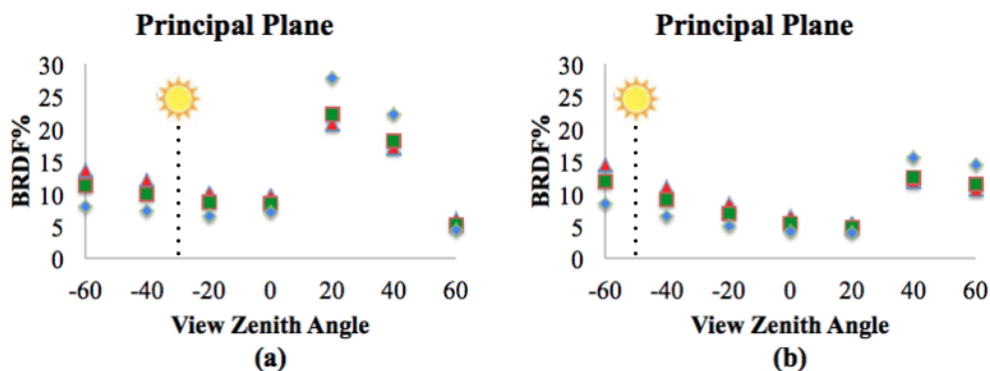


FIGURE 5.21: BRDF car contamination simulation results for 74% coverage. The plot (a) was generated with an illumination source positioned at a zenith angle of  $30^\circ$ . There is noticeable change in reflectance magnitude and sample occlusion when the light source is relocated to a zenith position of  $50^\circ$  from nadir. Data was simulated at 650 (red), 550 (green), and 450 nm (blue).

Simulation was also used to describe how the magnitude of average reflectance in the visible regime changes with surface coverage. Plots were formed for 450nm radiation at three different light source positions ( $0^\circ$ ,  $30^\circ$  and  $50^\circ$  zenith).

When the light source was positioned at nadir, simulation results show that there is a quadratic, if not nearly linear, relationship between average reflectance and surface coverage (Figure (5.22)). This is true at nadir (Figure (5.22a)), and at larger phase angles (Figure (5.22b)). At phase angles between 0 and  $40^\circ$ , the trend line has a negative slope, indicating that the amount of detected blue light decreases as the soil contamination level increases. At phase angles greater than  $40^\circ$ , the trend line exhibits a positive slope. This is non-intuitive trend highlights the impact that directional scatter has upon BRDF. The painted metal reflects light directionally. When the radiation source is placed at nadir, the majority of light rays will reflect backwards towards the source. Very little is scattered in the direction of larger phase angles. This explains why small BRDF magnitudes are observed when contamination coverage is low. When more of the surface is covered with soil, uniform scattering begins to dominate. More radiation is

scattered in the direction of large phase angles. This is why 450nm BRDF magnitude actually increases with increasing levels of surface coverage. It is encouraging to see DIRSIG successfully simulate the transition between scattering phenomenologies and produce believable signature trends.

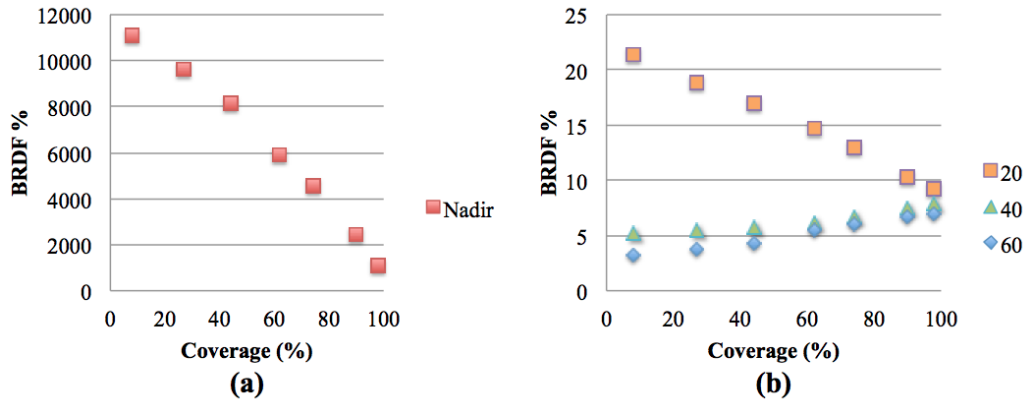


FIGURE 5.22: DIRSIG was used to model 450nm BRDF with surface coverage. For simulations with the illumination source positioned at nadir, BRDF scales quadratically (nearly linearly) with surface coverage. Trend lines for nadir viewing (a) and 20° declination (b) have negative slopes, indicating that the light reflection observed at these locations is dominated by specular scatter. Trend lines for 40° and 60° declination (b) have positive slopes. This is the result of uniform scatter from the soil contaminant.

When the position of the illumination source was positioned at a 30° zenith angle, BRDF trended nearly linearly with the percentage of surface coverage at all sensing positions along the principal plane except for one. This can be seen in Figure (5.23). Figure (5.23a) shows that at backscatter viewing positions (-20°, -40°, and -60°), trend lines slope positively with increasing surface coverage. This indicates that light detected at these view angles is primarily scattered uniformly by the soil contaminant. Figure (5.23a) reveals that the relationship between BRDF and surface coverage becomes more nonlinear only at very large backscatter zenith angles (-60°) when the surface coverage exceeds 87%. The shadowing and occlusions resulting from large zenith illumination and view angles precipitate the nonlinear trend. The impact of illumination zenith angle is highlighted here as this nonlinearity was not observed in simulations with the illumination source positioned directly above the target (Figure (5.22)). At nadir, and at view positions in the forward scatter direction (20°, 40°, and 60°), BRDF trends negatively with increasing levels of surface coverage. This relationship (Figure (5.23b)) characterizes the reduction of specular scatter with added surface contamination.

As larger illumination zenith angles are incorporated into simulation, the relationship

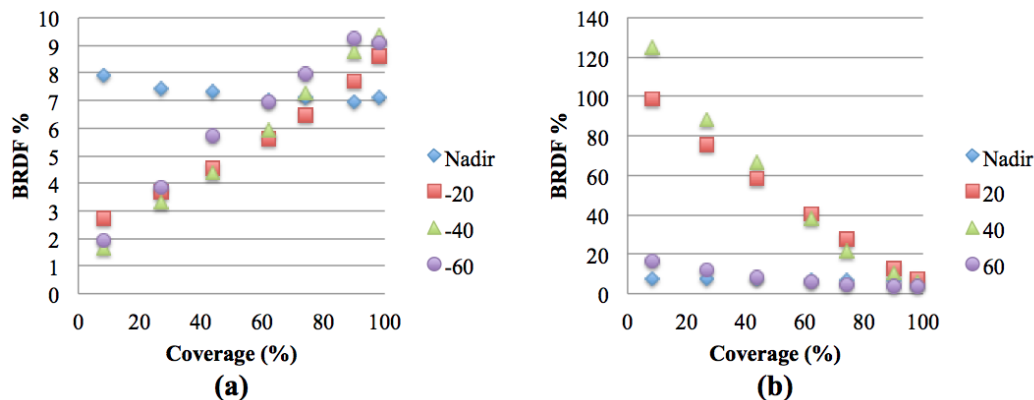


FIGURE 5.23: DIRSIG was used to model 450nm BRDF with surface coverage. For simulations with the illumination source positioned at  $30^\circ$ , BRDF scales linearly with surface coverage at all viewing positions other than  $-60^\circ$  zenith. Trend lines for backscatter (a) have positive slopes. This is the result of uniform scatter from the soil contaminant. Trend lines for nadir and other forward scatter view positions (b) have negative slopes, indicating that the light reflection observed at these locations is dominated by specular scatter.

between BRDF and surface coverage becomes nonlinear at forward scattering view positions. Figure (5.24b) shows that when the illumination source was positioned at  $50^\circ$  zenith, the shadowing and occlusion of particles becomes noticeable at lower levels of contamination coverage. The trend is accentuated at forward scattering view positions  $> 40^\circ$  zenith.

## 5.4 Soil Signatures in the LWIR

In section 4.5.3, a method was developed to obtain hyperspectral BRDF and directional emissivity measurements in the LWIR. This process was applied to a scene created to geometrically describe disturbed soil. The scene included soil particles covered with fine micro-grains. Material files were applied to each grain based on particle diameter.

The ability to use realistic scene geometry with chemical properties assigned by particle size enabled the simulation of an intimately mixed complex soil signature. To tune the DIRSIG born signature to match *in situ* measurements, the particle scene was systematically altered by gradually removing fine particles from the larger sand grains. A scene with large particles that are completely covered with small fines should produce a spectral emissivity curve that looks similar to the emissivity of  $50\mu m$  particles. This was accurately simulated using DIRSIG. As the fines were removed (Figure (5.25)), the material properties of the larger particles were shown to have a greater impact on the



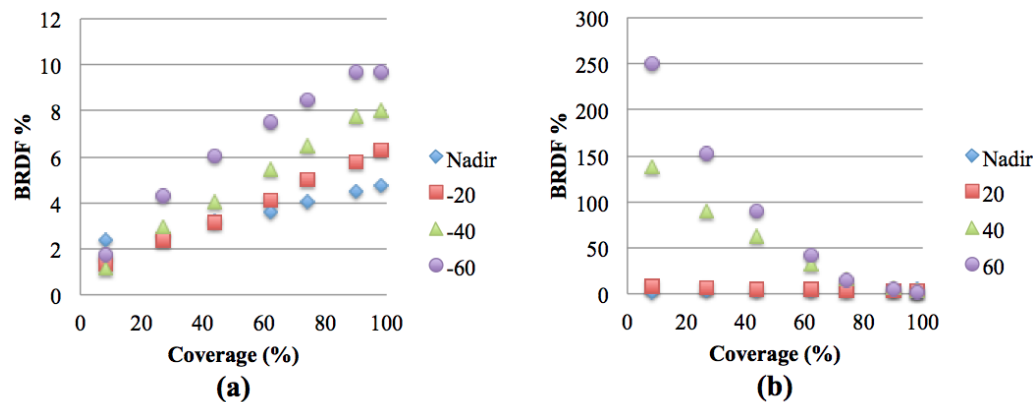


FIGURE 5.24: DIRSIG was used to model 450nm BRDF with surface coverage. For simulations with the illumination source positioned at  $50^\circ$ , BRDF scales linearly with surface coverage at all backscattering view positions other than  $-60^\circ$  zenith. Trend lines for backscatter (a) have positive slopes. This is the result of uniform scatter from the soil contaminant. Trend lines for nadir and other forward scatter view positions (b) have negative slopes, indicating that the light reflection observed at these locations is dominated by specular scatter. The association between BRDF and surface coverage at view locations  $> 40^\circ$  is nonlinear.

overall spectral signature of the mixed soil target. The desired scene geometry is the one that most closely represents the geometry and signature of disturbed soil.

A chart presenting the resulting emissivity signatures of this iterative process is shown in Figure (5.26). In the figure, the curve denoted as *fully covered* was simulated using large particles that are entirely covered with bits of dust (Figure (5.25a)). Some dust was removed in the scene of particles that were *less covered* (Figure (5.25b)). Even more fine grains were removed in the scene of *sparsely covered* particles. The relative spectral emissivity curve of sparsely covered particles (Figure (5.25c)) is very similar to the signature of disturbed soil presented by Johnson et al. (1998b). Results from this simulation also showed an increased spectral contrast, and lower relative intensity in the  $8 - 9.5\mu m$  spectral band compared to scenes dominated by finely powdered quartz (Salisbury and Wald, 1992, Moersch and Christensen, 1995).

Analytical evaluation of Figure (5.26) reveals that simulation results agree with the expected theoretical balance between surface reflection and volume transmission. The Christensen frequency of quartz emerges at approximately  $7.4\mu m$ . This frequency is a benchmark because it defines nearly complete volume transmission. In this frequency region, the real part of the complex index of refraction of quartz approaches one. Air also has an index of refraction of approximately one at this wavelength. The result is the effective absence of grain boundaries. This distinct spectral feature is evident at

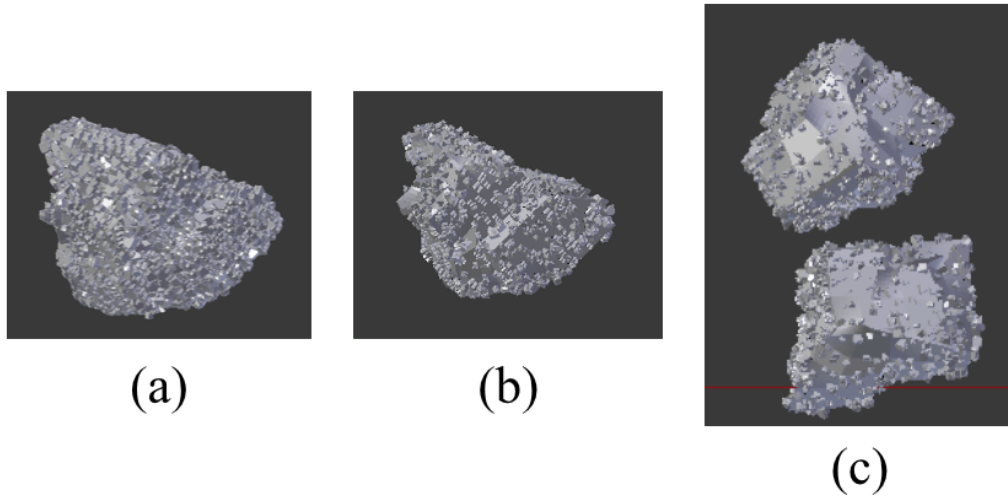


FIGURE 5.25: In (a), particles are fully covered in clinging fines. Large particles are covered less in (b), and sparsely covered in (c). The emissivity curves that correspond to these changing particle configurations show how signature varies with target geometry.

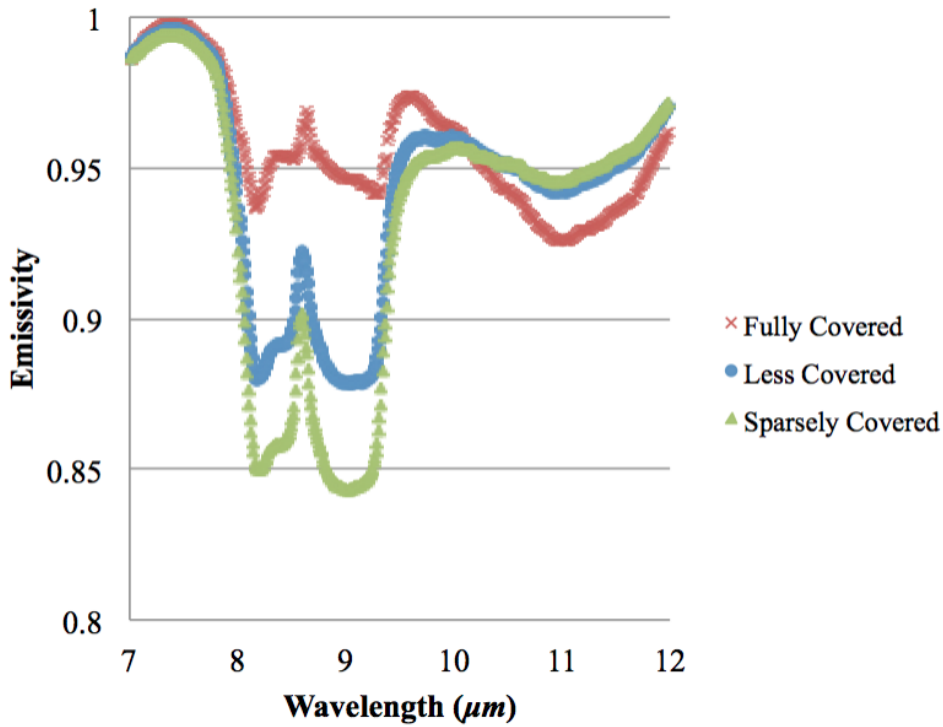
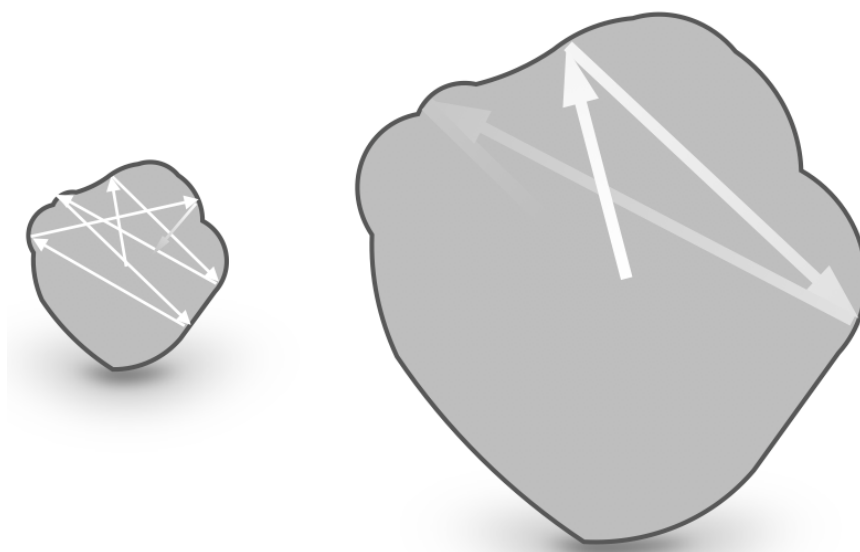


FIGURE 5.26: Emissivity is modeled with varying amounts of clinging fines. The fully covered curve (red) corresponds to a geometric representation of soil particles that are completely covered with micro-fines. The shape and magnitude of the reststrahlen band troughs changes as micro-fines are gradually removed from the target scene. This is observed in the less covered scene (blue) and in the sparsely covered scene (green).

7.5 $\mu\text{m}$  in Figure (5.26).

The impact of particle size in the reststrahlen bands has been modeled with great difficulty in the past (Moersch and Christensen, 1995). In the 8-9.5 $\mu\text{m}$  region characterized by primary reststrahlen effects, quartz is defined by a large imaginary component of its complex index of refraction. This means that radiation is subjected to many Fresnel reflections at these wavelengths. It also implies that energy cannot easily pass through quartz grains. Therefore, emissivity in this spectral region is defined by two substantial troughs. It has been observed that smaller grains in this region emit at higher levels than do larger quartz particles (Salisbury and Wald, 1992, Johnson et al., 1998b, Moersch and Christensen, 1995). Both Salisbury and Moersch attribute this trend to the increase in volume scatter that is sensed at the top layer of a target (Salisbury and Wald, 1992, Moersch and Christensen, 1995). Moersch explains that there are more pre-reabsorption interactions between thermal radiation and grain boundaries in small particles. More interactions translates to more opportunities for emission in this wavelength range. The graphic in Figure (5.27) helps to illustrate the correspondence between particle size and emission in this regime that is defined by Fresnel reflections. Figure (5.26) shows that the presence of clinging fine particles at the sample surface impacts the modeled signature as expected. Evidence of volume scatter in scenes of completely covered grains is evident in the flattened troughs of the reststrahlen bands. Decreased spectral contrast in this region of the curve also highlights the increased porosity and volume scatter that accompany small quartz particles. The reststrahlen region of the curve defined by sparsely covered quartz is a close match in magnitude and spectral contrast to the disturbed soil observed by Johnson (Johnson et al., 1998b).

Between 10 and 12 $\mu\text{m}$ , both volume transmission and Fresnel reflection occur in quartz. The imaginary portion of the index of refraction is very small and the real coefficient is approximately equal to two. Because volume transmission is significant in this regime, reabsorption is minimized in larger grains. This was not true in the 8-9.5 $\mu\text{m}$  region. Since reabsorption is low, larger particles exhibit higher levels of emissivity than do small particles. As was stated above, radiation from smaller particles must pass many grain boundaries before it is measured by a sensor. In the primary reststrahlen bands this characteristic made small particles more emissive than larger particles because reabsorption was prevalent. In the 10-12 $\mu\text{m}$  band, this very same characteristic is the purpose for lower emission levels displayed by smaller particles. This trend is described with accuracy in Figure (5.26). The emissivity curves of less covered and sparsely covered soil are impacted by the presence of large soil grains. The spectral signature of the scene of completely covered grains is almost entirely characterized by fine grains. Within the 10-12 $\mu\text{m}$  band, comparatively higher emissivity levels should be observed




---

FIGURE 5.27: Pre-reabsorption interactions between thermal radiation and grain boundaries depend on particle size. When compared to small particles, radiation emitted from large grains travels a longer optical path to experience the same number of radiation-boundary interactions.

in simulation results corresponding to the scenes of less covered and sparsely covered grains. This is demonstrated by this simulation approach.

## 5.5 Directional signatures of liquid contaminants

The signature simulation of mixed solids using DIRSIG is the primary subject of this research. Soil mixtures and mixed material contamination of dry solids have been modeled successfully. Using the goniometer of RIT (GRIT) and a fourier transform infrared spectroscopic (FTIR) sensor, liquid contaminants were also measured and modeled. Water and calcium chloride were used as contaminants in this study.

In the previous simulations of mixed solids, particles of different materials were mixed together using the Blender 3-D graphic design software. X-ray microanalysis revealed that liquid contamination could be observed on individual facets of particles. So to model liquid spills on soil, material properties were assigned to individual facets of each particle within a computer generated scene. In order to populate a model with materials and validate simulation results, directional reflectance and emissivity were measured for pure and contaminated targets (Figures (5.28-33)).

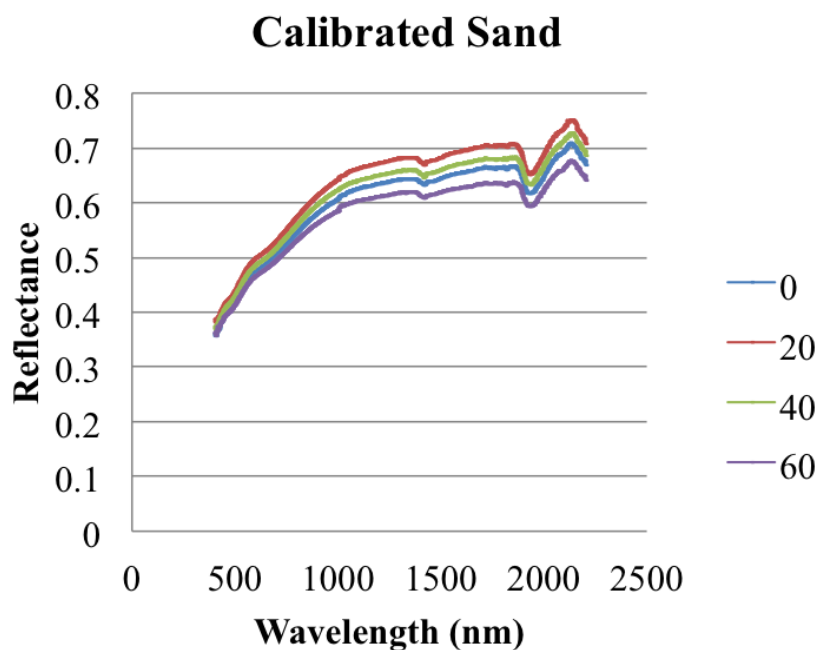


FIGURE 5.28: GRIT was used to capture the spectral reflectance of calibrated sand in the visible domain. Particle diameter within the target ranged between 0.3 and 2mm. Signatures were measured at zenith angles of 0, 20, 40, and 60° zenith in the forward scatter direction of the principal plane. The halogen light source used in this measurement was positioned with a zenith angle of 30°.

It was difficult to obtain spectral reflectance of liquid calcium chloride that was usable for simulation. Like water, liquid calcium chloride solution has very low reflectance in the visible and near infrared spectrum (between 1 and 3%). Unlike water, which evaporates over time, calcium chloride solution is hygroscopic and actively pulls moisture from the air. This is why it serves so well as a road treatment for dust control. This trait was observed in the laboratory at RIT. Liquid  $CaCl_2$  was oven dried for > 24 hours so that it could be measured for spectral reflectance. The dried sample is shown in Figure (5.34). Within one week, the sample had reverted completely to liquid form.

Since the spectrum of calcium chloride is transient due to changing humidity, the contaminated particles were modeled in DIRSIG by assigning some facets with the reflectance properties of wet sand, and other facets with the reflectance properties of baked calcium chloride. This is not the optimal geometry. Preferably, a scene created to model liquid contamination would not combine spatially separated facets of dry and wet materials. In order to ensure that the simulation would produce the best possible results, the wet sand used in simulation and the calcium chloride contaminated sand used for validation

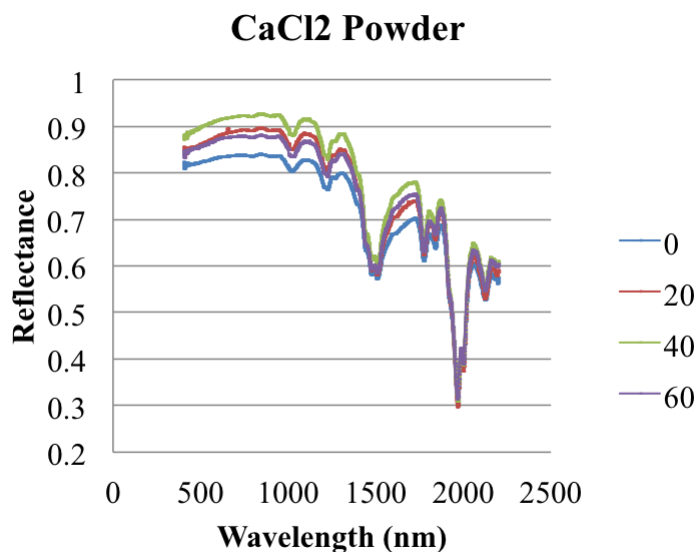


FIGURE 5.29: GRIT was used to capture the spectral reflectance of CaCl<sub>2</sub> powder in the visible domain. Signatures were measured at zenith angles of 0, 20, 40, and 60° zenith in the forward scatter direction of the principal plane. The halogen light source used in this measurement was positioned with a zenith angle of 30°.

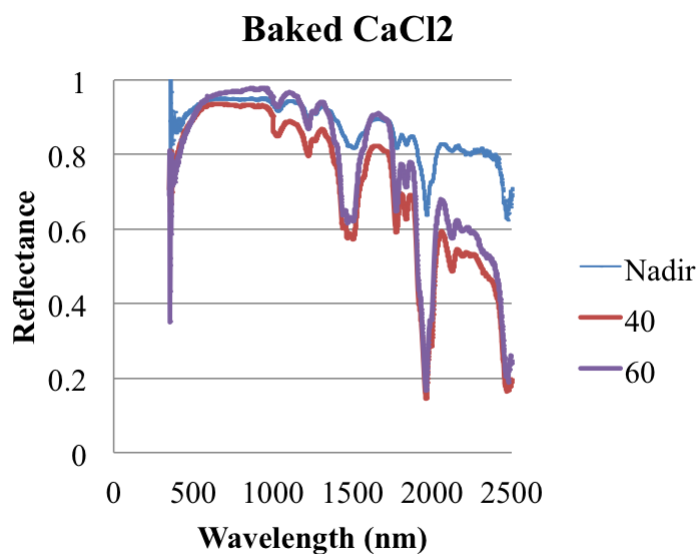


FIGURE 5.30: GRIT was used to capture the spectral reflectance of oven baked 38% CaCl<sub>2</sub> solution in the visible domain. Signatures were measured at zenith angles of 0, 40, and 60° zenith in the forward scatter direction of the principal plane. The halogen light source used in this measurement was positioned with a zenith angle of 30°.

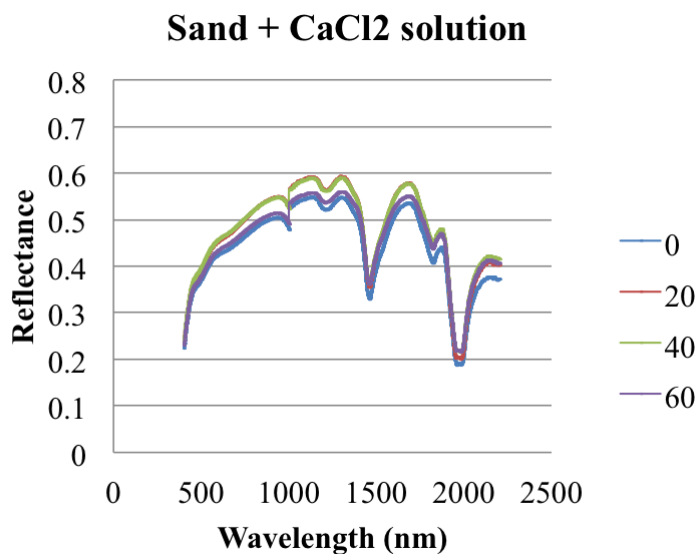


FIGURE 5.31: GRIT was used to capture the spectral reflectance of calibrated sand with 38% CaCl<sub>2</sub> solution in the visible domain. Signatures were measured at zenith angles of 0, 20, 40, and 60° zenith in the forward scatter direction of the principal plane. The halogen light source used in this measurement was positioned with a zenith angle of 30°.

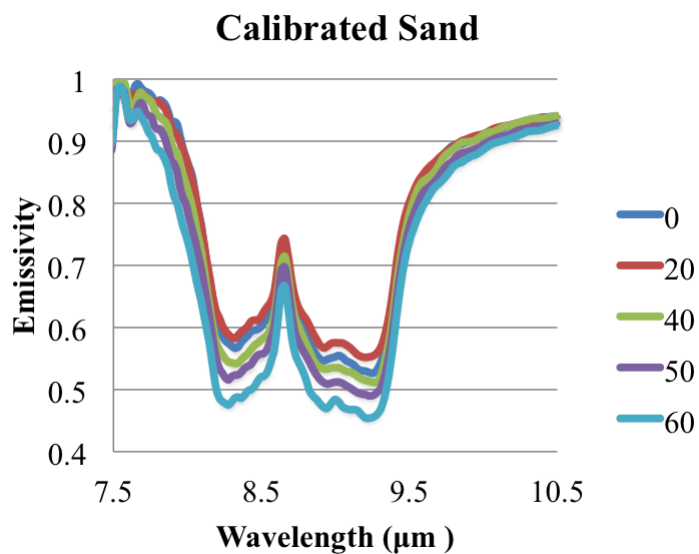


FIGURE 5.32: The D&P 102F microFTIR was used to capture the emissivity of calibrated sand in the LWIR. Signatures were measured at zenith angles of 0, 20, 40, 50, and 60°.

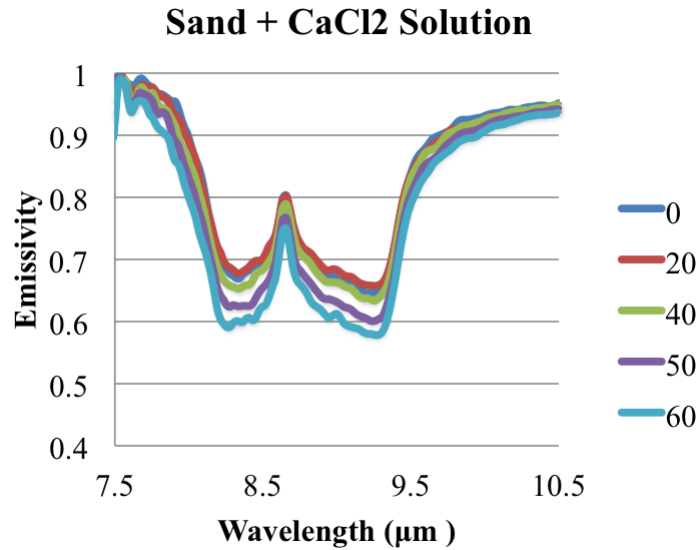


FIGURE 5.33: The D&P 102F microFTIR was used to capture the emissivity of calibrated sand with 38% CaCl<sub>2</sub> solution in the LWIR. Signatures were measured at zenith angles of 0, 20, 40, 50, and 60°.

were measured with the same volume moisture content (5.4%).

Measurements of wet sand and contaminated sand are plotted in Figures (5.35-36) alongside the DIRSIG simulation results. It is observed that at this specific volume moisture content, wet sand shares many of the spectral features observed in the reflectance signature of contaminated sand. This is not surprising as calcium chloride has absorption bands at 950, 1200, 1450, 1750, and 1950nm that are all produced by absorbed water molecules. At both nadir and at a phase angle of 40°, the DIRSIG simulation produced spectral curves with errors of 16% and 11% respectively. Sand contaminated with distilled water varied from the calcium chloride target by 13% at nadir viewing and 6% when viewed at a zenith angle of 40°. Modeling wet contaminated particles as a combination of wet and dry facets proved to be an inadequate geometric representation of liquid contamination. It was found that the spectrum of wet sand in the visible and short wave infrared closely resembles that of sand that has been contaminated with calcium chloride when volume moisture content is the same in both samples.

Both dry soil and soil contaminated with calcium chloride exhibit a decrease in emissivity at increasing view zenith angles. Figures (5.32-33) show that the emissivity of both samples decreases at approximately the same rate indicating a strong correlation between directional emissivity and particle size.



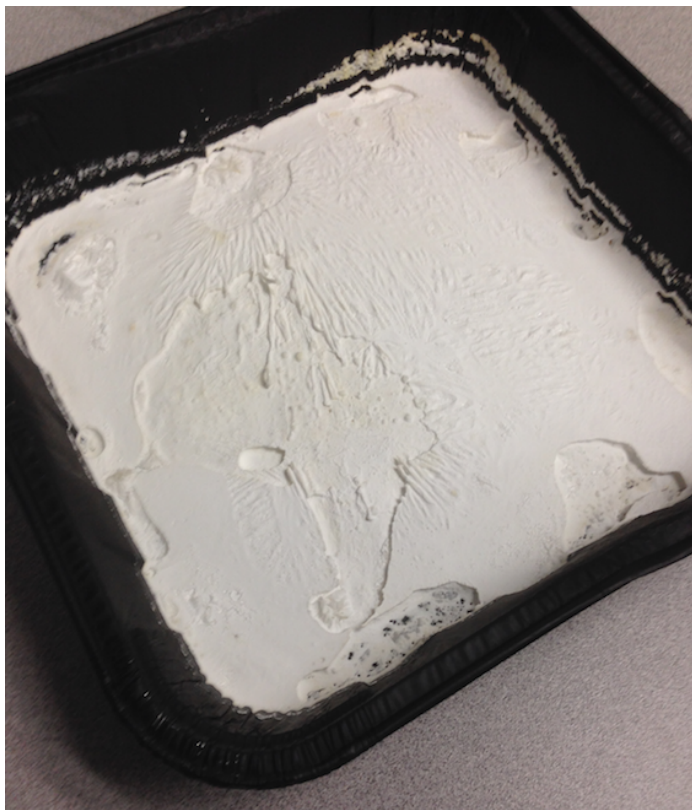


FIGURE 5.34: Calcium chloride solution after 24 hours of oven baking.

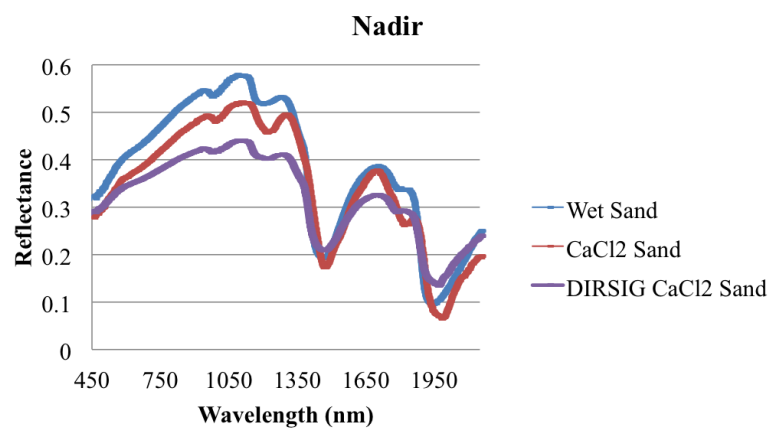


FIGURE 5.35: A DIRSIG simulation of sand contaminated with calcium chloride is plotted with LWIR measurements of wet sand and sand contaminated with calcium chloride. At nadir viewing, the DIRSIG simulation varies by 13% from the FTIR measured signature of sand with calcium chloride contamination.

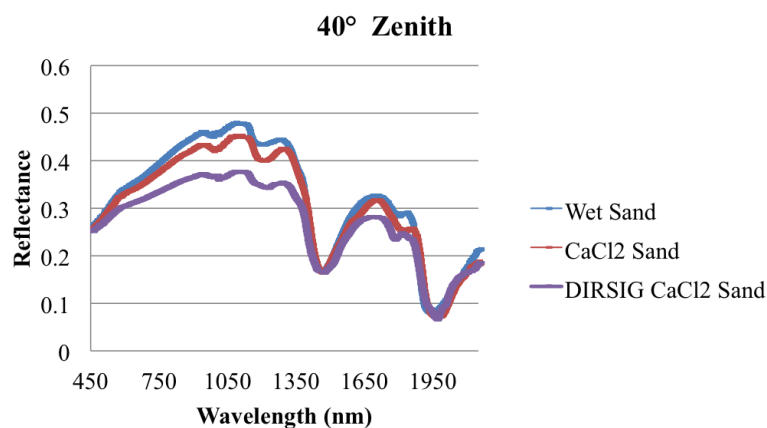
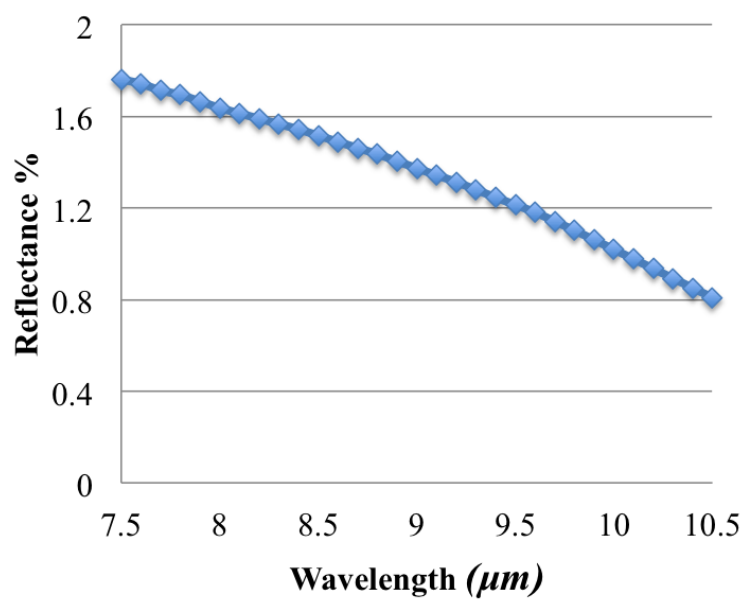


FIGURE 5.36: A DIRSIG simulation of sand contaminated with calcium chloride is plotted with LWIR measurements of wet sand and sand contaminated with calcium chloride. At a view angle of 40° zenith, the DIRSIG simulation varies by 16% from the FTIR measured signature of sand with calcium chloride contamination.

The presence of calcium chloride causes an increase in emissivity within the reststrahlen bands of approximately 0.1. It also appears to have impacted the relative emissivity magnitude between the two individual bands. Measurements of bare soil (Figure (5.32)) indicate that at each view angle between 0 and 60° zenith, the emissivity magnitude within the 7.75-8.75 $\mu\text{m}$  band is 0.02-0.03 greater than that of the reststrahlen band that falls between 8.75 and 9.5 $\mu\text{m}$ . This change in magnitude is reduced by 0.01 after the application of the calcium chloride solution (Figure (5.33)). These trends can be partially explained through analysis of the reflectance spectrum of water between 7.5 and 10.5 $\mu\text{m}$ . Figure (5.37) shows that water reflectance is very low in this portion of the LWIR. Kirchoff's law indicates that this corresponds to very high emissivity across the broad band between 7.5 and 10.5 $\mu\text{m}$ . The 0.1 increase in emissivity across this LWIR band is likely due in large part to the presence of absorbed water. Additionally, the change in relative emissivity magnitude between the two reststrahlen bands is justified by the 1-2% decrease in reflectance percentage observed between 7.5 and 10.5 $\mu\text{m}$ .

Multiple unsuccessful attempts were made to simulate the decrease in soil emissivity that arises at increasing view zenith angles. It was established that this phenomenology should be described using the Fresnel equations for absorptive media. Figure (5.38) displays simulation results obtained using theory developed by Chang et al. (2005). This plot was created using microDIRSIG at RIT. Quartz particles of 500 micron were used in the DIRSIG scene. At a view angle of 60°, an emissivity drop of approximately 0.1 is simulated. This is a very good approximation to the physical measurements displayed



---

FIGURE 5.37: LWIR reflectance spectrum of water

in Figure (5.32).

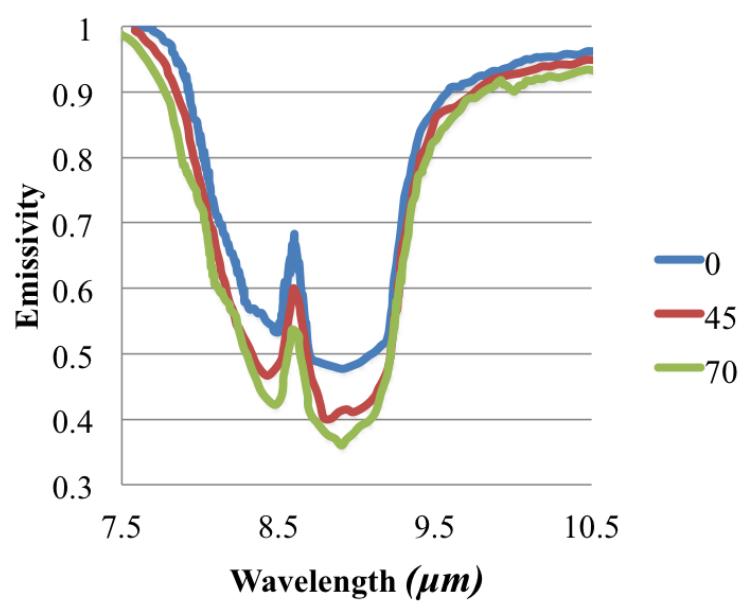


FIGURE 5.38: MicroDIRSIG simulation results for quartz emissivity at different view angles. Particles possessing a diameter of  $500 \mu m$  were used in this simulation. Emissivity fall off was observed as the view zenith angle was increased. This coincides with sand measurements made using the LWIR FTIR.

## Chapter 6

# Summary and Conclusions

Determining the spectral signatures of mixed granular solids is important for many applications that include sensor calibration, land mine detection, and the identification of radioactive materials. Field and laboratory data indicate that specific signature trends are correlated with aspects of the imaging chain such as particle size, shape, orientation, material reflectance and absorption properties, illumination, and sensor location. Metrics of bidirectional reflectance distribution function (BRDF) and directional emissivity are used to analyze and display the variance in target appearance. The objective of this research was to simulate the BRDF and directional emissivity of soil based targets by integrating realistic three dimensional computer graphic renderings with the DIRSIG radiometry model.

The derivation of signature metrics requires consideration of many geometric, radiometric, and chemical subprocesses. It is a complex problem that includes many different parameter dependencies. A work breakdown structure for signature modeling is displayed in Figure (6.1). This work gave specific attention to producing accurate target geometries. Physics engines within the Blender 3-D modeling environment were critical in the scene creation process. Grains were modeled as rigid bodies and could be posed in physical fashion. Realistic computer graphic scenes were crucial to the imaging chain modeling approach used in this research. Simulations were initialized with the emission of optical or thermal photons. These rays were propagated through a radiometric environment which included the computer generated soil geometry attributed with measured spectral emissivities of pure materials. Finally, radiation was collected and detected by a sensor whose output was a radiance image.

Initial studies were performed to test the validity of a DIRSIG based goniometer sensor

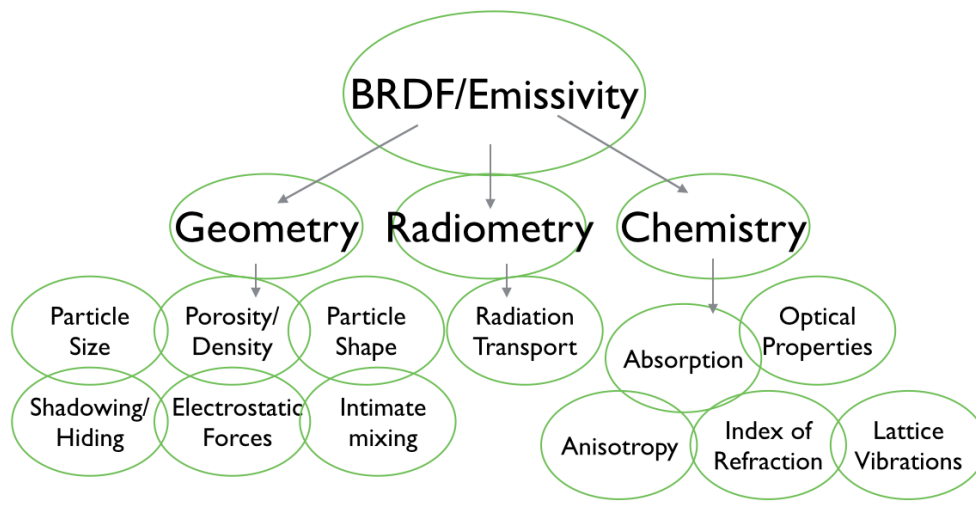


FIGURE 6.1: Simulation subprocesses

configuration. A comparative experiment in the visible regime showed that this modeling technique accurately predicts spectral features of magnitude and contrast that are observed in laboratory measurements. Simulated soil BRDF percentage was shown to vary from spectra recorded in the lab by 4%-8% across red, green and blue wavelength bands. The virtual goniometer framework was also used to predict scattering for dry soil contamination by including material properties from the NEFDS database. Additionally, the tool was used to model BRDF with changing surface contamination coverage. Linear and nonlinear trends were observed for different scenarios. Specific contamination and illumination conditions were linked to these trends.

With a virtual goniometer in hand, the relationships between phase angle and geometric subprocesses were explored in depth. It was shown that BRDF signatures will vary with particle size and grain distribution. And, the density of a soil has a notable impact on the BRDF of targets containing mixed materials. In a bimodal grain distribution model, the presence of small magnetite grains lead to a notable decrease in BRDF of high-density samples.

The simulation of thermal signatures was also performed using a similar methodology. The magnitude and spectral contrast signatures of quartz soil emissivity can be accurately realized only if the relationship between scene geometry and chemistry is modeled appropriately. Distinct absorption and transmission features in the  $7.5\mu\text{m}$  -  $10.5\mu\text{m}$  region of the thermal infrared depend upon particle size and orientation. This work established that using known software tools, including Blender 3-D and DIRSIG, one can successfully model the complex mixture of disturbed soil in this wavelength

region. Spectral behavior at the Christensen frequency and the primary, and secondary reststrahlen bands was correctly modeled with respect to particle size distribution.

It is the ability to focus on geometric modeling that separates this research from other models. Because DIRSIG provides complete user control of sample geometry and the assignment of spectral properties, it serves as a convenient test-bed for target construction, and target signature sensing. This technique can be easily modified for implementation with other material mixtures provided that pure spectral reflectance or emissivity data is available. Ultimately, this study demonstrated that by combining realistic target geometry and spectral measurements, BRDF and emissivity of complex soil mixtures could be modeled without functional data fitting or rigorous analysis of material dynamics.

It has been shown through these investigations and considerations that the remote sensing of complex mixtures can be achieved virtually. Signatures sensed in this virtual environment mimic those obtained *in situ* and in the laboratory.

## 6.1 Recommendations

### 6.1.1 Emissivity file format

Discussion in Section (5.4) of this document described the modeling of disturbed soil signatures in the LWIR. By using realistic 3-D geometries, and the spectral emissivity curves of pure quartz, distinct signature features corresponding to different particle size distributions were modeled with accuracy. This method correctly depicted transmission at the Christensen frequency, as well as the changes in emissivity magnitude occurring in the reststrahlen bands. These spectral features have not been truly portrayed using variants of the Hapke model (Moersch and Christensen, 1995), or by employing the ray tracing techniques based on Fresnel reflections that have been implemented in *microDIRSIG* (Gartley et al., 2008b, Chang et al., 2005).

In addition to particle size effects, another simultaneous phenomenology occurs in the reststrahlen band region of the LWIR. In Section (5.5), it was shown that the magnitude of emissivity decreases between 8 and  $9.5\mu\text{m}$  when a quartz based soil target is viewed at large zenith angles. This trend could be confused with similar effects caused by particle size distribution. To ensure accuracy, both processes should be modeled.

The methods used in this work rely on physical measurements. In order to reproduce the emissivity change due to view angle, this model would require full hemispherical BRDF measurements of each pure substance used in simulation. This does not seem

practical. However, the *microDIRSIG* model does accurately predict the changes in spectral features that are linked to view position. This ability is displayed in Figure (5.38).

If all important processes are to be considered, it makes sense to create a hybrid DIRSIG model. This new model should be implemented via the DIRSIG .ems (emissivity) file. For a given material, the current format of the .ems file contains spectral emissivity curves, and a list of weighting factors that are applied to the spectral emissivity values when the sensor position is modified in a DIRSIG simulation. This research has shown that the application of a single weighting factor across large LWIR bandwidths will result in inaccurate simulation results. This is because certain spectral features will not vary with view position while others change significantly. For quartz, there is nearly complete transmission at  $7.4\mu\text{m}$  for all view positions. The index of refraction approaches 1 at this wavelength (Figure (6.2)). Since air also has an index of refraction near one, there is essentially an absence of grain boundaries. Applying a scaling factor at this wavelength is unphysical. What is needed is a tool to produce wavelength dependent scaling factors that are calculated for different sensor view positions. Although the methods used in this work will not aptly compute wavelength dependent weighting factors, *microDIRSIG* can complete this task.

In theory, *microDIRSIG* could be used to determine the change in signature that is observed at different view positions. This would be done by direct comparison between BRDF/emissivity calculated at the nadir view position and BRDF/emissivity from other viewing angles. This could be completed in as few as two *microDIRSIG* runs. This is possible because the tool treats each detector element as a virtual source that emits rays which travel through a scene until they are traced into the hemisphere above the target where they are collected and binned into virtual detectors that are distributed in zenith and azimuth. The change in wavelength dependent BRDF/emissivity between the nadir collection and the off-nadir collection could then be inserted into a DIRSIG .ems file using an XML file editor. Then, wavelength dependent scaling factors could be used in the traditional operation of DIRSIG.

By modifying the DIRSIG .ems file, the simultaneous emission processes determined by particle size distribution and sensor view position can be simulated. Effects due to view position would be handled with *microDIRSIG*. Signature simulation at nadir viewing would be performed using the methods used in this research.



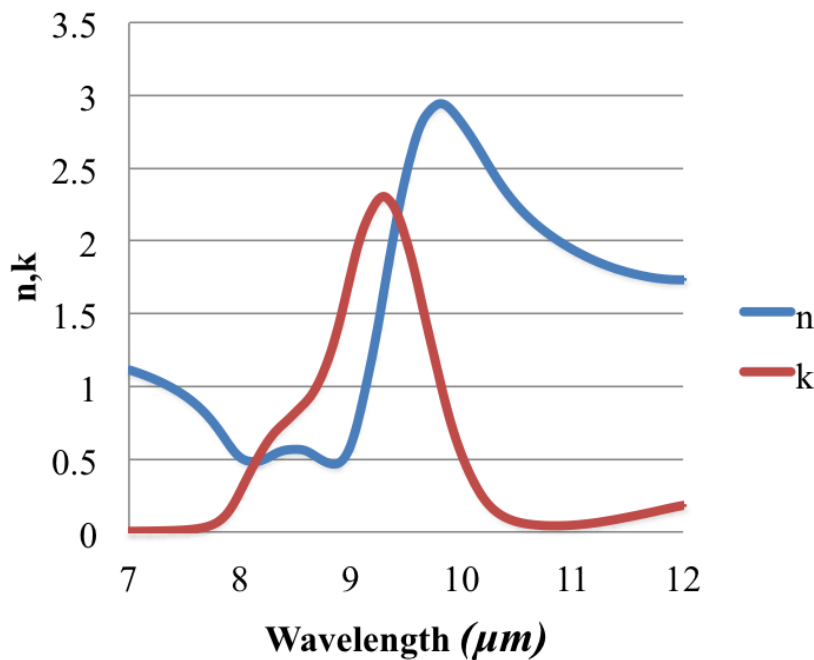


FIGURE 6.2: Real and imaginary components of the complex index of refraction for quartz

### 6.1.2 Fluid Simulation

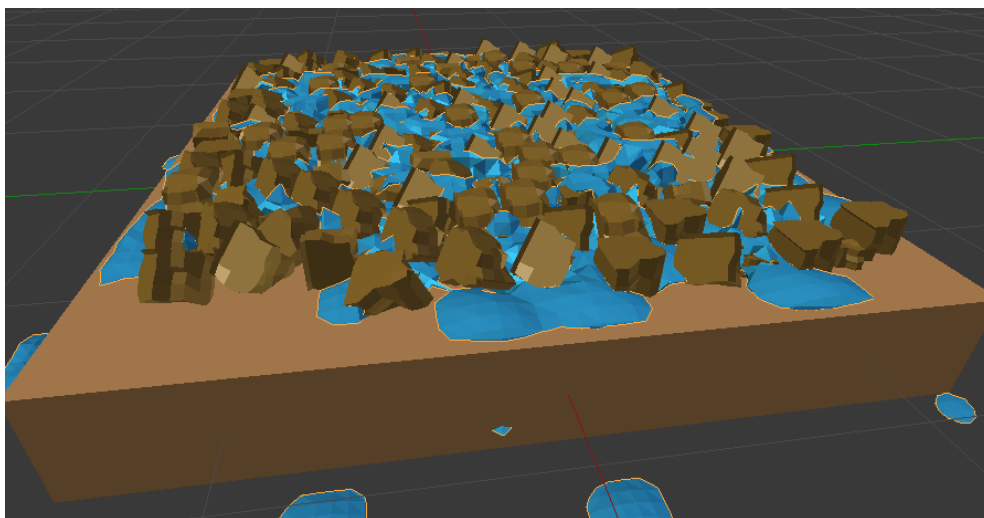
This work included a modeling effort that considered liquid contaminants. One difficulty encountered while modeling liquids was the inability to accurately create the geometry of the contaminant. The facets of contaminated particles were separated into two classes. Some facets were attributed with the material description of wet soil. All other facets were assigned the properties of baked calcium chloride. A single particle would contain some "wet" facets and some facets that were assigned the properties of a dry chemical. The material assignments were made arbitrarily. This strategy produced signatures that varied from physical measurements by 13-16%.

To simulate signatures that are more accurate, the method by which liquid contamination scenes are built needs to be improved. A physics engine for fluid simulation exists within the Blender 3-D graphic design software. This feature can be used to produce scenes with more realism.

The volume of liquid contaminant used in a scene can be controlled by using a bounding shape. Once volume is determined, gravity is applied to the fluid. As is true with Blender 3-D rigid body simulations, the dynamics of flow are depicted as a motion

picture. Calculations to determine shape and position of the fluid are made frame by frame. Within a scene, particles can be defined as obstacles, and liquid will flow on and around grains in physical fashion. The fluid is treated as a single object within Blender 3-D. Like any other object, it can be assigned the properties of any unique material.

Using the Blender 3-D physics engine, liquids can be incorporated into DIRSIG models. By modeling the geometry of contaminants more truly, simulation results should be closer to those observed in nature and in the laboratory. A fluid scene generated in Blender 3-D is displayed in Figure (6.3).




---

FIGURE 6.3: Blender 3-D contains a physics engine that could be used to simulate geometries of fluid contamination. Fluids are faceted and can be assigned distinct material properties.

### 6.1.3 Advanced Ray Tracing for Sensitive Absorption Features

This work has discussed the difficulty surrounding the simulation of detectable absorption features in the LWIR. In section (5.4), a method was presented to create such simulations using the emissivity signatures of pure materials. It was also noted that approaches relying on pure optical constants, such as the Hapke model and *microDIRSIG*, do not simulate LWIR absorption features with great accuracy.

This problem is hard because dramatic changes in the complex index of refraction coincide with absorption. Light propagation is stunted in a lossy medium, and the mean optical path length (MOPL) of radiation is very short at certain wavelengths. For such materials, geometry becomes important. In many cases, the size and shape of a specimen will determine the mode of radiation scatter.

Quartz has been referenced throughout this thesis, and it is a great illustration of the delicate relationship between absorption and particle size. Figure (6.4) shows the reflectance spectrum of powdered quartz (100-200 $\mu m$  diameters). The reflectance peaks between 8 and 10 $\mu m$  are a result of the distinct change in the complex index of refraction (Figure (6.2)) at those wavelengths. Specifically, the absorption coefficient of quartz reaches very high values due to the stretching and bending of ionic bonds within SiO<sub>2</sub> atoms. This leads to signatures that are dominated by surface scattering. In the case of particulate quartz, radiation due to self emission is largely reabsorbed within grain boundaries and can not be sensed.

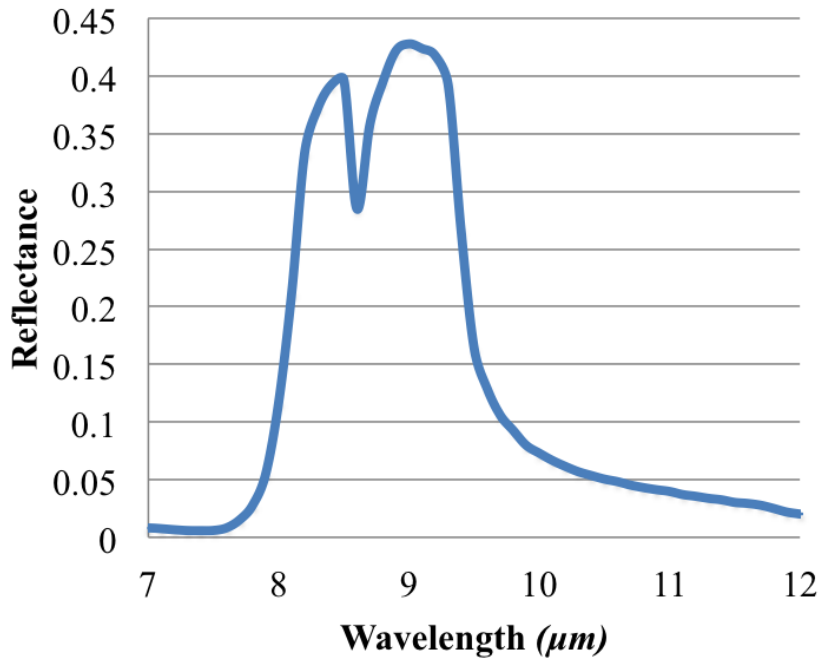


FIGURE 6.4: Reflectance spectrum of granular quartz (100-200 $\mu m$ )

Like quartz, many materials are lossy. Radiation that propagates in a lossy medium is inhomogeneous. This means that the normal vectors of the planes of constant amplitude and constant phase do not coincide. Fresnel formulae that account for the inhomogeneity have been used for the purpose of ray tracing by Chang et al. (2005), and are incorporated into *microDIRSIG*. Radiation propagating in a lossy medium loses magnitude over a path length. The scaling factor for attenuation is expressed in Equation (6.1)

$$F(\lambda, n, k, \alpha) = e^{-2\pi K l \cos(\alpha)/\lambda} e^{2\pi i N l/\lambda}. \quad (6.1)$$

Where  $N$  is the *apparent* real part of the complex index of refraction that is perpendicular to the surfaces of constant phase

$$N(n, k, \alpha) = \sqrt{\frac{1}{2} \left[ n^2 - k^2 + \sqrt{(n^2 - k^2)^2 + 4(nk/\cos(\alpha))^2} \right]}. \quad (6.2)$$

The *apparent* imaginary part of the complex index of refraction is denoted as  $K$

$$K(n, k, \alpha) = \frac{nk}{\cos(\alpha)N}. \quad (6.3)$$

The inhomogeneity angle is represented as  $\alpha$ . This is the angle separating the normal vector of the planes of constant phase and the the normal vector of the planes of constant amplitude.

Through the analysis of path loss, the relationship between particle size and absorption band signatures can be understood more thoroughly. Figure (6.5) is another reflectance signature of quartz powder. This curve corresponds to grains smaller than  $75\mu m$  in diameter. Because grains are smaller than those represented by Figure (6.4), there is more opportunity for radiation to reach the grain boundaries before it is attenuated and reabsorbed. This leads to suppression of the reflectance peaks between  $8\mu m$  -  $10\mu m$ .

To illustrate the relationship between path loss and particle size, the scaling factor for attenuation,  $F(\lambda, n, k, \alpha)$ , has been plotted for optical path lengths ranging from  $2.5\mu m$  -  $100\mu m$ . Figure (6.6) displays the relationship for a inhomogeneity angle of  $0^\circ$ . Figure (6.7) displays the relationship using a inhomogeneity angle of  $60^\circ$ . Between  $8\mu m$  -  $10\mu m$ , both plots depict very small scaling factors at even the shortest optical path lengths. This gives insight into why *microDIRSIG* has difficulty recreating particle size dependent features in the reststrahlen bands. The plots of the attenuation factor show that for particles as small as  $2.5\mu m$ , radiation entering a grain from the outside has no chance of reemerging by volume scattering before it is completely attenuated. If all rays in a DIRSIG simulation impinge upon quartz grains from the hemisphere above, the simulation will predict the same signature for targets of large and small grains. This highlights the need for a more thorough representation of self emission within DIRSIG. If the aspect of particle size is to be better represented, rays should be cast from the inside of grains as well as from an outside source. This way, modalities of surface scattering, multiple scattering, and volume scattering will be captured. For it is volume scatter that contributes greatest to the spectral emissivity of quartz in the reststrahlen bands.

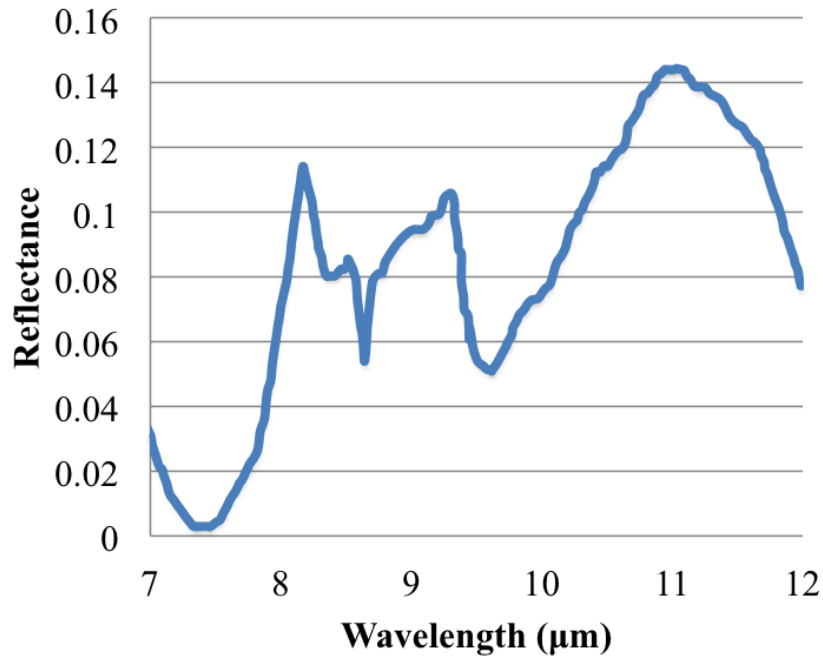


FIGURE 6.5: Reflectance spectrum of granular quartz ( $<75\mu\text{m}$ )

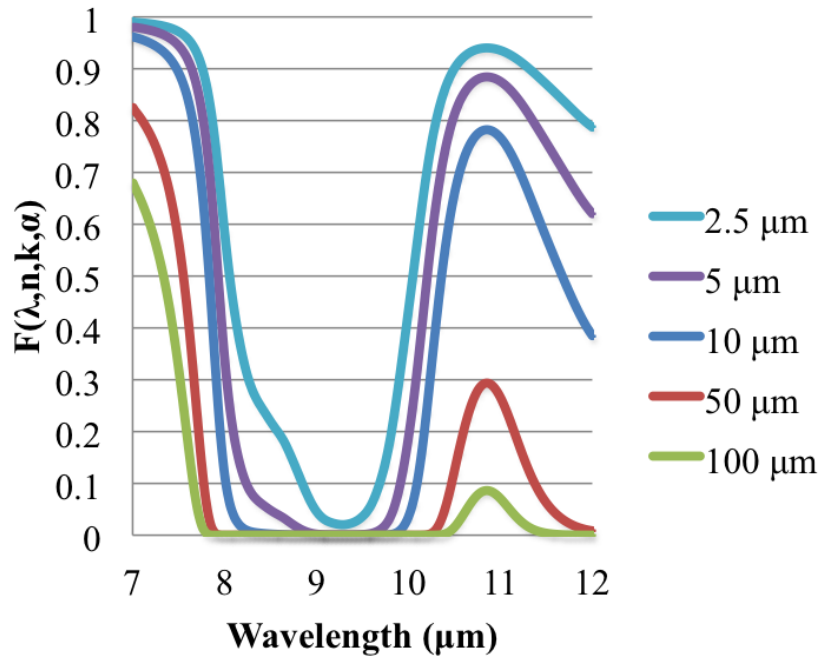


FIGURE 6.6: Scaling factor of attenuation in quartz for an inhomogeneity angle of  $0^\circ$ . Path lengths of  $2.5\mu\text{m}$ ,  $5\mu\text{m}$ ,  $10\mu\text{m}$ ,  $50\mu\text{m}$ , and  $100\mu\text{m}$  are plotted together.

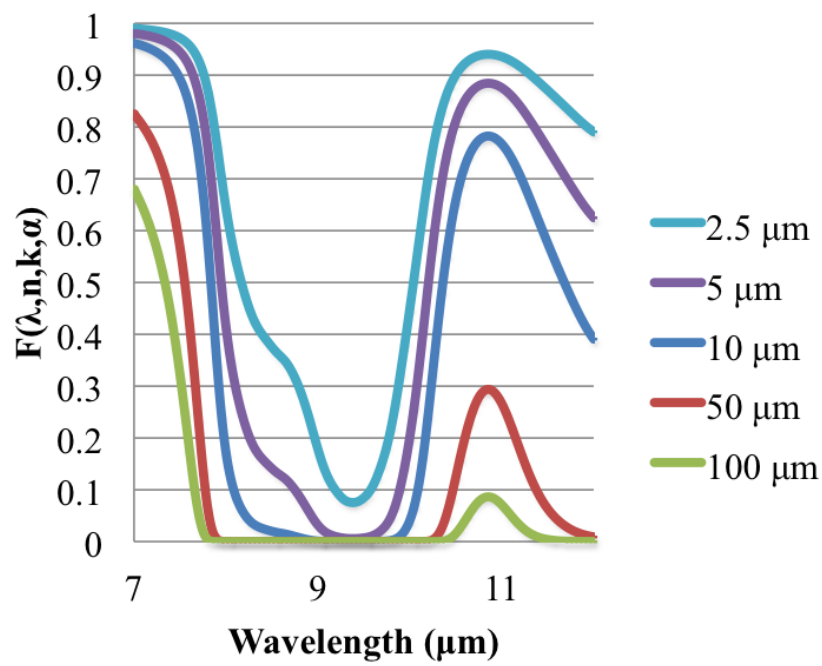


FIGURE 6.7: Scaling factor of attenuation in quartz for an inhomogeneity angle of  $60^\circ$ . Path lengths of  $2.5\mu m$ ,  $5\mu m$ ,  $10\mu m$ ,  $50\mu m$ , and  $100\mu m$  are plotted together.

# Bibliography

- Z. Wang, C.A. Coburnb, X. Rena, D. Mazumdarb, S. Myshakb, A. Mullinb, and P.M. Teillet. Assessment of soil surface BRDF using an imaging spectrometer. In *Proceedings of SPIE 7830: Image and Signal Processing for Remote Sensing*, volume 7830(10), 2010, 2010.
- Jeffrey R. Johnson, Paul G. Lucey, Keith A. Horton, and Edwin M. Winter. Infrared Measurements of Pristine and Disturbed Soils. *Remote Sensing Environment*, 64: 34–36, 1998, 1998a.
- Brent Burley. Physically-Based Shading at Disney. Technical report, Walt Disney Animation Studios, 2012.
- Christophe Hery and Ryusuke Villemin. Physically Based Lighting at Pixar. Technical report, Pixar Animation Studios, 2013.
- Stephen H. Westin, James R. Arvo, and Kenneth E. Torrance. Predicting Reflectance Functions from Complex Surfaces. In *Proceedings of the 19th annual conference on Computer Graphics and Interactive Techniques*, volume 26, pages 255–264, 1992, 1992.
- Stephen H. Westin, Hongsong Li, and Kenneth E. Torrance. A Comparison of Four BRDF Models. In *Eurographics Symposium on Rendering*, pages 1–10, 2004, 2004.
- Huiying Xu, Yi Ru, and Yinlong Sun. From Physics to Illumination Models of Subsurface Scattering, Computer Science Technical Reports, Purdue University, No. 06-002, 2006.
- B.A. Darling and J. A. Ferwerda. The tangiBook: A Tangible Display System for Direct Interaction with Virtual Surfaces. In *IS&T 17th Color Imaging Conference*, pages 206–266, 2009, 2009.
- K. Torrance and E. Sparrow. Theory for Off-Specular Reflection from Roughened Surfaces. *Optical Society of America*, Vol. 57:pp. 1105–1114, 1976.

- Xiao D. He, Kenneth E. Torrance, Francois X. Sillion, and Donald P. Greenberg. A Comprehensive Physical Model for Light Reflection. In *Computer Graphics (ACM SIGGRAPH '91 Proceedings)*, volume Vol. 25, pages pp. 175–186, July 1991.
- Addy Ngan, Frédo Durand, and Wojciech Matusik. Experimental Analysis of BRDF Models. In *Eurographics Symposium on Rendering*, pages pp. 117–126, Konstanz, Germany, 2005. Eurographics Association.
- S.K. Nayar and M. Oren. Generalization of the lambertian model and implications for machine vision. *International Journal on Computer Vision*, Vol. 14(No. 3):pp. 227–251, Apr 1995.
- Pat Hanrahan and Wolfgang Krueger. Reflection from Layered Surfaces due to Sub-surface Scattering. In editor, editor, *Proceedings of the 20th annual conference on Computer Graphics and Interactive Techniques*, pages pp. 165–174, 1993.
- P. Beckmann and A. Spizzichino. *The Scattering of Electromagnetic Waves From Rough Surfaces*. MacMillan. 1963, 1963.
- Michael Ashikmin and Peter Shirley. An Anisotropic Phong BRDF Model. *Journal of Graphics Tools*, Vol. 5(2):pp. 25–32, 2000, 2000.
- E. Ientilluci and M. Gartley. Impact of BRDF on Physics Based Modeling as Applied to Target Detection in Hyperspectral Imagery. In *Proceedings of SPIE 7334: Algorithms and technologies for multispectral, hyperspectral, and ultraspectral imagery*, volume 7334(29), 2009 2009.
- James T. Kajiya. The Rendering Equation. *Computer Graphics*, Vol. 20(No. 4), August, 1986 1986.
- Mark Colbert, Sumanta Pattanaik, and Jaroslav Krivánek. BRDF Shop. *IEEE Computer Graphics and Applications*, pages pp. 30–36, January/February, 2006, 2006.
- F.E. Nicodemus, J.C. Richmond, and J.J. Hsia. *Geometrical Considerations and Nomenclature for Reflectance*, U.S. Department of Commerce, National Bureau of Standards, October, 1977 1977.
- Jay S. Gondek, Gary W. Meyer, and Jonathan G. Newman. Wavelength Dependent Refelctance Functions. In *Proceedings of the 21st annual conference on Computer Graphics and Interactive Techniques*, pages 213–220, 1994, 1994.
- Gregory J. Ward. Measuring and modeling anisotropic reflection. In *Proceedings of SIGGRAPH*, pages pp. 265–272, 1992.



- Arne Dür. An Improved Normalization for the Ward Reflectance Model. *Journal of Graphics, GPU, and Game Tools*, Vol. 11(1):pp. 51–59, 2006.
- David Geisler-Moroder and Arne Dür. A New Ward BRDF Model with Bounded Albedo. *Computer Graphics Forum*, Vol. 29(4):pp. 1391–1398, 2010, 2010.
- John.P. Kerekes, Kristin-Elke Strackerjan, and Carl Salvaggio. Spectral reflectance and emissivity of man-made surfaces contaminated with environmental effects. *Optical Engineering*, 47(10), October, 2008 2008.
- Yue Dong, Jiaping Wang, Fabio Pellacini, Xin Tong, and Baining Guo. Fabricating Spatially-Varying Subsurface Scattering. *ACM Transactions on Graphics (TOG)*, Vol. 29(Article 62), July, 2010 2010.
- Dominik Bänninger and Hannes Flühler. Modeling Light Scattering at Soil Surfaces. In *IEEE Transactions on Geoscience and Remote Sensing*, volume 42(No. 7), pages 1462–1471, July, 2004 2004.
- Zhi-Jian Li, Adrian K. Fung, Saibun Tjuatja, Daniel P. Gibbs, Christopher L. Betty, and James R. Irons. A Modeling Study of Backscattering from Soil Surfaces. In *IEEE Transactions on Geoscience and Remote Sensing*, volume 34(No. 1), pages 264–271, January, 1996 1996.
- Shunlin Liang and John R. G. Townshend. A Modified Hapke Model for Soil Bidirectional Reflectance. *Remote Sensing Environment*, Vol. 55:1–10, 1996, 1996.
- B.W. Hapke. *Theory of Reflectance and Emittance Spectroscopy*. Cambridge University Press, New York. 1993, 1993.
- Bruce Hapke. Bidirectional reflectance spectroscopy 7: The single particle phase function hockey stick relation. *Icarus*, 221(2):1079–1083, 2012a.
- M. G. Gartley, S. D. Brown, and J. R. Schott. Micro-Scale Surface and Contaminate Modeling for Polarimetric Signature Prediction. In *SPIE 6972: Polarization: Measurement, Analysis, and Remote Sensing*, volume 6972, March, 2008, 2008a.
- M. G. Gartley, J. R. Schott, and S. D. Brown. Micro-Scale Modeling of Contaminant Effects on Surface Optical Properties. In *SPIE 7086: Imaging Spectrometry*, volume 7086, August, 2008, 2008b.
- John R Schott. *Remote sensing*. Oxford University Press, 2007.
- Michael Theodore Eismann. Hyperspectral remote sensing. SPIE, 2012.

- E Ben-Dor, JR Irons, and GF Epema. Soil reflectance. *Man. Remote Sens. Remote Sens. Earth Sci.*, 3:111, 1999.
- Angela Kociolek. Unpaved Road Chemical Treatments. Technical report, U.S. Department of Transportation Federal Highway Administration, 2013.
- John Kerekes, Michael Gartley, Christopher De Angelis, Carl Salvaggio, Chris Gittins, Michael Costolo, and Bogdan Cosofret. Measurements and modeling of lwir spectral emissivity of contaminated quartz sand. In *Hyperspectral Image and Signal Processing: Evolution in Remote Sensing*, 2013.
- R.J.P. Lyon. Evaluation of Infrared Spectrophotometry for Compositional Analysis of Lunar and Planetary Soils . Part II: Rough and Powdered Surfaces. NASA-CR-100. Technical report, NASA, 1964.
- John W. Salisbury and Andrew Wald. The Role of Volume Scattering in Reducing Spectral Contrast of Reststrahlen Bands in Spectra of Powdered Minerals. *ICARUS*, 96:121–128, 1992.
- Jeffrey R. Johnson, Paul G. Lucey, Keith A. Horton, and Edwin M. Winter. Infrared Measurements of Pristine and Disturbed Soils 1. Spectral Contrast Differences between Field and Laboratory Data. *Remote Sens. Environ.*, 64:34–46, 1998b.
- Christopher J Deloye, Michael S West, and John M Grossmann. Changes in apparent emissivity as a function of viewing geometry. In *SPIE Defense, Security, and Sensing*, pages 80400J–80400J. International Society for Optics and Photonics, 2011.
- R.K. Vincent and G.R. Hunt. Infrared reflectance from material surfaces. *Appl. Opt.*, 74:53–59, 1968.
- JE Moersch and Philip R Christensen. Thermal emission from particulate surfaces: A comparison of scattering models with measured spectra. *Journal of Geophysical Research: Planets (1991–2012)*, 100(E4):7465–7477, 1995.
- JR Maxwell, J Beard, S Weiner, Da Ladd, and S Ladd. Bidirectional reflectance model validation and utilization. Technical report, DTIC Document, 1973.
- Michael I Mishchenko, Larry D Travis, and Andrew A Lacis. *Multiple scattering of light by particles: radiative transfer and coherent backscattering*. Cambridge University Press, 2006.
- Michael I Mishchenko, Janna M Dlugach, Edgard G Yanovitsku, and Nadia T Zakharova. Bidirectional reflectance of flat, optically thick particulate layers: an efficient radiative transfer solution and applications to snow and soil surfaces. 1999.

- Janna M Dlugach, Michael I Mishchenko, Li Liu, and Daniel W Mackowski. Numerically exact computer simulations of light scattering by densely packed, random particulate media. *Journal of Quantitative Spectroscopy and Radiative Transfer*, 112(13):2068–2078, 2011.
- Victor P Tishkovets, Elena V Petrova, and Michael I Mishchenko. Scattering of electromagnetic waves by ensembles of particles and discrete random media. *Journal of Quantitative Spectroscopy and Radiative Transfer*, 112(13):2095–2127, 2011.
- Bruce Hapke. *Theory of reflectance and emittance spectroscopy*. Cambridge University Press, 2012b.
- Janet E. Simms, Ernest S. Berney IV, Danny W. Harrelson, Maureen K. Corcoran, and Ray M. Castellane. Analysis of Long Wave Infrared Soil Data to Predict Reflectance Response. Technical report, US Army Corps of Engineers, 2009.
- Charles M. Bachmann, Robert A. Fusina, Marcos J. Montes, Rong-Rong Li, Daniel Korwan, Ellen Bennert, W.D. Miller, David Gillis, C.R. Nichols, and John C. Fry. Virginia Coast Reserve 2007 Remote Sensing Experiment. Technical report, Naval Research Lab Remote Sensing Division, 2007.
- Charles M. Bachmann, Robert A. Fusina, Marcos J. Montes, Rong-Rong Li, Carl Gross, C.R. Nichols, John C. Fry, Chris Parrish, Jon Sellars, and Stephen White. Talisman-Saber 2009 Remote Sensing Experiment. Technical report, Naval Research Lab Remote Sensing Division, 2009.
- Charles M. Bachmann, Robert A. Fusina, Marcos J. Montes, Rong-Rong Li, Deric Gray, Daniel Korwan, Carl Gross, Christopher Jones, Krista Lee, and Jon Wende. Mariana Islands-Hyperspectral Airborne Remote Environmental Sensing Experiment 2010. Technical report, Naval Research Lab Remote Sensing Division, 2010.
- Charles M Bachmann, William Philpot, Andrei Abelev, and Dan Korwan. Phase angle dependence of sand density observable in hyperspectral reflectance. *Remote Sensing of Environment*, 150:53–65, 2014.
- Douglas S Peck, Malachi Schultz, Charles M Bachmann, Brittany Ambeau, and Justin Harms. Influence of density on hyperspectral brdf signatures of granular materials. In *SPIE Defense+ Security*, pages 94720F–94720F. International Society for Optics and Photonics, 2015.
- F Capaccioni, P Cerroni, MA Barucci, and M Fulchignoni. Phase curves of meteorites and terrestrial rocks: Laboratory measurements and applications to asteroids. *Icarus*, 83(2):325–348, 1990.

- Georgi T Georgiev, Charles K Gatebe, James J Butler, and Michael D King. Brdf analysis of savanna vegetation and salt-pan samples. *Geoscience and Remote Sensing, IEEE Transactions on*, 47(8):2546–2556, 2009.
- S Kaasalainen. Laboratory photometry of planetary regolith analogs-i. effects of grain and packing properties on opposition effect. *Astronomy & Astrophysics*, 409(2):765–769, 2003.
- JAM Dematte, MR Nanni, AP da Silva, JF de Melo Filho, WC Dos Santos, and RC Campos. Soil density evaluated by spectral reflectance as an evidence of compaction effects. *International Journal of Remote Sensing*, 31(2):403–422, 2010.
- Michael K Shepard and Paul Helfenstein. A laboratory study of the bidirectional reflectance from particulate samples. *Icarus*, 215(2):526–533, 2011.
- Peter CY Chang, JG Walker, and KI Hopcraft. Ray tracing in absorbing media. *Journal of Quantitative Spectroscopy and Radiative Transfer*, 96(3):327–341, 2005.